

ABSTRACT

CHENG, HUI. Nanofiber-reinforced Quasi-solid-state Polymer Electrolyte Design for Room-temperature, High-performance Li Metal Batteries (Under the direction of Dr. Xiangwu Zhang).

Compared with today's Li-ion batteries, Li-metal batteries can potentially provide higher capacity and larger operating voltage, thus delivering higher energy density while remaining lightweight, which are extremely promising to satisfy the ever-growing demands for portable electronic devices, electric vehicles and grid-energy storage systems. The development of polymer electrolytes is off great important in replacing the liquid electrolyte for advanced Li-metal battery due to their high mechanical strength and flexibility, good interfacial contact with the electrodes and non-flammability, which can help to overcome the dramatic volume variation and suppress the lithium dendrite formation during cycling. However, the ionic conductivities of polymer electrolytes are usually low ($\sim 10^{-6}$ S cm^{-1}) at room temperature, which hinders their application in practical Li-metal batteries. Thus, in order to improve the Li ion conductance, organic plasticizers or inorganic fillers are introduced to the polymer system to increase the amorphous region or promote extra Li ion conductive pathway for faster and more effective ion transportation. In this dissertation, the historical developments and recent improvements of polymer electrolytes with additives are summarized. The contributions and possible mechanisms of organic plasticizer and inorganic active fillers to the ionic conductivity, mechanical properties, and electrochemical stability of the polymer electrolytes are profoundly explored. Polymer electrolytes with different designs and fabrication exhibit superior electrochemical properties for various Li battery systems including Li-metal and Li-sulfur batteries.

To obtain the improved the ionic conductivity and sufficient mechanical strength for effective Li ion conductance and suppressed Li dendrite formation within Li batteries, modified polymer electrolytes are designed and manufactured. Initially, research is mainly concentrated on polymer

matrix to reach to better Li-ion transportation. We have chemically synthesized the Li monomer to fabricate single-ion conducting polymer electrolyte, where charge delocalized anions are covalently bonded along the polymer backbone and only Li ions are allowed to migrate during charging-discharging process. The effects of introduced plasticizer and electrospun nanofibrous membrane for the resultant single-ion conducting polymer electrolyte have been investigated. Later, a novel single-ion conducting composite polymer electrolyte by embedding inorganic active fillers and reducing the amount of plasticizer was studied. By optimizing the content of inorganic Li-ion conductors with uniform distribution, the overall electrochemical stabilities of single-ion conducting polymer electrolyte are dramatically improved. After that, in order to maintain an interconnected interface between cathode-electrolyte and protect Li anode from dendrites formation, two thin composite polymer electrolyte membranes were created by directly coating on the electrodes. In short, several promising designs of polymer electrolytes are specified, excellent electrochemical and cycling performances of these novel polymer electrolytes are accomplished when applied in all-solid-state Li batteries.

In summary, a general strategy in addressing the multiple issues for all-solid-state Li-metal batteries is presented in this dissertation based on chemical and structural designs of polymer electrolytes, which are necessary for the ever-accelerating development and practical application of solid electrolytes toward all-solid-state Li batteries in the field of research and industrialization.

© Copyright 2022 by Hui Cheng

All Rights Reserved

Nanofiber-reinforced Quasi-solid-state Polymer Electrolyte Design for High-performance Li
Metal Batteries

by
Hui Cheng

A dissertation submitted to the Graduate Faculty of
North Carolina State University
in partial fulfillment of the
requirements for the degree of
Doctor of Philosophy

Fiber and Polymer Science

Raleigh, North Carolina
2022

APPROVED BY:

Dr. Xiangwu Zhang
Committee Chair

Dr. Wei Gao

Dr. Philip Bradford

Dr. Hsiao-Ying Shadow Huang

BIOGRAPHY

Hui Cheng was born in Henan, China. She received her B.S. degree in 2016 in Chemical Engineering and Technology from the College of Chemistry, Chemical Engineering and Materials Science at Soochow University and her M.S in Polymer Science in 2017 from the University of Akron. Then she started to pursue her Ph.D. in Fiber and Polymer Science in the Department of Textile Engineering, Chemistry, and Science in the Wilson College of Textiles under the supervision of Prof. Xiangwu Zhang at North Carolina State University. Her research interests focus on nanostructured materials for energy storage, especially in organic and nanofibrous materials for solid-state electrolytes applied in Li-metal batteries.

ACKNOWLEDGMENTS

Here I would like to thank all my committee members, Dr. Xiangwu Zhang, Dr. Wei Gao, Dr. Philip Bradford, Dr. Hsiao-Ying Shadow Huang and Dr. Veronica Augustyn for all the valuable advice and time to evaluate my work. In particular, I would like to express my sincerest gratitude to my advisor, Dr. Xiangwu Zhang, for his great mentorship and thoughtful insights during my Ph.D. study. This work would not be completed without his endless encouragement and guidance.

I would also like to thank all my co-authors and great lab members in Dr. Zhang's group, for their great help and advice.

I also appreciate the help from the faculty and staff in the Analytical Instrumentation Facility and the Wilson College of Textiles at NC State University, for their help in materials and characterizations.

Moreover, I want to thank my roommate, Dr. Jiang, who I have lived with for five years, and all other friends for their encouragement during my Ph.D. study.

Most importantly, I would like to express my special gratitude to my sister and my parents for their love and constant support.

TABLE OF CONTENTS

LIST OF TABLES	viii
LIST OF FIGURES	ix
CHAPTER 1: OVERVIEW OF SOLID POLYMER ELECTROLYTES	1
1.1 Introduction of solid-state electrolyte	1
1.2 Development of organic solid polymer electrolytes	2
1.2.1 Lithium-ion transference number	4
1.2.2 Polymer matrices	5
1.3 Additives	12
1.3.1 Organic plasticizers.....	12
1.3.2 Inorganic fillers	13
1.3.3 Nanofiber-shaped additives	22
1.4 Li-ion conduction mechanisms	33
CHAPTER 2: RESEARCH OBJECTIVES.....	37
2.1 Polyacrylonitrile Nanofiber-Reinforced Flexible Single-Ion Conducting Polymer Electrolyte for High-Performance, Room-Temperature All-Solid-State Li-Metal Batteries ...	37
2.2 $\text{Li}_{6.28}\text{La}_3\text{Zr}_2\text{Al}_{0.24}\text{O}_{12}$ -reinforced Single-ion Conducting Composite Polymer Electrolyte for Room-Temperature Li-Metal Batteries	38
2.3 Garnet-type Composite Polymer Electrolyte for Room-Temperature All-Solid-State Li-S Battery.....	39

CHAPTER 3: Polyacrylonitrile Nanofiber-Reinforced Flexible Single-Ion Conducting Polymer Electrolyte for High-Performance, Room-Temperature All-Solid-State Li-Metal Batteries	41
3.1 Introduction.....	43
3.2 Experimental Section	46
3.2.1 Materials	46
3.2.2 Synthesis of monomer lithium (4-styrenesulfonyl) (trifluoromethylsulfonyl) imide ..	47
3.2.3 Preparation of single-ion conducting polymer electrolytes	50
3.2.4 Structure characterization	51
3.2.5 Electrochemical performance evaluation.....	52
3.3 Results and Discussion	54
3.3.1 Design of plasticized single-ion conducting polymer electrolytes reinforced with PAN-NFs	54
3.3.2 Electrochemical performance of plasticized single-ion conducting polymer electrolytes reinforced with PAN-NFs.....	61
3.3.3 High performance of all-solid-state Li-metal batteries	69
3.4 Conclusions.....	75
CHAPTER 4: $\text{Li}_{6.28}\text{La}_3\text{Zr}_2\text{Al}_{0.24}\text{O}_{12}$ -reinforced Single-ion Conducting Composite Polymer Electrolyte for Room-Temperature Li-Metal Batteries	77
4.1 Introduction.....	79
4.2 Experimental Section	82
4.2.1 Materials	82
4.2.2 Synthesis of monomer lithium (4-styrenesulfonyl) (trifluoromethylsulfonyl) imide ..	82

4.2.3 Fabrication of $\text{Li}_{6.28}\text{La}_3\text{Al}_{0.24}\text{Zr}_2\text{O}_{12}$ nanofibers	85
4.2.4 Fabrication of silane-modified $\text{Li}_{6.28}\text{La}_3\text{Al}_{0.24}\text{Zr}_2\text{O}_{12}$ nanofibers (s@LLAZO).....	86
4.2.5 Preparation of single-ion conducting composite polymer electrolytes.....	86
4.2.6 Structure characterization	87
4.2.7 Electrochemical performance evaluation.....	88
4.2.8 Battery Performance Evaluation	90
4.3 Results and Discussion	90
4.3.1 Design of single-ion conducting composite polymer electrolytes.....	92
4.3.2 Electrochemical performance of single-ion conducting composite polymer electrolytes	96
4.3.3 High performance of all-solid-state Li-metal batteries	101
4.4 Conclusions.....	105
CHAPTER 5: Garnet-type Composite Polymer Electrolyte for Room-Temperature All-Solid- State Li-S Battery.....	
5.1 Introduction.....	108
5.2 Experimental Section	111
5.2.3 Preparation of LLAZO incorporated composite polymer electrolytes	112
5.2.4 Structure characterization	113
5.2.5 Electrochemical performance evaluation.....	113
5.2.6 Battery Performance Evaluation	115
5.3 Results and Discussion	116
5.3.1 Design of LLAZO NFs-reinforced composite polymer electrolytes	117

5.3.2 Electrochemical performance characterization of LLAZO NFs-reinforced composite polymer electrolytes.....	121
5.3.3 Battery performance evaluation of all-solid-state Li-S batteries	127
5.4 Conclusions.....	133
CHAPTER 6: Recommended Future Work.....	134
REFERENCES	136

LIST OF TABLES

Table 3.1	Mechanical properties of PAN-NFs, SIPE-2.5 and SIPE-2.5-PAN.....	58
Table 3.2	Electrochemical properties of dry SIPE, SIPE-x and SIPE-2.5-PAN membranes....	62
Table 3.3	Mechanical properties, electrochemical and battery performances of different SIPEs.....	72
Table 4.1	Ionic conductivities and mechanical properties of SICE _x with different s@LLAZO NFs contents at room temperature.....	92
Table 4.2	Electrochemical properties of SICE ₀ , SICE ₃₀ and p-SICE ₃₀	96
Table 4.3	The data summary and calculated lithium-ion transference number of p-SICE ₃₀ at 60 °C.....	98
Table 5.1	Ionic conductivities and mechanical properties of CPEs with different LLAZO contents at room temperature.....	119
Table 5.2	Electrochemical properties of CPEs with different LLAZO contents.....	122
Table 5.3	The data summary and calculated lithium-ion transference numbers of CPEs with different filler contents at 60 °C.....	123

TABLE OF FIGURES

Figure 1.1 Chemical structures of single-ion conducting polymer electrolytes: (a) and (b) with carboxylate anions, [45] (c) and (d) with sulfonate anions, (f) and (g) with the sulfonylimide anions, and (e) chemical structure of LiTFSI.**Error! Bookmark not defined.**

Figure 1.2 (a) chemical structure of PEO; (b) schematic of the segmental motion assisted diffusion of Li^+ in the PEO matrix, the circles represent the ether oxygens of PEO; [57] chemical structure of polyether-based liquid polymers (c) PEGDMA and (d) PEGMEA, ester-based liquid monomers (e) PETMP and (f) PETA.....**Error! Bookmark not defined.**

Figure 1.3 Schematic illustration of the synthetic process of SIPE membrane by crosslinking the monomer of LiSTFSI, PTMP and PETA within a PP nonwoven fabric supporting membrane by a photo-initiated thiol-ene click reaction. [64].....**Error! Bookmark not defined.**

Figure 1.4 (a) Schematic showing the procedure of in situ hydrolysis and interaction mechanisms among PEO chains and MUSiO_2 ; [75] (b) schematic illustration of TiO_2 -grafted nanohybrid polymer electrolyte with cross-linked branching structure. [76]....**Error! Bookmark not defined.**

Figure 1.5 Historical development of active fillers. [85].....**Error! Bookmark not defined.**

Figure 1.6. Crystal structures of (a) Perovskite-type LLTO, (b) NASICON-type LAGP, (c) Garnet-type LLZO, and (d) thio-LISICON-type LGPS. (Other atoms such as titanium, germanium, zirconium and phosphorus are inside tetrahedra or octahedra) [148].....**Error! Bookmark not defined.**

Figure 1.7 (a) Schematic illustration and digital image of the composite electrolyte prepared by casting the mixed solution containing ionic liquid N-methyl-N-propylpyrrolidinium

bis(fluorosulfonyl)imide (C3mpyrFSI), LiFSI, poly(diallyldimethylammonium) chloride (PDADMA) and LiTFSI on PVDF fibrous matrix; [165] (b) the schematic illustration of the preparation of the LOF-CPE, which was fabricated by sandwiching the resulting LOF between two PEO electrolyte films, followed with vacuum-assisted thermal lamination process; [167] (c) schematic illustration of the fabrication, composition and operation of the es-PVPSI nanofiber-based membrane by electrospinning the polymer solution composed of nanoscale mixed PVDF-HFP and LiPSI. [9]**Error! Bookmark not defined.**

Figure 1.8 (a) The schematic diagram for the fabrication procedure of the solid composite electrolyte, where PDA-coated TiO₂ nanofillers were incorporated into PEO matrices to form the composite electrolyte; [173] (b) schematic picture of synthetic processes of 3D-CPEs, designed and manufactured with LLTO nanofibrous network as a nano-backbone in PEO matrix by hot-pressing and quenching, and voltage profiles of Li plating and stripping cycling for the bare solid polymer electrolyte and 3D-CPE. [177]**Error! Bookmark not defined.**

Figure 1.9 (a) Schematic of synthesis procedure of s@LLAZO-PEGDA polymer electrolyte by grafting the silane-modified LLAZO nanofibers with polymer matrix, providing fast and non-tortuous Li⁺ conductive pathways with percolated s@LLAZO network within the composite electrolyte, (b) cycling performance (at 1C) and (c) rate capability (0.2–10 C) of all-solid-state Li|LiFePO₄ cell operated at 25 °C by using the composite electrolyte with 50 wt.% s@LLAZO nanofibers; [182] (d) photographs of Boston ivy and a schematic diagram of the mechanism of action of PEO and LLZO–DI–Ca²⁺, which mimics Boston ivy, and schematic illustration showing the reaction route of PEO/LLZO–DI–Ca²⁺, (e) cycling stability of the Li|PEO/LLZO NFs–DI–Ca²⁺/LiTFSI|LiFePO₄ and Li|PEO/LLZO NFs/LiTFSI|LiFePO₄ cells at 0.5 C. [183]

.....**Error! Bookmark not defined.**

Figure 1.10 (a) Schematic illustration for the preparation of LLZTO/ PVDF-PEO-LiTFSI solid composite electrolytes by introducing inorganic ceramic LLZTO particles into electrospun PVDF nanofibers and then coating the membrane with PEO/LiTFSI polymer complex, (b) cycling performance of Li/Li symmetric batteries with 0LLZTO/PVDF-PEO-LiTFSI and 10LLZTO/PVDF-PEO-LiTFSI composite electrolytes under 0.3 mA cm^{-2} , (c) long-term cycling performances of Li/LiFePO₄ cells with pure PEO-LiTFSI electrolyte, 0LLZTO/ PVDF-PEO-LiTFSI and 10LLZTO/PVDF-PEO-LiTFSI composite electrolytes under 1 C. [185].....**Error! Bookmark not defined.**

Figure 1.11 (a) Cartoon of ion motion in a polymer host; [189] (b) transformation of a polymer electrolyte with a non-percolative arrangement of highly ordered regions to a percolative arrangement of disordered regions as in plasticized electrolytes. Percolative network of disordered regions provide fast ion transport pathways for the mobile ion; [194] (c) basic mechanisms of the Li ion transfer across crystalline polymer and crystalline polymer with inorganic fillers; [58] (d) diagram for the effects of inert and active fillers for Li⁺ conductive pathway within polymer electrolytes. [14]**Error! Bookmark not defined.**

Figure 3.1. Schematic illustration of the chemical synthetic process of LiSTFSI..... **Error! Bookmark not defined.**

Figure 3.2. (a) ¹HNMR and (b) ¹³CNMR spectra of KSTFSI.**Error! Bookmark not defined.**

Figure 3.3. (a) ¹HNMR, (b) ¹³CNMR, and (c) ¹⁹FNMR spectra of LiSTFSI.**Error! Bookmark not defined.**

Figure 3.4. Schematic of synthesis procedure of plasticized SIPE membrane reinforced with PAN-NFs, with a crosslinked amorphous network within the polymer electrolyte, providing fast Li^+ conductive pathways.**Error! Bookmark not defined.**

Figure 3.5. (a) Ionic conductivity versus molar ratio of $[\text{EO}]/[\text{Li}^+]$ for the crosslinked solid polymer electrolyte series at room temperature; (b) FTIR spectra of LiSTFSI, PEGDA and dry SIPE ($[\text{EO}]/[\text{Li}^+]=24$).**Error! Bookmark not defined.**

Figure 3.6. (a) EIS profiles of dry SIPE and SIPE-x at room temperature; (b) Ionic conductivity and Young's modulus versus PC weight ratio for dry SIPE and SIPE-x; (c) Stress-strain curves of PAN-NFs, SIPE-2.5 and SIPE-2.5-PAN; and (d) TGA curves of PAN-NFs, dry SIPE and SIPE-2.5-PAN from 20 to 600 °C.**Error! Bookmark not defined.**

Figure 3.7. SEM images of top view of (a) PAN-NFs and (b) SIPE-2.5-PAN; (c) Digital image of SIPE-2.5-PAN; and (d) SEM image of the cross-section of SIPE-2.5-PAN. **Error! Bookmark not defined.**

Figure 3.8. (a-g) Digital images of bending test for SIPE-2.5-PAN membrane. **Error! Bookmark not defined.**

Figure 3.9. (a) Arrhenius plots of dry SIPE, SIPE-x and SIPE-2.5-PAN membranes; (b) Time-dependent response of DC polarization for $\text{Li}|\text{SIPE-2.5-PAN}|\text{Li}$ symmetric cell (inset is the EIS plots before and after polarization); and (c) Linear sweep voltammetry curves of SIPE-2.5 and SIPE-2.5-PAN.**Error! Bookmark not defined.**

Figure 3.10. (a) EIS profiles of SIPE-2.5 and SIPE-2.5-PAN membranes; (b) time-dependent response of DC polarization curve for the $\text{Li}|\text{SIPE-2.5}|\text{Li}$ symmetric cell (inset is the EIS plots before and after polarization).**Error! Bookmark not defined.**

Figure 3.11. (a) LSV curve and (b) CV curve of Li|SIPE-2.5-PAN|stainless steel cell at room temperature.**Error! Bookmark not defined.**

Figure 3.12. Lithium plating/stripping cycles of symmetric (a-b) Li|SIPE-2.5-PAN|Li and (c) Li|SIPE-2.5|Li cells at different current densities.**Error! Bookmark not defined.**

Figure 3.13. Schematic illustration of (a) lithium dendrite formation phenomenon between SIPE-2.5 membrane and Li metal; and (b) lithium dendrite suppression effect between SIPE-2.5-PAN membrane and Li metal.**Error! Bookmark not defined.**

Figure 3.14. SEM images of (a) and (b) fresh Li metal surface; (b) and (c) Li metal surface after cycling in Li|SIPE-2.5-PAN|Li symmetric cell; (e) and (f) Li metal surface after cycling in Li|SIPE-2.5|Li symmetric cell.**Error! Bookmark not defined.**

Figure 3.15. (a) Cycling performance at current density of 0.2 C of all-solid-state Li|SIPE-2.5|LFP and Li|SIPE-2.5-PAN|LFP cells operated at 25 °C; (b) Charge-discharge curves of 1st, 50th and 100th cycles of all-solid-state Li|SIPE-2.5-PAN|LFP cell at current density of 0.2 C; (c) Rate capability and (d) Charge-discharge profiles (0.2-5 C) of all-solid-state Li|SIPE-2.5-PAN|LFP cell operated at 25 °C; (e) Cycling performance and (f) EIS evolution curves of all-solid-state Li|SIPE-2.5-PAN|LFP cell at current density of 1C operated at 25 °C..... **Error! Bookmark not defined.**

Figure 3.16. Charge-discharge curves of solid-state Li|SIPE-2.5|LFP cell at 1st, 50th and 100th cycles, 0.2 C @ 25°C.**Error! Bookmark not defined.**

Figure 4.1. Schematic illustration of the chemical synthetic process of LiSTFSI..... **Error! Bookmark not defined.**

Figure 4.2. (a) ¹HNMR and (b) ¹³CNMR spectra of KSTFSI.**Error! Bookmark not defined.**

Figure 4.3. (a) ^1H NMR, (b) ^{13}C NMR, and (c) ^{19}F NMR spectra of LiSTFSI.**Error! Bookmark not defined.**

Figure 4.4. Schematic of synthesis procedure of plasticized SICE membrane with a well-crosslinked inorganic-organic network, providing fast Li^+ conductive pathways.....**Error! Bookmark not defined.**

Figure 4.5. (a and b) SEM images and (c) XRD pattern of calcinated LLAZO NFs.**Error! Bookmark not defined.**

Figure 4.6. (a) SEM image and EDAX mapping of La, Zr, O, Si elements of s@LLAZO NFs; (b) FTIR spectra of PEGDA, PEGMEA, LiSTFSI and SICE₃₀; (c) EIS profiles of SICE_x with different s@LLAZO NF contents at room temperature; (d) Stress–strain curves of SICE_x at room temperature.....**Error! Bookmark not defined.**

Figure 4.7. FTIR spectra of silane, LLAZO and s@LLAZO NFs.**Error! Bookmark not defined.**

Figure 4.8. Ionic conductivities of SICEs with s@LLAZO NFs and pristine LLAZO NFs at different filler contents.....**Error! Bookmark not defined.**

Figure 4.9. (a) EIS profiles and (b) Arrhenius plots of SICE₀, SICE₃₀ and p-SICE₃₀; (c) linear sweep voltammetry curves of p-SICE₃₀ membrane at room temperature; (d) time-dependent response of DC polarization curve for the Li|p-SICE₃₀|Li symmetric cell (inset is the EIS plots before and after polarization) at 60 °C; (e) lithium plating/stripping cycles of symmetric Li|p-SICE₃₀|Li cell at different current densities under room temperature.**Error! Bookmark not defined.**

Figure 4.10. DSC curves tested from -80 to 100 °C of SICE₀, SICE₃₀ and p-SICE₃₀ membranes.**Error! Bookmark not defined.**

Figure 4.11. LSV curve of Li|p-SICE₃₀|stainless steel cell at room temperature. **Error! Bookmark not defined.**

Figure 4.12. (a) SEM image of the cross-section of p-SICE₃₀ membrane; (b) cycling performance at current density of 0.2 C of all-solid-state Li|p-SICE₃₀|LFP and liquid-state Li|LiPF₆|LFP cells operated at room temperature; (c) and (d) charge–discharge curves of 1st, 150th and 300th cycles of all-solid-state Li|p-SICE₃₀|LFP and liquid-state Li|LiPF₆|LFP cells at current density of 0.2 C; (e) rate capability and (f) charge-discharge profiles (0.2-5 C) of all-solid-state Li|p-SICE₃₀|LFP cell operated at room temperature; SEM images of (g) fresh Li metal surface, (h) Li metal surface after 300-cycling in all-solid-state Li|p-SICE₃₀|LFP cell and (i) Li metal surface after 300-cycling in liquid-state Li|LiPF₆|LFP cell. **Error! Bookmark not defined.**

Figure 4.13. SEM image of the cross-section of p-SICE₃₀ membrane and EDAX mapping of C, O, La, and Zr elements. **Error! Bookmark not defined.**

Figure 4.14. Digital images of p-SICE₃₀ membrane. **Error! Bookmark not defined.**

Figure 5.1. Schematic of fabrication procedure of all-solid-state Li-S battery with garnet-type CPE coated S cathode and Li anode, in which the LLAZO NFs was manufactured by electrospinning with high temperature calcination. **Error! Bookmark not defined.**

Figure 5.2. (a) SEM image and (b) XRD pattern of calcinated LLAZO NFs; (c) Ionic conductivity versus filler content and (d) Stress–strain curves of the CPEs at room temperature. **Error! Bookmark not defined.**

Figure 5.3. SEM image and EDAX mapping of La, Zr, O elements of LLAZO NFs..... **Error! Bookmark not defined.**

Figure 5.4. (a) FTIR spectra of PEGDA, PEGMEA, LLAZO NFs and CPE-x with different content fillers; (b) EIS profiles of CPE-x with different content fillers at room temperature.

.....**Error! Bookmark not defined.**

Figure 5.5. (a) Arrhenius plots and (b) DSC curves of CPE membranes; (c) time-dependent response of DC polarization curve for the Li|CPE-2|Li symmetric cell (inset is the EIS plots before and after polarization) at 60 °C; (d) linear sweep voltammetry curves of CPE-2 membrane at room temperature; (e) and (f) lithium plating/stripping cycles of symmetric Li|CPE-2|Li and Li|CPE-0|Li cells at different current densities under room temperature. ...**Error! Bookmark not defined.**

Figure 5.6. Time-dependent response of DC polarization curve for the Li|CPE-x|Li symmetric cell (inset is the EIS plots before and after polarization, and x=0, 1, 3, 4, 5) at 60 °C.....**Error! Bookmark not defined.**

Figure 5.7. TGA curves of CPE-0 and CPE-2 from 0 to 800 °C. ...**Error! Bookmark not defined.**

Figure 5.8. Lithium plating/stripping cycles of symmetric Li|CPE-0|Li cell at current densities of (a) 0.05 mA cm⁻² and (b) 0.1 mA cm⁻² under room temperature.....**Error! Bookmark not defined.**

Figure 5.9. SEM images of the surface morphologies of (a) S cathode and (b) CPE-2 coated S cathode.**Error! Bookmark not defined.**

Figure 5.10. SEM images of the cross-section of (a) CPE-2 coated S cathode and (b) CPE-2 coated Li metal anode; (c) cycling performance at current density of 0.1 C of all-solid-state Li|CPE-0|S and Li|CPE-2|S cells operated at room temperature; (d) charge–discharge curves of 1st, 50th and 100th cycles of all-solid-state Li|CPE-2|S cell at current density of 0.1 C; (e)

Rate capability (0.05–1 C) of all-solid-state Li|CPE-2|S cell operated at room temperature.**Error!**
Bookmark not defined.

Figure 5.11. The EDAX mapping of F, Zr elements of CPE-2 coated S cathode of the SEM image on Figure 4(a), the S cathode used here did not contain any LiTFSI/ TEGDME solution and LLAZO NFs.**Error! Bookmark not defined.**

Figure 5.12. Charge–discharge curves of 1st, 50th and 100th cycles of all-solid-state Li|CPE-0|S cell at current density of 0.1 C.**Error! Bookmark not defined.**

Figure 5.13. SEM images of (a) fresh Li metal surface, (b) Li metal surface after 100-cycling in all-solid-state Li|CPE-0|S cell and (c) Li metal surface after 100-cycling in all-solid-state Li|CPE-2|S cell.**Error! Bookmark not defined.**

Figure 5.14. (a) SEM image of uncycled Li metal anode from Li|CPE-0|S cell with (b) EDAX mapping of S element; (c) SEM image of cycled Li metal anode from Li|CPE-0|S cell with (d) EDAX mapping of S element; (e) SEM image of cycled Li metal anode from Li|CPE-2|S cell with (f) EDAX mapping of S element.**Error! Bookmark not defined.**

CHAPTER 1: OVERVIEW OF SOLID POLYMER ELECTROLYTES

1.1 Introduction of solid-state electrolyte

Rechargeable lithium-ion batteries (LIBs) were first introduced into the commercial market by Sony in the early 1990s and are considered the most significant achievement in the development of electrochemical energy storage technologies. [1-3] In conventional LIBs, liquid electrolytes composed of lithium salts (e.g., LiPF_6) dissolved in a mixture of carbonate-based organic solvents (e.g., EC, DMC, and EMC) are usually employed with separators (e.g., PP and PE) for lithium-ion transportation between the cathode and anode. [1, 4, 5] However, detrimental impacts have been aroused by applying organic liquid electrolytes and separators, which further hinder the future development of advanced LIBs. On the one hand, the highly volatile, flammable and easy-leaking organic solvent-based liquid electrolytes can lead to severe safety concerns like fire and explosion, which limit the long-term durability of LIBs, causing higher cost and requirements on packaging and state-of-charge monitoring circuits. [2, 6, 7] On the other hand, with rapidly increasing requirements for portable electronic devices, electric and hybrid vehicles, current commercial liquid-state LIBs are insufficient to fulfill future demands due to their limited power and energy densities, inadequate safety, poor inadequate lifespan, and high cost. [8-11]

Recently, enormous research has been shifted to lithium metal batteries based on high-voltage cathode materials and highly active lithium metal. Lithium metal is regarded as one of the most promising anode candidates for next-generation energy storage systems owing to the high theoretical specific capacity (3860 mA h g^{-1}), low density (0.59 g cm^{-3}), and the lowest redox potential (-3.04 V vs. standard hydrogen electrode). [12-14] Conventional organic liquid

electrolytes are usually electrochemically unstable at high voltage, and decomposition of lithium salts and side reactions between liquid electrolytes and Li anode could generate unstable solid electrolyte interface (SEI), leading to decreasing Coulombic efficiency and irreversible capacity loss. [4] Moreover, uncontrolled Li dendrites formation due to uneven lithium ions deposition on the surface of Li metal during charging process can pierce the separator upon cycling and eventually cause catastrophic battery failure. [9, 15] Therefore, replacement of organic liquid electrolytes and separators with solid-state electrolytes in lithium metal batteries will not only help to overcome the persistent problems of current liquid-state batteries, but also offer possibilities for developing safer, long-term and high-performance lithium metal batteries with using high-voltage cathode materials and Li metal anode. [10] In general, solid-state electrolytes used in rechargeable batteries are classified into inorganic solid ceramic electrolytes and organic solid polymer electrolytes. [7, 16, 17] This thesis mainly focuses on organic solid polymer electrolytes.

1.2 Development of organic solid polymer electrolytes

The development of organic solid polymer electrolytes can be traced back to 1973, when P.V. Wright et al. discovered the ionic conducting capability of complexes formed by semi-crystalline poly(ethylene oxide) (PEO) and certain common alkali salts (e.g., NaI) in the absence of liquid solvent. [1, 18, 19] Later, M. Armand explored that the ionic conductivity of polymer electrolytes was related to the amorphous phases of the PEO/salt systems, where ionic conductivity can be improved by suppressing the crystallinity of polymer system. [20] After that, increasing attention has been aroused on solid polymer electrolyte development and targeting their use in electrochemical applications, especially LIBs, owing to their high safety, good processability,

excellent flexibility and enhanced mechanical compliance with the electrodes. [7, 21, 22]

Currently, solid polymer electrolytes can be divided into two categories, including conventional dual-ion conducting polymer electrolytes and novel single-ion conducting polymer electrolytes (SIPEs).

Conventional polymer electrolytes, consisting of a polymer solid matrix (e.g., polyethylene oxide (PEO), polyacrylonitrile (PAN), polyvinylidene fluoride (PVDF)) with alkali metal salts (e.g., LiTFSI, LiPF₆, LiClO₄, LiBF₄, LiCF₃SO₃), are usually dual ion conductors, in which both Li⁺ cations and their counter anions migrate during the charging/discharging process. [23-28]

Unfortunately, the overall conductivity is predominated by the motion of counter anions, which have a 4 times greater mobility than Li⁺ cations. This results in lithium-ion transference numbers (t_{Li^+}) of lower than 0.5 for dual-ion polymer electrolyte systems. [29] As a result, a severe concentration polarization effect is generated due to the accumulation/depletion of salt near the electrodes during battery operation, which brings higher internal impedance and subsequent cell failure. In an effort to enhance t_{Li^+} , SIPEs were fabricated by anchoring charge delocalized anions on a polymeric backbone, as side chains of a crosslinked system. The immobilization of the anions on the polymer backbone means that only Li⁺ cations moving between the cathode and anode, with t_{Li^+} close to unity. [1, 30] However, immobilizing the anions typically results in large decreases in the ionic conductivity of the SIPE system owing to the strong ion pairing between Li ions and anions. [7, 30] It is reported that the highest bulk ionic conductivity of a typical dry SIPE is approximately 10^{-5} S cm⁻¹ at 60 °C, which is nearly three orders of magnitude lower than that of a standard liquid electrolyte at room temperature. [31-33] Thus, plasticizers of cyclic carbonates with high dielectric constant and flash point, or inorganic ceramic fillers are often introduced to improve the ionic conductivity of SIPEs for high-

performance lithium batteries.

1.2.1 Lithium-ion transference number

SIPEs, which can be fabricated by anchoring charge delocalized anions as side chains on polymeric backbones, can avoid the problems of severe concentration polarization effect happened in binary electrolyte systems for Li batteries. In previous work, conventional polymer electrolytes employing lithium salts are usually dual-ion conductors, in which both Li^+ cations and their counter anions migrate during the charging/discharging process. Thus, the lithium-ion transference number for a binary salt electrolyte is simply defined as the fraction of the ionic conductivity that is carried by lithium ions compared with the total ionic conductivity carried by both lithium ions and their counter ions, and can be calculated by:

$$t_{\text{Li}^+} = D^+ / (D^- + D^+) \quad (1.1)$$

where t_{Li^+} is the lithium-ion transference number, D^+ is the lithium-ion diffusion coefficient, and D^- is the anion diffusion coefficient. [29] It is obvious that t_{Li^+} is highly related to the diffusion of lithium ions and counter anions. However, the overall conductivity of dual-ion polymer electrolytes is predominated by the motion of counter anions that have greater mobility than lithium cations. This happens due to the strong preferential solvation of lithium ions over their counter anions, leading to a bulkier solvation shell around lithium ions compared to typical counter anions. [34] Therefore, lithium-ion transference numbers of binary polymer electrolyte systems are undesirably low, always lower than 0.5, typically ranging from 0.1 to 0.4 in real applications. [35, 36] As a result, a severe concentration polarization effect is generated because anions migrate in the opposite direction of the lithium ions and eventually accumulate on the electrode surface, which brings higher internal impedance, decreased energy density and lower

charging rates. [1, 37] Moreover, according to Chazalviel's space-charge theory in 1990, an electric field could be induced near the Li anode region due to concentration polarization, which will cause uneven distribution of lithium-ion flux and lead to growth of lithium dendrites. [38, 39] In contrast, SIPEs with immobilized anions along polymer backbones can maintain high lithium-ion transference numbers, which is desirable for advanced Li metal batteries. It has been demonstrated by Monroe and Newman's simulations in 1994 that no concentration gradients occurred in polymer electrolyte systems with a unity t_{Li^+} , in which the utilization of active electrode materials could remain near 100%, even at relatively high current density, further improving the energy and peak-power densities for these batteries. [1, 39]

1.2.2 Polymer matrices

1.2.2.1 Lithium monomers

In a polymerized SIPE system, anions from the organic lithium monomer are usually covalently bonded on the polymer backbone as side chains in order to obtain a near-unity lithium-ion transference number. Therefore, the chemical group selection for better degree of negative charge distribution of anions is of great importance for high Li^+ cation dissociation in a polymer system. It is reported that enlarging the conjugation structure of organic anions or attaching strong electron-withdrawing groups adjacent to the anionic units can enhance delocalization of negative charges and minimize the anion/cation dissociation energy barrier. [40, 41] In 1995, Armand et al. demonstrated that employment of a strong electron-withdrawing group perfluorinated alkyl ($RF-$) instead of the common hydrocarbon alkyl ($R-$) group in the $R-SO_2-$ based anions could dramatically reduce the anion/cation interaction strength and increase the degree of Li^+ cation dissociation, further improving the ionic conductivity of SIPEs. [42, 43] In this part of thesis,

three types of commonly-used organic lithium monomers are discussed based on the different anion structures, including carboxylate ($-\text{CO}_2^-$), sulfonate ($-\text{SO}_3^-$), and sulfonylimide ($-\text{SO}_2\text{N}(-)\text{SO}_2-$).

Carboxylate anions as the counterpart of the Li^+ cations have first been investigated in 1980s, where a homopolymer of organic lithium monomer was synthesized by Tsuchida et al. with three main chemically functional moieties: a flexible carbon main chain, an oligo(oxyethylene) matrix for fast ion conduction and a carrier source for Li^+ cation (**Figure 1.1a**). [44] However, the conductivity of this organic lithium homopolymer was extremely low, around $3.2 \times 10^{-9} \text{ S cm}^{-1}$ at $30 \text{ }^\circ\text{C}$, and it was improved to $2 \times 10^{-7} \text{ S cm}^{-1}$ by increasing the segmental motion of the polymer matrix through the copolymerization of oligo(oxyethylene) methacrylate (MEO_7) with the organic lithium monomer. Recently, Zhou et al. reported a novel hyperbranched SIPE with poly(ethylene glycol)₉ (PEG) segments and carboxylate groups (**Figure 1.1b**), which provided a relatively high ionic conductivity of $1.2 \times 10^{-4} \text{ S cm}^{-1}$ at $85 \text{ }^\circ\text{C}$ with a superior lithium-ion transference number of 0.86. [45] This polymer system not only possessed a low glass transition temperature (below $0 \text{ }^\circ\text{C}$) to enable a large number of ion-conductible amorphous regions, but also accommodated plenty of alternating coordination anions and PEG segments in the molecules to synergistically accelerate the transportation of lithium ions, exhibiting a high potential of applying organic lithium monomers with carboxylate groups as the cation source of SIPEs for Li metal batteries.

Compared with the carboxylate anions, the sulfonate groups show higher degree of negative charge delocalization and thus lower interaction strength with Li-ions. [1, 46] Increasing efforts have been devoted to developing sulfonate-based SIPEs for high-performance all-solid-state Li batteries. In the early 1990s, Zhang et al. developed a blend polymer electrolyte composed of a

lithium polymer with hydrocarbon alkyl sulfonate (**Figure 1.1c**) and a polyethylene oxide (PEO)-based polymer, which showed a low ionic conductivity of $1.8 \times 10^{-7} \text{ S cm}^{-1}$ at room temperature with a relatively high glass transition temperature range of 245 to 265 °C. [47] After the introduction of polar acrylonitrile (AN) group into the molecular chains of the blend polymer electrolyte, the ionic conductivity was further improved to $1.1 \times 10^{-6} \text{ S cm}^{-1}$ due to the enhanced polarity of polymer matrix for the dissociation of the Li^+ cation, and relieved crystallization of oligoether sidechain for higher Li^+ ion transportation. Furthermore, as shown in **Figure 1.1d**, a new type of SIPE of poly(hexafluorobutyl methacrylate-co-lithium allyl sulfonate) (P (HFMA-co-ASLi)) was first prepared and followed with soaking in the organic plasticizer solution of ethylene carbonate (EC)/propylene carbonate (PC). [40] At the presence of strong electron-withdrawing fluorine units in polymer matrix, a high lithium ionic conductivity of $10^{-4} \text{ S cm}^{-1}$ can be reached at 80 °C with excellent cycling performance at high temperature, which could be attributed to the good thermal stability, high mechanical properties and high lithium-ion transference number of this novel type of SIPEs.

Another important member of anions for organic lithium monomers, sulfonylimide anions, has raised enormous attention in the development of SIPEs due to their expanded conjugated structure, which can delocalize the negative charges in a relatively efficient manner and hence decrease the binding energy with Li-ions. [48-50] In 1986, Armand initially applied lithium bis(trifluoromethanesulfonyl)imide (LiTFSI, **Figure 1.1e**), a binary lithium salt with sulfonylimide anion, into solid polymer electrolyte for Li batteries due to its highly delocalized negative charge over to a large conjugate structure, together with a very flexible chemical structure responsible for good plasticizing ability for the polymer matrix. [51] After the recognition of good chemical and electrochemical properties of LiTFSI in liquid and polymer

electrolytes, trifluoromethanesulfonamide anion was successfully introduced into various synthesized organic lithium monomers for the development of high-performance SIPEs. [32, 52-54] Since 2011, Armand and co-workers have fabricated and characterized the lithium poly(4-styrenesulfonyl(trifluoromethylsulfonyl)imide) (PLiSTFSI, **Figure 1.1f**), and reported a variety of novel blend and copolymer SIPEs based on the monomer of lithium (4-styrenesulfonyl(trifluoromethylsulfonyl)imide) (LiSTFSI) as the cation source. [32, 49, 55] **Figure 1.1g** shows the SIPE structure polymerized by improved organic lithium monomer with a more delocalized anionic structure by replacing an =O group in the SO₃Li structure of LiSTFSI by a strong electron-withdrawing group of =NSO₂CF₃, and achieved a Li-ion conductivity as high as $1.35 \times 10^{-4} \text{ S cm}^{-1}$ at 90 °C when blending with PEO as SIPEs. [56]

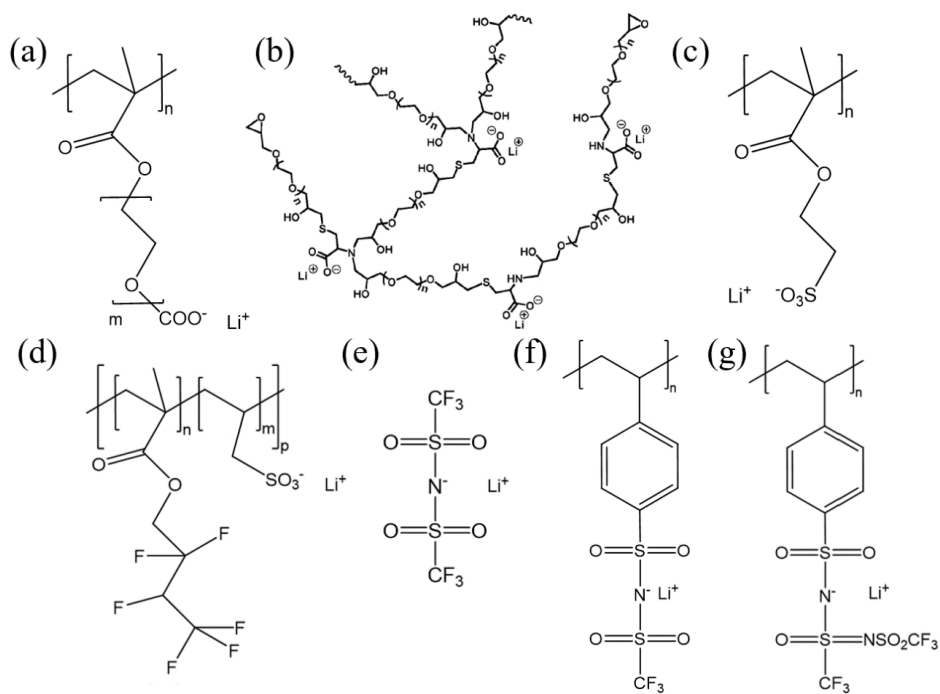


Figure 1.1 Chemical structures of single-ion conducting polymer electrolytes: (a) and (b) with carboxylate anions, [45] (c) and (d) with sulfonate anions, (f) and (g) with the sulfonylimide anions, and (e) chemical structure of LiTFSI.

1.2.2.2 Polymer backbones

As mentioned above, the chemical structure of lithium-ion conducting monomers plays an important role in determining the activation energy required for Li^+ cation dissociation.

Meanwhile, the polymer backbone architecture also has great effect on the dissociation and transportation of Li^+ ions, as well as the overall mechanical performance and thermal stability of SIPEs. [32, 54]

SIPEs are derived from the development of polymer electrolytes composed of organic polymer matrices and binary lithium salts, which initially occurred in 1973 when Wright et al. found PEO containing alkali-metal salts could provide notable ionic conductivity. [18] Since then, various PEO-based polymer electrolytes have been extensively explored and developed due to their decent Li^+ cation dissociation ability, good mechanical properties, and good compatibility with electrodes. As shown in **Figure 1.2a**, the repeat unit of PEO molecular chain is $-\text{CH}_2-\text{CH}_2-\text{O}-$, which exhibits strong donor nature and allows lithium-ion complexation with low dissociation barrier. **Figure 1.2b** illustrates the Li^+ ion transportation facilitated by the segmental motion of the PEO backbone where Li^+ ions coordinated with ether oxygen atoms can migrate from one coordination site to another with the assistance of the PEO segmental motion, thereby realizing the conduction of Li^+ ions under the action of an electric field. [3, 57]

However, since PEO is a semi-crystalline polymer at room temperature and the segmental motion in the crystalline region is very limited so that the ionic conduction of PEO-based polymer electrolytes mainly occurs in the amorphous region, resulting in insufficient ion dynamics for Li^+ ion transportation and a low ionic conductivity of about 10^{-8} - 10^{-6} S cm^{-1} at room temperature. [3, 58] It is generally agreed that decreasing the crystallinity of polymer matrix or increasing the working temperature above the melting temperature (T_m) for fast main-

chain segmental movements can dramatically enhance the ionic transport in PEO-based polymer electrolytes. [59] Oligomeric polyester-based liquid polymers with different molecular weights, such as poly(ethylene glycol) dimethacrylate (PEGDMA, **Figure 1.2c**) and poly(ethylene glycol) methyl ether acrylate (PEGMEA, **Figure 1.2d**), and ester-based liquid monomers, such as pentaerythritol tetrakis(3-mercaptopropionate) (PETMP, **Figure 1.2e**) and pentaerythritol tetraacrylate (PETA, **Figure 1.2f**), have been widely applied as the polymer backbone in polymer electrolytes, especially in SIPE systems because they can directly polymerize with organic lithium monomers to form crosslinked or copolymerized SIPEs. [60-64]

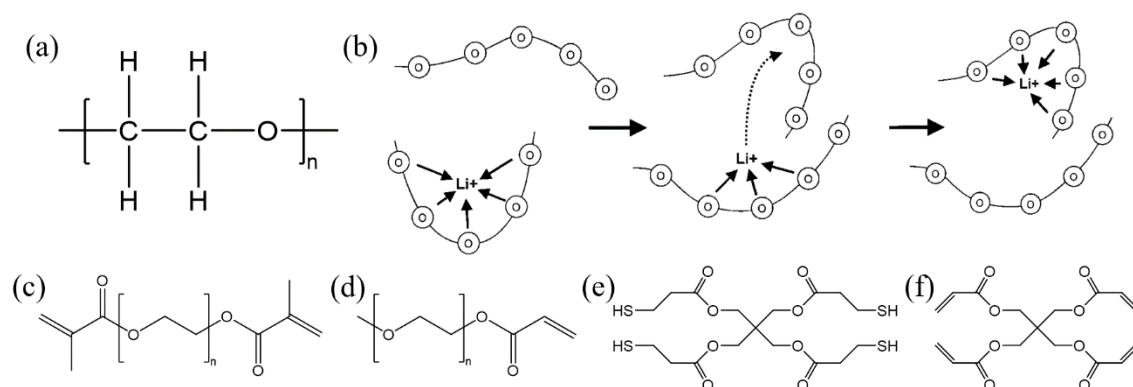


Figure 1.2 (a) Chemical structure of PEO; (b) Schematic of the segmental motion assisted diffusion of Li⁺ in the PEO matrix, the circles represent the ether oxygens of PEO; [57] Chemical structure of polyether-based liquid polymers (c) PEGDMA and (d) PEGMEA, ester-based liquid monomers (e) PETMP and (f) PETA.

It is known that crosslinking is an approach to simply linking one polymer chain to another through a covalent bond. Compared to homopolymerization or copolymerization, polymerization by crosslinking can increase dynamic storage modulus of polymer electrolytes and, at the same time, improve thermal stability and tensile strength. [7] As shown in **Figure 1.3**, Meng and co-workers developed a novel SIPE by directly polymerizing the monomer of LiSTFSI, crosslinkers

of PETMP and PETA into a crosslinked network structure within a polypropylene nonwoven fabric as supporting membrane by a photo-initiated thiol-ene click reaction. [64] The crosslinked SIPE presented a superior ionic conductivity of 0.84 mS cm^{-1} at room temperature and a near-unity lithium-ion transference number of 0.93 after solvent soaking process.

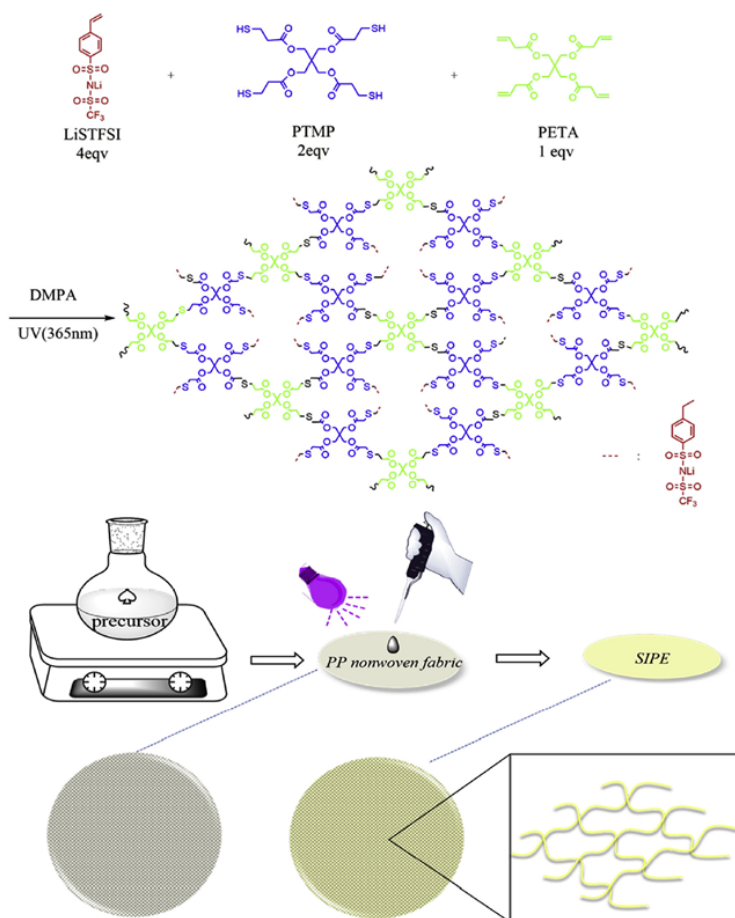


Figure 1.3 Schematic illustration of the synthetic process of SIPE membrane by crosslinking the monomer of LiSTFSI, PTMP and PETA within a PP nonwoven fabric supporting membrane by a photo-initiated thiol-ene click reaction. [64]

1.3 Additives

1.3.1 Organic plasticizers

The high lithium-ion transference number of SIPEs is realized by immobilized the anions. However, immobilizing the anions typically results in dramatically reduced ionic conductivity for SIPEs owing to the strong ion pairing between Li ions and anions. Therefore, although SIPEs have superior lithium-ion transference number, their bulk ionic conductivity is extremely low, typically no more than 10^{-5} S cm⁻¹ at 60 °C, which is nearly three orders of magnitude lower than that of a standard liquid electrolyte at room temperature. One of the most simple and effective ways to increase the ionic conductivity of SIPEs is to introduce organic plasticizers of cyclic carbonates with high dielectric constant and flash point. [65] The polymerized polymer network can accommodate the added plasticizer and hence integrate the advantages of both liquid and solid electrolytes. Compared to the dry SIPEs, plasticized SIPEs can provide high ionic conductivity up to 10^{-3} S cm⁻¹ via enhanced polymer chain segmental motion and increased ion pair dissociation under room temperature, and offer another transport mechanism for cationic species by facilitating vehicular transport of the solvated cation. [66, 67] Furthermore, the polymerized networks with added plasticizer facilitate a relatively homogeneous Li⁺ ion flux, minimizing volumetric changes of Li deposition and blocking lithium dendrite formation. [68] In addition, introduced organic plasticizer can improve the wettability of the SIPEs and enhance the interfacial stability with better electrode-electrolyte interfacial contact. However, plasticized SIPEs possess a trade-off between improved conductivity and compromised mechanical strength. The lack of mechanical strength could induce short-circuiting failure during cycling. [46] To improve the strength of SIPEs, reinforcement agents, such as inorganic ceramic fillers, organic metal frames and mechanically robust standing membranes, can be introduced into the

crosslinked system to improve their mechanical robustness. [69]

1.3.2 Inorganic fillers

1.3.2.1 Inert fillers

One effective way to improve both the ionic conductivity and mechanical robustness of SIPEs is to introduce inorganic fillers into the polymer matrix, which have three main functions: i) reduce the crystallinity of polymer system, ii) enhance the interfacial stability between electrode and electrolyte, and iii) improve the mechanical property of polymer matrix. [17] As a result, inorganic filler-incorporated SIPEs have attracted increasing attention in recent years owing to their excellent electrochemical performance in lithium batteries. [70] There are two main categories of inorganic fillers, inert and active fillers, where inert fillers are usually oxide ceramic fillers without Li source and they do not transport Li ions, and active fillers are ceramics containing Li element with high Li ion conductivity.

Various types of inert oxide ceramic sphere particles such as silica (SiO_2), aluminum oxide (Al_2O_3), titanium oxide (TiO_2), etc., have been extensively studied and applied into the polymer matrix for better electrochemical performance and strong mechanical properties. [71-73] Al_2O_3 particles were first incorporated as an inorganic filler additive into a PEO polymer electrolyte for Li batteries by Weston et al. in 1982. Although the inert fillers cannot conduct Li ions, the Al_2O_3 -incorporated polymer electrolyte showed increased mechanical strength and enhanced ionic conductivity. [74] After that, more research on inorganic inert fillers has been explored for better electrochemical and cycling performance of Li batteries. Cui et al. reported a new method to prepare inert oxide ceramic-polymer electrolyte via in situ synthesis of ceramic particles inside polymer electrolyte, where a much stronger chemical/mechanical interactions were produced

between monodispersed ultrafine SiO₂ (MUSiO₂) nanospheres and poly(ethylene oxide) (PEO) chains. [75] As shown in **Figure 1.4a**, the introduction of ultrafine MUSiO₂ significantly suppressed the crystallization of PEO and thus facilitated polymer segmental motion and improved degree of LiClO₄ dissociation, leading to good ionic conductivities of $1.2 \times 10^{-3} \text{ S cm}^{-1}$ at 60 °C and $4.4 \times 10^{-5} \text{ S cm}^{-1}$ at 30 °C. **Figure 1.4b** illustrated a homogeneous TiO₂-grafted nanohybrid polymer electrolyte (NHPE) with a crosslinked branching structure, which composed of ion-conducting poly(ethylene glycol) methyl ether methacrylate (PEGMEM) and non-polar stearyl methacrylate (SMA). [76] Due to the highly monodispersed TiO₂ nanocrystals, interfacial interactions between particles and polymer matrix were effectively enhanced, which decreased the crystallization of ethylene oxide (EO) groups and facilitated continuously interconnected ion-conducting channels. The TiO₂-grafted NHPE exhibited superior electrochemical properties with an ionic conductivity of $1.1 \times 10^{-4} \text{ S cm}^{-1}$ at 30 °C, a high lithium-ion transference number and excellent interfacial compatibility with the lithium electrode.

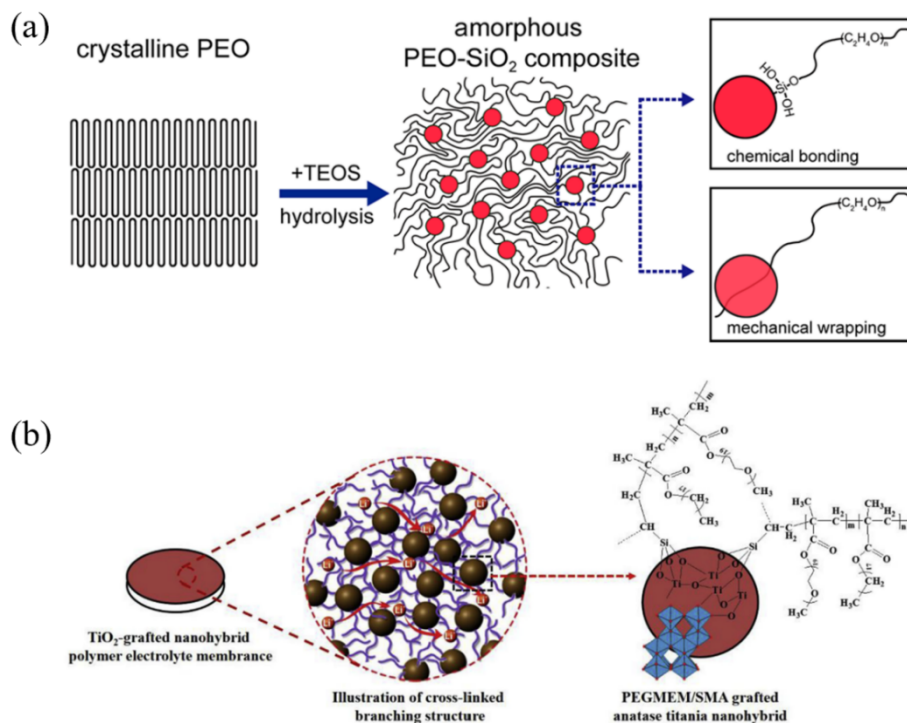


Figure 1.4 (a) Schematic showing the procedure of in situ hydrolysis and interaction mechanisms among PEO chains and MUSiO₂; [75] (b) Schematic illustration of TiO₂-grafted nanohybrid polymer electrolyte with cross-linked branching structure. [76]

1.3.2.2 Active fillers

Active fillers are mainly originated from inorganic solid ceramic electrolytes, and the incorporation of active fillers into polymer-based electrolytes can not only reduce the crystallinity of the polymer host and provide mechanical support to enhance electrochemical stability, but also facilitate new Li⁺ ion transfer channels to improve ionic conductivity.

The development of active fillers shown in **Figure 1.5** can date back to as early as the 1830s, when Faraday observed an exponential increase in conductivity with increasing temperature in solid Ag₂S and PbF₂, after which Warburg discovered the Na⁺ ion mobility in a glass and measured the first Na⁺ ion transference number with Tegetmeier in the study of ionic conductors.

[77-79] Later in 1914, Tubandt and Lorenz determined the ionic conductivity of α -AgI by testing the ionic contributions to the overall conductivity, where the total current that passed through the sample was simply detected by DC measurements and the number of transferred ions through AgI was measured by the change in masses of the electrodes and thereby determined ionic contributions to the conductivity. [80] Another key milestone was the discovery of the concept of point defects focused on understanding and visualizing ionic and electronic transport in solids in 1920s. [81] Later in 1960s, Takahashi first introduced the term solid-state ionics (SSIs) working on the transport of mobile ions, mixed ions and electrons in solid materials, and their physical and chemical properties. Since then, the evolution and the incorporation of SSIs into batteries experience a rapid increase. To date, the representative active fillers mainly include solid oxide electrolytes, e.g., perovskite-type, NASICON-type, garnet-type, LISICON-type, and solid sulfide electrolytes such as thio-LISICON-type ($\text{Li}_{10}\text{GeP}_2\text{S}_{12}$, LGPS), both of which have been extensively developed owing to their high ion conductivity at room temperature, high Li-ion transference number close to unity, good electrochemical stability, robust mechanical strength and excellent thermal stability. [22, 82-84]

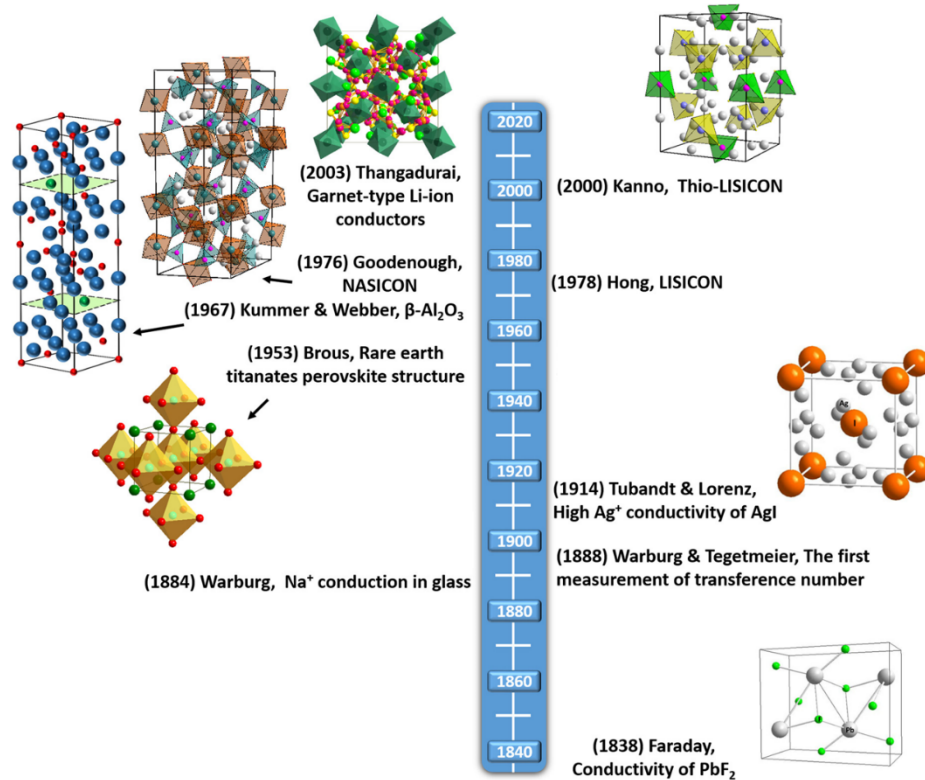


Figure 1.5 Historical development of active fillers. [85]

The typical structure of perovskite oxides has a general formula of ABO_3 (space group: $Pm\bar{3}m$), where A-site ions at the corners of a cube are normally rare-earth or alkaline-earth elements, and B ions at the center are usually transition-metal elements, and the oxygen atoms are at the face-centered positions. [86, 87] Early in 1953, Brous reported a rare earth titanate ($EuTiO_3$) with perovskite structure, which exhibited high dielectric constant, ferroelectric transition and dielectric hysteresis. [88] Later in 1971, Perovskite-type ceramic materials have been originally reported by Takahashi and Iwahara. [89, 90] Currently, the representative perovskite ceramic is the lithium lanthanum titanate $Li_{3x}La_{(2/3)-x}TiO_3$ (LLTO, **Figure 1.6a**) ($0.03 \leq x \leq 0.167$) by replacing the A-site with both La^{3+} and Li^+ while the B-site with Ti^{4+} , which was first reported by A.G. Belous in 1987. [91] LLTO has aroused much interest among researchers owing to its high

bulk lithium-ion conductivity of up to 10^{-3} S cm^{-1} at room temperature and good electrochemical stability in high voltages. [92] However, it has been demonstrated that LLTO is unstable below about 1.8 V and Ti^{4+} can be reduced when contacting with Li metal at around 1.5 V versus Li^+/Li , which limits its practical applicability in all-solid-state lithium batteries with low potential anode materials. [10, 93] A possible strategy to address these problems is applying thin proactive or protective layers on the surface of LLTO to avoid the direct contact with lithium metal. [94]

The Na super ionic conductor (NASICON)-type ceramics generally have an $\text{AM}_2(\text{PO}_4)_3$ formula with the A site occupied by Na and the M site occupied by Ge, Zr or Ti. [89] NASICON-type compounds were first studied in the 1960s and then termed ‘NASICON’ after the development of $\text{Na}_{1+x}\text{Zr}_2\text{P}_{3-x}\text{Si}_x\text{O}_{12}$ with a rhombohedral structure (space group of $\text{R}\bar{3}\text{c}$) through a high-temperature solid-state reaction method early reported by Goodenough et al. in 1976. [95, 96] The typical NASICON-type ceramic shown in **Figure 1.6b** possesses a rigid and three-dimensional (3D) crystalline network structure, which consists of corner-sharing MO_6 octahedra and PO_4 tetrahedra structures in the three dimensionally linked interstitial space. Na ions occupy at interstitial sites and transport along the c-axis. [85, 97] This material can maintain its original structure and turn into a NASICON-type lithium-ion conductor when Na^+ is replaced by Li^+ in a general formula of $\text{LiM}_2(\text{PO}_4)_3$. [98] While, the ionic conductivity of this Li-ion-based ceramics decreases due to the ionic radius difference between Na^+ and Li^+ . [99] One possible method to improve the ionic conductivity of NASICON-type Li^+ conductor is doping Al into the ceramic structure, $\text{Li}_{1+x}\text{Ti}_{2-x}\text{Al}_x(\text{PO}_4)_3$ ($x = 0.3$ or 0.4 , LATP), which can achieve a high ionic conductivity up to 10^{-3} S cm^{-1} at room temperature. [100, 101] This is due to that aliovalent substitution could directly increase the Li ion concentration and mobility. [17] Currently, NASICON-type materials

are considered as suitable active fillers for high-voltage solid electrolyte batteries owing to their relatively wide electrochemical stability window up to 5 V versus Li^+/Li and excellent water and air resistance. [102-104] However, the main drawback of NASICON-type ceramics is their chemical instability, which is similar to the perovskite-type ceramic that Ti^{4+} is easily reduced to Ti^{3+} when contacting with lithium metal. [105]

The original garnet-type ceramics exhibit a general chemical formula of $\text{A}_3\text{B}_2(\text{XO}_4)_3$, containing three crystallographically distinct cation coordination environments with the A (e.g., Ca, Mg, Y, La or rare earth), B (e.g., Al, Fe, Ga, Ge, Mn, Ni or V), and X (e.g., Si, Ge or Al) cations in eight, six, and four oxygen-coordinated cation sites. [17, 106, 107] The $\text{A}_3\text{B}_2(\text{XO}_4)_3$ ceramic crystallizes in a face-centered cubic structure with the space group of $\text{Ia}\bar{3}\text{d}$ (space group number 230). [108] The first solid garnet-type Li^+ conductor, $\text{Li}_5\text{La}_3\text{M}_2\text{O}_{12}$ ($\text{M} = \text{Nb}$ or Ta), was reported by Thangadurai et al. in 2003 and possessed a lithium-ion conductivity of $\sim 10^{-6} \text{ S cm}^{-1}$ at room temperature with activation energy of no more than 0.6 eV. [105, 109] Later by replacing La and M sites with other metal ions, a series of garnet-type materials has been generated, such as $\text{Li}_6\text{ALa}_2\text{M}_2\text{O}_{12}$ ($\text{A} = \text{Ca}$, Sr or Ba ; $\text{M} = \text{Nb}$ or Ta), $\text{Li}_{5.5}\text{La}_3\text{M}_{1.75}\text{B}_{0.25}\text{O}_{12}$ ($\text{M} = \text{Nb}$ or Ta ; $\text{B} = \text{In}$ or Zr) and the cubic systems $\text{Li}_7\text{La}_3\text{Zr}_2\text{O}_{12}$ and $\text{Li}_{7.06}\text{M}_3\text{Y}_{0.06}\text{Zr}_{1.94}\text{O}_{12}$ ($\text{M} = \text{La}$, Nb or Ta). [110-119] Among different types of solid garnet-type ceramics, the one with zirconium element $\text{Li}_7\text{La}_3\text{Zr}_2\text{O}_{12}$ (LLZO, **Figure 1.6c**), first reported by R. Murugan et al. in 2007, has been widely investigated owing to high lithium-ion conductivity (10^{-4} - $10^{-3} \text{ S cm}^{-1}$) at room temperature, low activation energy ($\sim 0.31 \text{ eV}$), excellent stability against lithium metal, wide electrochemical window ($\sim 5 \text{ V}$), and high mechanical strength. [117, 120] LLZO has two different crystal structures, including low-temperature tetragonal structure with relatively low lithium-ion conductivity and high-temperature cubic structure with high lithium-ion conductivity. [111, 121]

At present, the lithium-ion conductivity of LLZO can reach to 9.24 mS cm^{-1} through different doping methods, which is highly promising for all-solid-state Li battery development. [122-126] However, the practical application of this garnet-type ceramic electrolytes is hindered via the following issues: 1) instability in the moisture and air by reacting with water and carbon dioxide to generate Li_2CO_3 and LiOH ; 2) poor contact and wetting ability at the electrode-electrolyte interfaces; 3) severe formation and propagation of lithium dendrites at the grain boundaries. [98, 127, 128] Therefore, more and specific research should be emphatically considered to improve the overall performance of garnet-type ceramic electrolytes.

Another class of lithium super ionic conductor called LISICON ($\text{Li}_{14}\text{ZnGe}_4\text{O}_{16}$) was developed by H.Y.P. Hong in 1978. [99] The general formula of LISICON-type ceramic is $\text{Li}_{16-2x}\text{M}_x(\text{TO}_4)_4$ ($0 < x < 4$) with M as a divalent cation (eg., Mg^{2+} , Zn^{2+}) and T as a tetravalent cation (eg., Si^{4+} , Ge^{4+}). The crystal structure of LISICON-type ceramics can be considered as a distorted hexagonal close-packing of oxygen atoms with all cations (such as Li^+ and P^{5+}) being tetrahedrally coordinated. [86, 129] Oxygen atoms are packing perpendicular to the c-axis and Li^+ ions locate at LiO_4 tetrahedra diffuse between these tetrahedra and interstitial sites (PO_4 network), arranging into one-dimensional (1D) parallel chains along the a-axis. [130]

$\text{Li}_{14}\text{ZnGe}_4\text{O}_{16}$ and their derivatives have an orthorhombic unit cell with the space group of Pnma, similar to $\gamma\text{-Li}_3\text{PO}_4$. [131] They exhibit very high conductivity at improved temperatures, e.g., $1.25 \times 10^{-1} \text{ S cm}^{-1}$ at $300 \text{ }^\circ\text{C}$, but extremely low conductance of $1 \times 10^{-7} \text{ S cm}^{-1}$ at room temperature because formed defective compound Li_4GeO_4 can trap mobile lithium ions through the immobile sublattice. [132-134] In order to enhance the ionic conductivity, a new LISICON-type family has been developed via aliovalent substitution of P^{5+} by Si^{4+} or Ge^{4+} in the $\gamma\text{-Li}_3\text{PO}_4$, having a general formula of $\text{Li}_{3+x}\text{Y}_{1-x}\text{X}_x\text{O}_4$ ($\text{Y} = \text{P, As, V, Cr}$ and $\text{X} = \text{Si, Ge, Ti}$). [135] As a

result, excess Li^+ ions occupying interstitial sites are created in the structures and decrease the migration distance of neighboring Li^+ ions, thus improving the conductance. [136, 137]

However, LISICON-type ceramics have the similar problems like garnet-type ceramics that they are easy to react with lithium metal and carbon dioxide, which increase the requirements for production and storage. [133]

Research into sulfide-type solid ceramics started in 1984, when Tachez et al. discovered a crystalline structure of Li_3PS_4 . [138] Later in 1986, $\text{Li}_2\text{S-SiS}_2$ -type ceramics have been extensively studied by doping the $\text{Li}_2\text{S-SiS}_2$ system with Li_3PO_4 , achieving the Li-ion conductivity up to $6.9 \times 10^{-4} \text{ S cm}^{-1}$. [139-142] In 2000, Kanno et al. introduced another sulfide-type lithium-ion conductor, thio-LISICON, with similar crystalline structure with LISICON made by replacing O^{2-} ions with S^{2-} ions. [143] The larger atomic size and higher polarizability of S^{2-} increase the lattice volume and weaken the binding of Li ion to the host framework, thus enlarging the ion-transport channel and achieving a very high ionic conductivity over $10^{-4} \text{ S cm}^{-1}$ at room temperature. [144, 145] Currently, one of the most promising thio-LISICON materials is the $\text{Li}_{10}\text{GeP}_2\text{S}_{12}$ (LGPS, **Figure 1.6d**), a newly developed thio-LISICON-type ceramic, first reported by N. Kamaya et al. in 2011. [31] At room temperature, its ionic conductivity can reach to $1.2 \times 10^{-2} \text{ S cm}^{-1}$, which is comparable to liquid electrolytes. However, sulfide SSEs are generally unstable and produce H_2S when exposed to air or moisture. [86] Partial substitution of O^{2-} for S^{2-} can decrease the rate of H_2S generation but could also reduce the ionic conductivity. Another way to solve this problem is to dope metallic oxides (such as Fe_2O_3 , ZnO , and Bi_2O_3) act as the H_2S absorbents to thio-LISICON-type ceramics to suppress the H_2S generation.[146]

Nonetheless, all aforementioned active fillers have suffered from their rigidity and brittleness,

exhibiting poor mechanical compliance with the electrodes and leading to large interfacial resistance. [147] Combing active fillers with polymer matrix for solid-state electrolytes can not only avoid the disadvantages of inorganic ceramics, but also enhance the mechanical strength and improve the ionic conductivities of the solid polymer electrolytes.

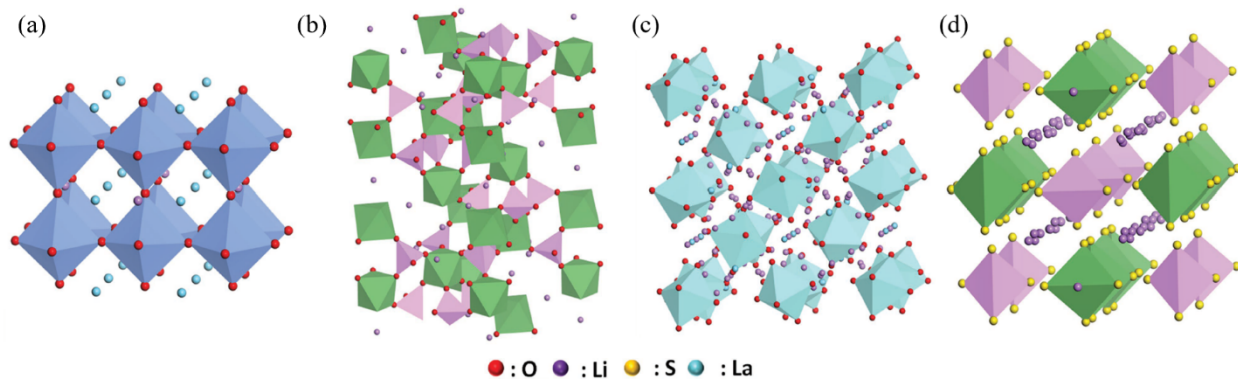


Figure 1.6. Crystal structures of (a) Perovskite-type LLTO, (b) NASICON-type LAGP, (c) Garnet-type LLZO, and (d) thio-LISICON-type LGPS. (Other atoms such as titanium, germanium, zirconium and phosphorus are inside tetrahedra or octahedra) [148]

1.3.3 Nanofiber-shaped additives

Nanotechnology has arisen as a fascinating discipline working on the phenomena and functions of matters within the dimensional range of 0.1-100 nm during the past decades. [149] Abundant nanotechnologies have been studied and practiced in various areas of human life from the view of science and technology. [150] At present, nanostructured materials are at the leading edge of the rapidly developing field of materials science and engineering due to their unique properties that result from the size-dependent structural behaviors, which have been widely applied in the fields of energy storage. [151-153] Among currently available nanostructured materials, ultrafine nanofibers, carrying a range of novel physical and chemical properties, have attracted considerable attention on overcoming many limitations present in organic solid-state polymer

electrolytes. [154, 155] Different strategies have been created and developed for nanofiber fabrication, including thermal-induced phase separation, drawing, template synthesis, self-assembly, etc., among which electrospinning is of considerable significance as a rapid, simple, and continuous process in manufacturing nanofibers, as well as formulating their two-dimensional (2D) and three-dimensional (3D) structures. [156-159] Besides, this straightforward, continuous, and cost-effective method can launch ultrathin nanofibers from an enormous number of materials, including polymers, inorganic ceramics, composites, etc. [160, 161] Moreover, electrospun nanofibers and their assemblies are much more favorable in providing high specific surface area, large surface-to-volume ratio, tunable porosity with uniform pores distribution, and the ability of desired chemical functionalization for various applications. [162-164]

1.3.3.1 Organic nanofibers

The development of solid polymer electrolytes, composed of a polymer matrix and lithium source, and also possibly various additives, is increasingly growing for all-solid-state Li batteries owing to their high safety, good processability, excellent flexibility and enhanced mechanical compliance with the electrodes. However, the mechanical properties of polymer electrolytes are usually insufficient for high-performance Li batteries, especially after adding organic plasticizer for improving their ionic conductivity. Electrospun polymeric nanofibers has been regarded as a good supporting membrane to enhance the mechanical strength of polymer-based electrolytes. Wang et al designed a composite polymer electrolyte (CPE) by combing polymerized ionic liquids (polyILs) with electrospun PVDF nanofiber membrane to afford electrolytes with high ionic liquid content and greatly increased Li ion transference number. [165] **Figure 1.7a** indicated that the incorporation of electrospun PVDF nanofibers effectively improves the

mechanical strength of the CPEs, forming flexible electrolytes with superior mechanical properties. In addition, the effect of crystallinity degree of PVDF nanofibers has been studied by Nakazawa et al, revealing that the solid polymer electrolyte composed of PVDF nanofibers with higher β -phase crystallinity showed higher ion conductivity and higher lithium ion transference number than the other ones with lower PVDF β -phase crystallinities. [166] Besides using the original polymer nanofiber membrane, novel lithiated organic nanofibers (LOF, **Figure 1.7b**) made by grafting branched polyethylenimine (bPEI) on the surface of PAN nanofibers via the chemical reaction between the amine groups of bPEI and the cyano groups ($C\equiv N$) of PAN have been used to improve the affinity of nanofibers to the polymer matrix. [167] The CPE was prepared by sandwiching the resulting LOF between two PEO electrolyte films, followed with vacuum-assisted thermal lamination process. The LOF-reinforced PEO composite electrolyte (LOF-CPE) with homogeneous percolation network and additional active Li^+ can not only enhance the tensile stress of the electrolyte to up to 8.9 MPa, but also form high-speed Li-ion conduction pathways, delivering an excellent ionic conductivity of $7.41 \times 10^{-5} S cm^{-1}$ at 30 °C. Electrospun polyamide 6 (PA6) nanofiber membrane with hierarchical structure, which was prepared by electrospinning the solution of PA6 and organic branching salt tetrabutylammonium chloride (TBAC), was also introduced into the PEO polymer matrix to prepare an all-solid-state composite electrolyte, with enhanced mechanical strength of up to 9.2 MPa. [168] The prepared Li/Li symmetric battery can be stably cycled for 1500 h under $0.3 mA cm^{-2}$ and 60 °C due to the improved safety and cycle stability. Some researchers also worked on directly embedding Li salts into electrospun polymer nanofibers, after which the obtained membranes were soaked by organic plasticizers to for the electrolyte for Li batteries. [9, 12] As shown in **Figure 1.7c**, Li et al reported a highly porous nanofiber SIPE membrane composed of nanoscale mixed

poly(vinylidene fluoride-co-hexafluoropropylene) (PVDF-HFP) and lithium poly(4,4'-diaminodiphenylsulfone, bis(4-carbonyl benzene sulfonyl)imide) (LiPSI), followed by soaking in the ethylene carbonate (EC)/dimethyl carbonate (DMC) (v:v = 1:1) solvent mixture. [9] The electrospun nanofiber membrane (es-PVPSI) showed high porosity, appropriate mechanical strength, and high thermal dimensional stability even at 300 °C. The resulting Li/LiFePO₄ cells using such a SIPE exhibit excellent rate capacity and outstanding electrochemical stability for 1000 cycles at least.

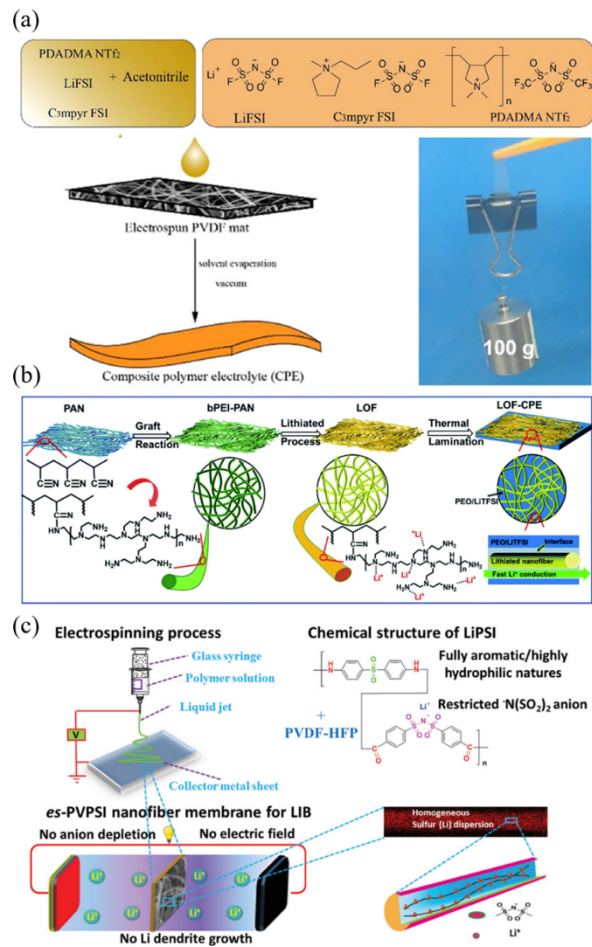


Figure 1.7 (a) Schematic illustration and digital image of the composite electrolyte prepared by casting the mixed solution containing ionic liquid N-methyl-N-propylpyrrolidinium bis(fluorosulfonyl)imide (C3mpyrFSI), LiFSI, poly(diallyldimethylammonium) chloride (PDADMA) and LiTFSI on PVDF fibrous matrix; [165] (b) Schematic illustration of the preparation of the LOF-CPE, which was fabricated by sandwiching the resulting LOF between two PEO electrolyte films, followed with vacuum-assisted thermal lamination process; [167] (c) Schematic illustration of the fabrication, composition and operation of the es-PVPSI nanofiber-based membrane by electrospinning the polymer solution composed of nanoscale mixed PVDF-HFP and LiPSI. [9]

1.3.3.2 Inorganic nanofibers

In order to improve the contact areas between the inorganic fillers and polymer matrices, enormous research has been conducted to prepare one-dimensional nanostructured fillers with high surface-to-volume ratios to promote ion conduction in SPEs. [169-172] Zhao et al reported a novel and efficient TiO_2 @polydopamine (PDA) fillers synthesized by coating PDA onto the surface of the TiO_2 nanofibers, which were then incorporated into PEO matrices to form the composite electrolyte, as shown in **Figure 1.8a**. [173] The composite electrolyte displays a higher ionic conductivity of $4.36 \times 10^{-4} \text{ S cm}^{-1}$ and a wider electrochemical window up to about 5 V. The assembled $\text{LiFePO}_4/\text{Li}$ ASSLIBs can deliver superior discharge specific capacities of 153.83 and 136.45 mAh g^{-1} at current densities of 0.5C and 2C, achieving good capacity retentions of 93.27% and 91.23% at 0.5C and 1C after 150 cycles, respectively. Besides nanofiber-shaped inert fillers, increasing efforts have been paid on developing strategies to reduce the grain boundary resistance of active fillers mentioned above, where the morphology of one-dimensional (1D) materials such as nanofibers could be beneficial for achieving closer packing and thus more effective densification during the sintering step. [8, 174, 175] Zhu et al fabricated a PEO-based composite solid polymer electrolyte filled with one-dimensional (1D) ceramic $\text{Li}_{0.33}\text{La}_{0.557}\text{TiO}_3$ (LLTO) nanofibers, which exhibited a high ionic conductivity of $2.4 \times 10^{-4} \text{ S cm}^{-1}$ at room temperature and a large electrochemical stability window of up to 5.0 V vs. Li/Li^+ . [176] Later, a self-standing 3D-CPE (**Figure 1.8b**), with LLTO nanofibrous network as a nano-backbone in PEO matrix by hot-pressing and quenching, was designed and manufactured by Nan's group. [177] The LLTO nano-backbone can not only enhance the mechanical properties and thermal stability of the electrolyte membrane but also increase its ionic conductivity. The resulting symmetric $\text{Li}|\text{3D-CPE}|\text{Li}$ cell was cycled at a current density of 0.1 mA cm^{-2} for over

800 h, which was possible due to the suppression of Li dendrite growth and reduced polarization. Study was also focused on the ionic conductivity and chemical interaction affected by oxygen vacancy formed during sintering under hydrogen atmosphere and different temperatures in LLTO ceramic nanofibers. [178]

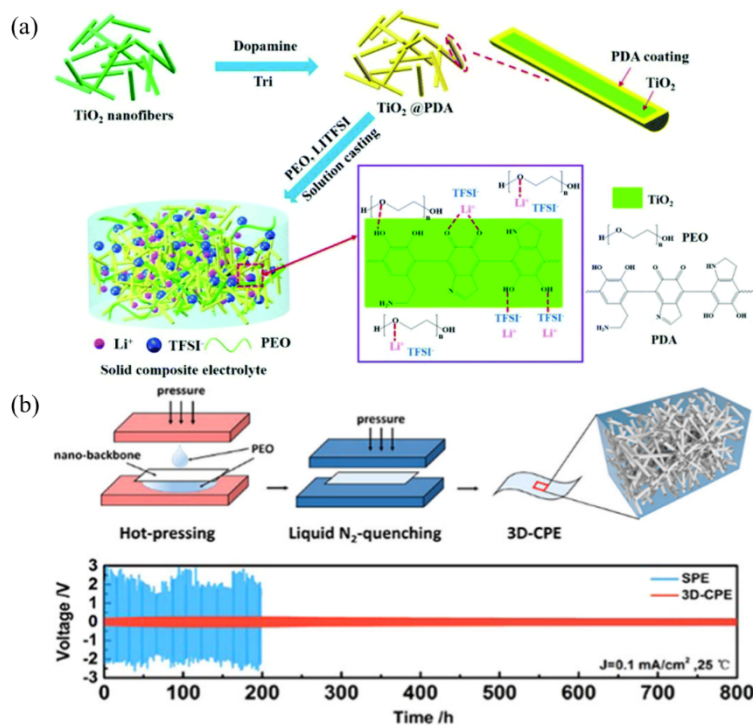


Figure 1.8 (a) The schematic diagram for the fabrication procedure of the solid composite electrolyte, where PDA-coated TiO_2 nanofillers were incorporated into PEO matrices to form the composite electrolyte; [173] (b) Schematic picture of synthetic processes of 3D-CPEs, designed and manufactured with LLTO nanofibrous network as a nano-backbone in PEO matrix by hot-pressing and quenching, and voltage profiles of Li plating and stripping cycling for the bare solid polymer electrolyte and 3D-CPE. [177]

Besides Perovskite-type LLTO nanofibers, garnet-type LLZO nanofibers and their derivatives are also popular inorganic fillers for solid polymer electrolytes to improve the ionic conductivity,

electrochemical stability and mechanical properties for ASSLBs development. [179, 180]

Monaca et al. reported an elastic solid electrolyte with a high ionic conductivity of $1.16 \times 10^{-4} \text{ S cm}^{-1}$ at 30 °C and a low activation energy of 0.308 eV by filling ionic-conductive polymers into well-aligned $\text{Li}_{6.4}\text{La}_3\text{Zr}_2\text{Al}_{0.2}\text{O}_{12}$ nanofiber films. [181] As shown in **Figure 1.9a**, Yan et al. has developed a new type of polymer electrolyte composed of silane-modified $\text{Li}_{6.28}\text{La}_3\text{Al}_{0.24}\text{Zr}_2\text{O}_{12}$ (s@LLAZO) nanofibers and poly(ethylene glycol) diacrylate (PEGDA), where the employment of the silane coupling agent eliminated the agglomeration effect and enabled the incorporation of a high content of LLAZO nanofibers (up to 70 wt%) with the polymer matrix, thereby resulting in a well-percolated, three-dimensional LLAZO network fully embedded in the PEGDA matrix. [182] **Figure 1.9b-c** have demonstrated that all-solid-state Li-metal batteries assembled with the developed polymer electrolyte can exhibit stable cycling performance for 250 cycles and extraordinary high rate capability (up to 10 C) at room temperature owing to the maximized utilization of fast Li^+ conductors (LLAZO) in the composite structure. Later, Chen's group reported bridging $\text{Li}_7\text{La}_3\text{Zr}_2\text{O}_{12}$ nanofibers (LLZO NFs) formed by grafting the Dynasylan IMEO (DI) on the surface and bonding with coordinatively unsaturated metal centers of Ca^{2+} , after which these Ca^{2+} bridge the modified LLZO NFs with PEO via the ether oxygen atoms they possess (**Figure 1.9d**). [183] It is indicated that the bridges built between the two phases, PEO and LLZO nanofibers, are effective to interface strengthening and guarantee rapid Li^+ conduction even after 900 cycles. The assembled $\text{Li}||\text{LiFePO}_4$ cell shown in **Figure 1.9e** can deliver excellent rate performance and cycling stability with capacity retention of 70.8% after 900 cycles at current density of 0.5 C.

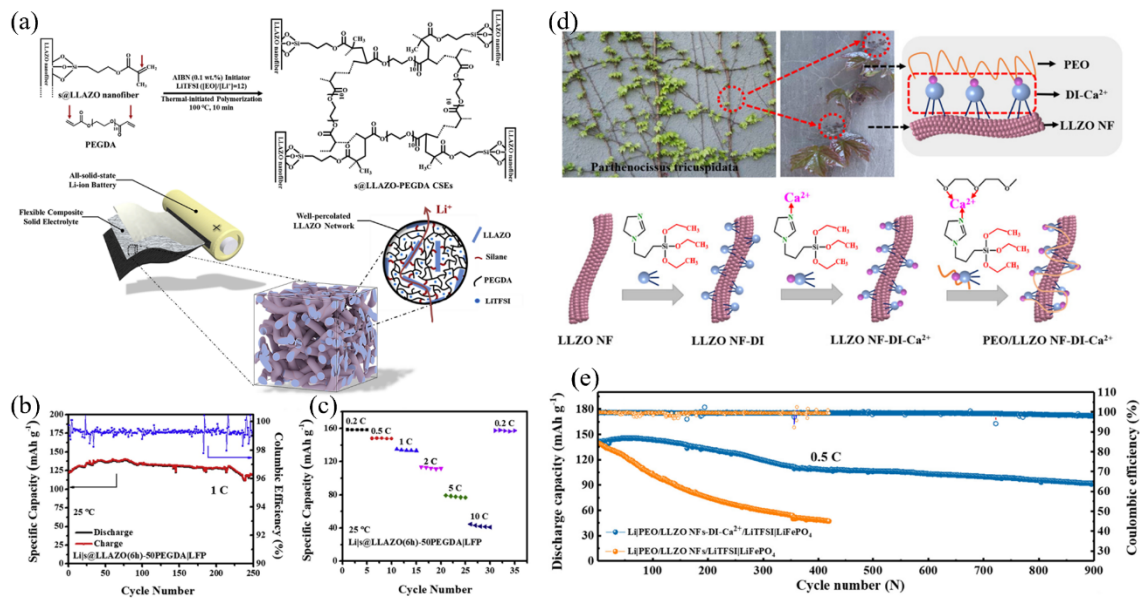


Figure 1.9 (a) Schematic of synthesis procedure of s@LLAZO-PEGDA polymer electrolyte by grafting the silane-modified LLAZO nanofibers with polymer matrix, providing fast and non-tortuous Li⁺ conductive pathways with percolated s@LLAZO network within the composite electrolyte, (b) Cycling performance (at 1C) and (c) rate capability (0.2–10 C) of all-solid-state Li|LiFePO₄ cell operated at 25 °C by using the composite electrolyte with 50 wt.% s@LLAZO nanofibers; [182] (d) Photographs of Boston ivy and a schematic diagram of the mechanism of action of PEO and LLZO–DI–Ca²⁺, which mimics Boston ivy, and schematic illustration showing the reaction route of PEO/LLZO–DI–Ca²⁺, (e) Cycling stability of the Li|PEO/LLZO NFs–DI–Ca²⁺/LiTFSI|LiFePO₄ and Li|PEO/LLZO NFs/LiTFSI|LiFePO₄ cells at 0.5 C. [183]

1.3.3.3 Inorganic-organic nanofibers

Enhanced inorganic/organic interfacial contact can help to maintain a uniform distribution of inorganic fillers within polymer system, which can further increase the ionic conductivity and electrochemical stability of SPEs. [184] Therefore, it is necessary to fabricate inorganic fillers in nanoscale. However, the agglomeration effect of added inorganic fillers becomes severer and

causes nonuniform distribution when their sizes decrease to nanoscale. Therefore, besides the surface modifications aforementioned, another effective way to address this issue is to directly embed inorganic filler particles into polymer nanofiber membranes by electrospinning, which can not only increase the content of inorganic fillers but also improve their uniformity in polymer system. A garnet-type ceramic filler LLZO@PAN CPE membrane, with an ultrathin thickness of $\sim 25 \mu\text{m}$ and a comparatively high conductivity of $1.60 \times 10^{-3} \text{ S cm}^{-1}$, was fabricated by crosslinking the precursor solution into the LLZO@PAN 3D electrospun backbone, where the 3D backbone improved the mechanical stability, and in-situ polymerization guaranteed good interfacial properties. [184] Gao et al. introduced inorganic ceramic $\text{Li}_{6.4}\text{La}_3\text{Zr}_{1.4}\text{Ta}_{0.6}\text{O}_{12}$ (LLZTO) particles into electrospun PVDF nanofibers and then coated the membrane with PEO/LiTFSI polymer complex to prepare composite electrolytes, as shown in **Figure 1.10a**. [185] The PVDF nanofibers with embedded LLZTO fillers can simultaneously reduce the crystallinity of the PEO polymer and provide a strong framework support for the composite electrolyte, thereby promoting the transmission of lithium ions and improving the lithium dendrite growth inhibition ability of the composite electrolyte. In addition, the uniform dispersion of garnet-type LLZTO active ceramic filler in the PVDF nanofiber membrane can enhance the interaction among PVDF, LLZTO and lithium salts, which promotes dissociation of the lithium salt, and further optimize the migration path of lithium ions. The ionic conductivity of the composite electrolyte is as high as $9.30 \times 10^{-4} \text{ S cm}^{-1}$ at $50 \text{ }^\circ\text{C}$, and the voltage of Li/Li symmetrical battery (**Figure 1.10b**) would not change significantly during 1200 h at 0.3 mA cm^{-2} . Additionally, the composite electrolytes exhibit good electrochemical stability with the capacity retention rate of 96% under 1 C after 500 cycles (**Figure 1.10c**). Perovskite-type LLTO was also embedded in PAN nanofibers for CPE fabrication. [186] In order to isolate the direct

contact between the chemically active Ti^{4+} in LLTO with lithium metal, PEO/LiTFSI electrolyte was filled into the pores of the PAN/LLTO nanofiber framework, thereby avoiding the occurrence of interfacial reactions, enhancing the electrochemical stability up to 4.8 V. Li et al designed and reported a high-performance quasi-solid-state electrolyte based on NASICON-type ceramic $Li_{1.3}Al_{0.3}Ti_{1.7}(PO_4)_3$ (LATP)|PVDF-HFP nanofibers. [187] This composite gel electrolyte shows a 3D porous network with significantly improved ionic conductivity up to 3.394 mS cm^{-1} , and the assembled Li|CGE|LFP solid-state battery can achieve a capacity retention up to 97% after 300 cycles at 0.5C, indicating its potential applications for high-performance energy storage devices.

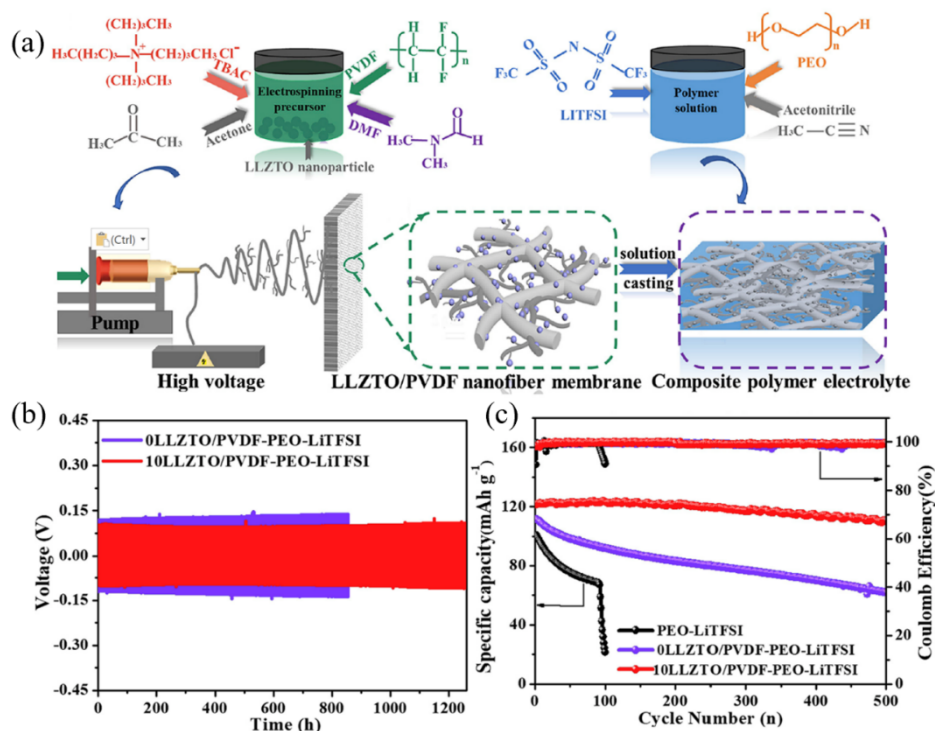


Figure 1.0 (a) Schematic illustration for the preparation of LLZTO/ PVDF-PEO-LiTFSI solid composite electrolytes by introducing inorganic ceramic LLZTO particles into electrospun PVDF nanofibers and then coating the membrane with PEO/LiTFSI polymer complex, (b) Cycling performance of Li/Li symmetric batteries with 0LLZTO/PVDF-PEO-LiTFSI and 10LLZTO/PVDF-PEO-LiTFSI composite electrolytes under 0.3 mA cm⁻², (c) Long-term cycling performances of Li/LiFePO₄ cells with pure PEO-LiTFSI electrolyte, 0LLZTO/ PVDF-PEO-LiTFSI and 10LLZTO/PVDF-PEO-LiTFSI composite electrolytes under 1 C. [185]

1.4 Li-ion conduction mechanisms

In a typical solid polymer electrolyte, the Li⁺ cations are responsible for the ionic conductivity. As shown in **Figure 1.11a**, cations can interconnect with functional groups of the host polymer chains, and hence move between neighboring coordinating sites by dissociative process for long range cation transportation. [188-190] Therefore, the Li ion transport highly depends on polymer

segmental motion and is faster in the amorphous regions compared to crystalline regions of the polymer host. [191] As shown in **Figure 1.11b**, amorphous regions of polymer matrix, e.g., semi-crystalline PEO, at ambient temperatures are usually below the percolation threshold, resulting in poor ionic conductivities for solid polymer electrolytes ($\leq 10^{-6}$ S cm⁻¹). After polymer electrolytes are plasticized via organic liquid solvent (high dielectric constant and low viscosity), the amorphous regions grow larger in number as well as in size due to decreased polymer crystallinity, leading to attainment of percolation threshold at room temperature. [192, 193] Thereby, percolative network with connected amorphous regions can provide fast ion conducting pathways and high ionic transportation. [194]

As mentioned above, the introduction of inorganic fillers (**Figure 1.11c**) influences the recrystallization kinetics of polymer chains and reduce their crystallinity, further facilitating Li ion transfer and improving ionic conductivity at low temperature. [58, 195] In addition, owing to their large surface area, Lewis acid-base interaction can be induced between inorganic filler surface and anions or polymer segments, which can also promote the lithium ion transference number and mechanical properties of polymer electrolytes. [14] However, the dominant lithium ions conductive mechanisms are slightly different in electrolytes containing inert fillers or active fillers, which is shown in **Figure 1.11d**. Inert fillers (e.g., SiO₂, Al₂O₃) are usually oxide ceramic fillers without Li source but abundant oxygen atoms and hydroxy groups on the surface. Lewis acid-base interaction between inert filler surface and polymer matrix can form favorable Li⁺ conducting pathway at the interface between inert particles and polymer matrix, called interface Li ion conduction. As for the active fillers, they are usually ceramics containing Li element so that active fillers themselves can transport lithium ions. Relative to the polymer region, conductive active fillers have higher ionic conductivity and Li ions tend to move through

conductive fillers phase, called inorganic phase Li ion conduction, then followed with interface and polymer phase Li ion conduction.

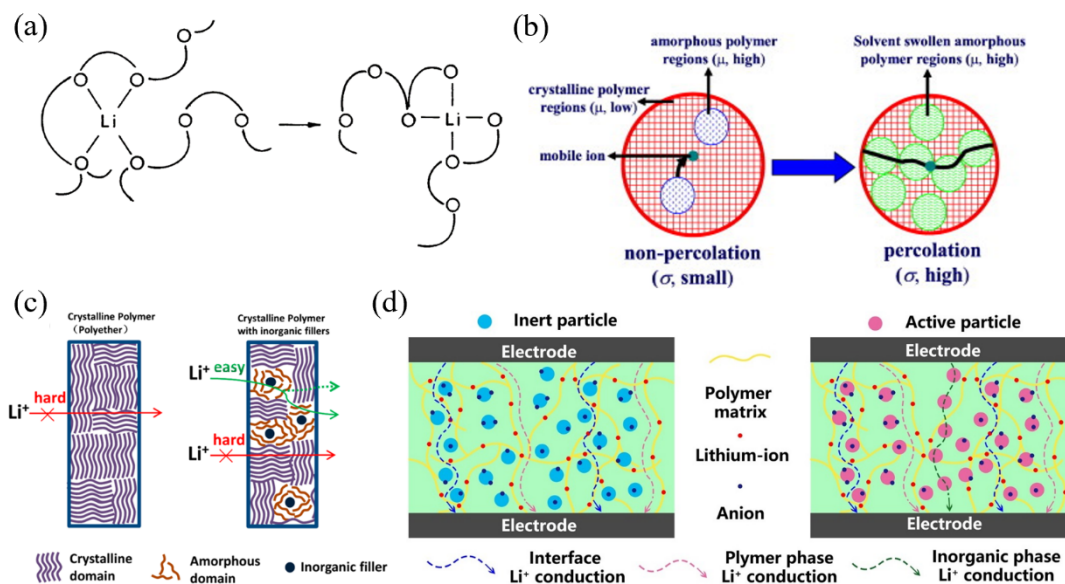


Figure 1.11 (a) Cartoon of ion motion in a polymer host; [189] (b) Transformation of a polymer electrolyte with a non-percolative arrangement of highly ordered regions to a percolative arrangement of disordered regions as in plasticized electrolytes. Percolative network of disordered regions provide fast ion transport pathways for the mobile ion; [194] (c) Basic mechanisms of the Li ion transfer across crystalline polymer and crystalline polymer with inorganic fillers; [58] (d) Diagram for the effects of inert and active fillers for Li⁺ conductive pathway within polymer electrolytes. [14]

Vogel-Tammann-Fulcher (VTF) and Arrhenius models can be used to quantify the ionic conductance behavior for solid polymer electrolytes based on the different ionic conduction mechanisms in the polymer matrix. Vogel-Tammann-Fulcher (VTF) model is an important phenomenological model used to study the ion transport mechanism in polymer electrolytes,

which is derived by quasi-thermodynamics with free volume and configurationally entropy, as described in the following equation:

$$\delta(T) = \delta_0 T^{1/2} \exp\left(\frac{-B}{T-T_0}\right) \quad (1.2)$$

where B is the pseudo-activation energy (expressed in units of E_a/k_B) and T_0 is the reference temperature (10~50 K below the kinetic glass transition temperature (T_g)). [196] VTF model explains that Li^+ ion transportation is highly correlated with the polymer segmental motion, which is considered more suitable in describing the ion transportation behavior for dry polymer electrolyte since ions can only be transferred or hopped into new adjacent coordinated sites with the presence of local free volume at temperatures above T_g . [197, 198] Therefore, the ion conduction mechanism in organic polymer electrolytes can be regarded as the combination of short-range ion hopping and long-range motions of polymer chains. [17] Arrhenius model for ion transport describing the relationship between the ionic conductivity and temperature can be explained by the follow equation:

$$\delta = A \exp(-E_a/k_B T) \quad (1.3)$$

where δ is the ionic conductivity, A is the dc conductivity of pre-exponential factor, E_a is the activation energy, k_B is the Boltzmann constant, and T is the absolute temperature. [16]

Arrhenius model is commonly used to describe the Li^+ transportation mechanism in plasticized polymer electrolytes, inorganic filler-incorporated polymer electrolytes and inorganic ceramic electrolytes. It is seen that the ionic conductivity is inversely proportional to the activation energy, which is defined as the energy barrier between adjacent available sites. Thus, the diffusion of Li^+ ions in pure Arrhenius-behavior polymer electrolyte is mainly realized by ion hopping mechanism through the connected available vacancies rather than polymer dynamics. [6]

CHAPTER 2: RESEARCH OBJECTIVES

This dissertation focuses on exploring and designing nanofiber-reinforced quasi-solid-state polymer electrolytes for high-performance Li metal batteries, with the aim of improving the ionic conductivities, electrochemical stabilities, and Li^+ conducting pathways of polymer electrolytes and cycling performance of Li metal batteries while enabling the safe operation. The main research topics include:

2.1 Polyacrylonitrile Nanofiber-Reinforced Flexible Single-Ion Conducting Polymer Electrolyte for High-Performance, Room-Temperature All-Solid-State Li-Metal Batteries

As abovementioned, the ionic conductivity of single-ion conducting polymer electrolytes (SIPes) by immobilizing charge delocalized anions along polymer matrix is extremely low due to the strong ion pairing between Li ions and anions. Addition of a plasticizer into the polymer network can dramatically increase the ionic conductivity via enhanced polymer chain segmental motion and increased ion pair dissociation under room temperature. However, plasticized SIPes usually face a trade-off between conductivity and mechanical strength, which could cause short-circuiting failure during cycling. To address this challenge, a crosslinked SIPE system with an appropriate ratio of $[\text{EO}]/[\text{Li}^+]$ and sufficient amount of plasticizer will be firstly design for high ionic conductivity, followed with incorporated with electrospun polyacrylonitrile nanofibers (PAN-NFs) for better mechanical strength and flexibility. The well-fabricated polymer matrix may provide fast and effective Li^+ conductive pathways with a remarkable ionic conductivity at room temperature and a superior lithium-ion transference number close to unity. The introduction of PAN-NFs may also endow the plasticized SIPE with a wider electrochemical stability window and better cycling stability. Superior long-term lithium cycling stability and

dynamic interfacial compatibility may be demonstrated by lithium symmetric cell testing. The assembled all-solid-state Li metal batteries with LiFePO_4 may show stable cycling performance and remarkable rate capability both in low and high current densities.

2.2 $\text{Li}_{6.28}\text{La}_3\text{Zr}_2\text{Al}_{0.24}\text{O}_{12}$ -reinforced Single-ion Conducting Composite Polymer Electrolyte for Room-Temperature Li-Metal Batteries

Composite polymer electrolytes composed of inorganic fillers and organic polymers have been considered to be a very promising candidate for Li metal batteries with improved safety and suppressed lithium dendrite growth. However, severe concentration polarization effect is happened in using conventional dual-ion polymer matrix, which could bring in higher internal impedance within cells with decreased lifespan. To address this challenge, plasticized single-ion conducting composite polymer electrolyte (SICE) was designed and fabricated by polymerizing the monomers of lithium (4-styrenesulfonyl) (trifluoromethanesulfonyl) imide (LiSTFSI) and poly(ethylene glycol) methyl ether acrylate (PEGMEA), crosslinker poly(ethylene glycol) diacrylate (PEGDA), silane-modified $\text{Li}_{6.28}\text{La}_3\text{Al}_{0.24}\text{Zr}_2\text{O}_{12}$ nanofibers (s@LLAZO NFs), along with the PEG-based plasticizer tetraethylene glycol dimethyl ether (TEGDME) by heat-initiation. The restrained delocalized anions allow only Li cation migrate during charging/discharging process, leading to a superior lithium-ion transference number. The s@LLAZO NFs enabled direct monomer grafting with polymer matrix, resulting in a controlled formation of an organic-inorganic network that improved the filler content and distribution with enhanced interaction between filler and polymer in SICE system. The resultant electrolyte exhibited a high ionic conductivity under room temperature, reduced activation energy and excellent oxidation stability which are beneficial from the well-percolated amorphous region in

polymer system and extra Li ion conductive pathways in ceramic structure due to the added plasticizer and LLAZO NFs. Most importantly, all-solid-state Li-metal batteries assembled with the fabricated SICE demonstrated stable long-term cycling performance and remarkably rate capability at room temperature owing to the improved electrochemical stability with the utilization of fast Li⁺ conductors (LLAZO) in the composite structure. Therefore, this novel and straightforward single-ion conducting composite polymer electrolyte has great potential in the development of advanced all-solid-state Li-metal batteries.

2.3 Garnet-type Composite Polymer Electrolyte for Room-Temperature All-Solid-State Li-S Battery

In recent years, lithium-sulfur batteries are considered as one of the most promising rechargeable energy storage systems due to their extremely high theoretical specific capacity (1675 mAh g⁻¹) and large energy density (2567 Wh kg⁻¹), compared to the traditional lithium-ion batteries with limited theoretical capacity (~300 mAh g⁻¹) and energy density (~200 Wh kg⁻¹). Meanwhile, the element sulfur is low-cost, environmentally benign and abundant in earth's crust. However, the commercialization of Li-S batteries is hindered due to the relatively low attainable energy density, short cycling life and insufficient mass loading. The most severe reason is the generation of highly soluble long-chain polysulfides (Li₂S_n, 4 ≤ n ≤ 8), called “shuttle effect”, when using organic liquid electrolyte, causing irreversible loss of active sulfur materials and subsequently rapid capacity fading on cycling. Therefore, the investigation of suitable solid-state electrolytes for lithium-sulfur batteries is critical owing to the dual improvement on safety and cycling performance. It is reported that Li_{6.28}La₃Zr₂Al_{0.24}O₁₂ (LLAZO) exhibits great function on restraining polysulfides migration. An advanced CPE reinforced with nanofibrous LLAZO fillers

will be developed as solid electrolyte for all-solid-state Li-S batteries. The CPE precursor solution will be directly coated on the top of the sulfur cathode and then crosslinked into membrane with a thin thickness of around 20 μm . An improved interfacial contact between sulfur cathode and electrolyte may be obtained by this direct coating method. This coated CPE may enable a fast Li^+ conduction directly from the cathode to the anode, leading to a better cycling performance of all-solid-state Li-S batteries at room temperature.

CHAPTER 3: Polyacrylonitrile Nanofiber-Reinforced Flexible Single-Ion Conducting Polymer Electrolyte for High-Performance, Room-Temperature All-Solid-State Li-Metal Batteries

Abstract

Single-ion conducting polymer electrolytes (SIPes) can be formed by anchoring charge delocalized anions on side chains of a crosslinked polymer matrix, thereby eliminating the severe concentration polarization effect in conventional dual-ion polymer electrolytes. Addition of a plasticizer into the polymer matrix confers advantages of both liquid and solid electrolytes. However, plasticized SIPes usually face a trade-off between conductivity and mechanical strength. With insufficient strength, there is potential for short-circuiting failure during cycling. To address this challenge, a simple and mechanically-robust SIPE was developed by crosslinking monomer lithium (4-styrenesulfonyl) (trifluoromethylsulfonyl) imide (LiSTFSI) and crosslinker poly(ethylene glycol) diacrylate (PEGDA), with plasticizer propylene carbonate (PC), on electrospun polyacrylonitrile nanofibers (PAN-NFs). The well-fabricated polymer matrix provided fast and effective Li^+ conductive pathways with a remarkable ionic conductivity of $8.09 \times 10^{-4} \text{ S cm}^{-1}$ and a superior lithium-ion transference number close to unity ($t_{\text{Li}^+} = 0.92$). The introduction of PAN-NFs not only improved the mechanical strength and flexibility but also endowed the plasticized SIPE with a wide electrochemical stability window (4.9 V vs. Li^+/Li) and better cycling stability. Superior long-term lithium cycling stability and dynamic interfacial compatibility were demonstrated by lithium symmetric cell testing. Most importantly, the assembled all-solid-state Li metal batteries showed stable cycling performance and remarkable rate capability both in low and high current densities. Therefore, this straightforward and

mechanically reinforced SIPE exhibits great potential in the development of advanced all-solid-state Li-metal batteries.

3.1 Introduction

Rechargeable lithium-ion batteries (LIBs) were first introduced into the commercial market by Sony in the early 1990s and are considered the most significant achievement in the development of electrochemical energy storage technologies due to their high specific energy, high operating voltage, and long cycle life. [1-3] However, with rapidly growing demands for portable electronic devices, electric vehicles and grid-energy storage systems, current LIBs are insufficient to fulfill future requirements due to their limited power density, high cost, and poor safety. [8-10] Thus, extensive research has shifted to lithium metal, which is regarded as the “holy grail” for next-generation energy storage systems due to its high theoretical specific capacity (3860 mA h g^{-1}), low density (0.59 g cm^{-3}), and low redox potential (-3.04 V vs. standard hydrogen electrode). [4, 12, 13] Commercial LIBs usually utilize lithium salts dissolved in carbonate-based organic solvents as liquid electrolytes for lithium-ion transportation. [15] However, with use of liquid electrolytes in lithium metal batteries (LMBs), growth of dendrites from the lithium metal anode during repeated Li plating/stripping can cause great safety concerns like short circuits and thermal runaway, resulting in catastrophic battery failure. Even if dendritic growth is avoided, liquid electrolytes in LMBs can generate an unstable solid electrolyte interface (SEI) upon cycling, leading to decreasing Coulombic efficiency and irreversible capacity loss. [4] In addition, decomposition of lithium salts and side reactions between electrolyte and anode bring steady capacity fade during charge-discharge cycling, limiting long-term durability of these batteries. [9, 15]

Single-ion conducting polymer electrolytes (SIPs), which can be fabricated by anchoring charge delocalized anions as side chains on the polymeric backbone of a electrolyte system, can avoid the abovementioned problems of dendritic growth and SEI instability in LMBs, resulting

in improved safety, good processability, superior flexibility and enhanced mechanical compliance with the electrodes. [4, 7] In previous work, conventional polymer electrolytes (PEs) employing lithium salts like LiTFSI, LiPF₆, LiClO₄, LiBF₄ and LiCF₃SO₃, are usually dual-ion conductors, in which both Li⁺ cations and their counter anions migrate during the charging/discharging process. [23-28] Thus, the lithium-ion transference number for a binary salt electrolyte is simply defined as the fraction of the ionic conductivity that is carried by lithium ions compared with the total ionic conductivity carried by lithium ions and their counter ions, and can be calculated by:

$$t_{\text{Li}^+} = D^+ / (D^- + D^+) \quad (3.1)$$

where t_{Li^+} is lithium-ion transference number, D^+ is the lithium-ion diffusion coefficient, and D^- is the anion diffusion coefficient. [29] It is obvious that t_{Li^+} is highly related to the diffusion of lithium ions and counter anions. However, the overall conductivity of binary PEs is predominated by the motion of counter anions that have greater mobility than lithium cations. This happens due to the strong preferential solvation of lithium ions over their counter anions, leading to a bulkier solvation shell around lithium ions compared to typical counter anions. [34] Therefore, lithium-ion transference numbers of binary PE systems are undesirably low, always lower than 0.5, typically ranging from 0.1 to 0.4 in real applications. [35, 36] As a result, a severe concentration polarization effect is generated because anions migrate in the opposite direction of the lithium ions and eventually accumulate at the electrode surface, which brings higher internal impedance, decreased energy density and lower charging rate. [1, 37] Moreover, according to Chazalviel's space-charge theory in 1990, an electric field could be induced near the Li anode region due to concentration polarization, which will cause uneven distribution of lithium-ion flux and lead to growth of lithium dendrites. [38, 39]

In contrast, SIPEs with immobilized anions along polymer backbone can maintain high lithium-ion transference numbers, which is desirable for advanced lithium metal batteries. It has been demonstrated by Monroe and Newman's simulations in 1994 that no concentration gradients occurred in PE systems with a unity t_{Li^+} , in which the utilization of active electrode materials remains near 100%, even at relatively high current densities, further improving the energy and peak-power densities for these batteries. [1, 30] However, immobilizing the anions typically results in significantly decreased ionic conductivity of the SIPE system, owing to the strong ion pairing between Li ions and anions. [7, 30] It is reported that the highest bulk ionic conductivity of dry SIPEs is approximately $10^{-5} \text{ S cm}^{-1}$ at $60 \text{ }^\circ\text{C}$, which is nearly three orders of magnitude lower than that of a standard liquid electrolyte at room temperature. [31-33] Thus, cyclic carbonates with high dielectric constant and flash point are often introduced into the polymer system, thereby integrating the advantages of both liquid and solid electrolytes. [65] Compared to dry SIPEs, these plasticized SIPEs can provide high ionic conductivity up to $10^{-3} \text{ S cm}^{-1}$ via enhanced polymer chain segmental motion and increased ion pair dissociation under room temperature. [1, 66, 67] Furthermore, the crosslinked networks with added plasticizer facilitate a relatively homogeneous Li^+ ion flux, minimizing volumetric changes of Li deposition and blocking lithium dendrite growth. [68] However, plasticized SIPEs possess a trade-off between improved conductivity and compromised mechanical strength. A lack of strength could induce short-circuiting failure during cycling. [4, 46] To improve the strength of the electrolyte, reinforcement agents, such as inorganic ceramic fillers, organic metal frames and free-standing membranes, can be introduced into the crosslinked system to improve the mechanical properties of plasticized SIPEs. [4, 8, 9, 69, 199]

In this paper, a flexible and free-standing membrane of electrospun polyacrylonitrile nanofibers (PAN-NFs), with robust mechanical strength and good electrochemical stability, [153, 200-202] was introduced to reinforce the plasticized SIPE. The reinforcement was realized by polymerizing the monomer lithium (4-styrenesulfonyl) (trifluoromethanesulfonyl) imide (LiSTFSI) and crosslinker poly(ethylene glycol) diacrylate (PEGDA), along with the plasticizer propylene carbonate (PC), by UV-initiation on the PAN-NFs membrane. The crosslinked polymer network with additional plasticizer on the PAN-NF membrane exhibited outstanding ionic conductivity, excellent mechanical properties, wide electrochemical stability window and remarkable cycling stability. Moreover, the covalently-bonded lithium salt anions on the polymer chain yielded a near unity lithium-ion transference number. Lithium symmetric cells assembled with the plasticized SIPE on PAN-NFs showed superior long-term lithium cycling stability and interfacial compatibility. Most importantly, all-solid-state Li|LFP cells with the plasticized SIPE on PAN-NFs showed stable cycling performance and remarkable rate capability with high Coulombic efficiency.

3.2 Experimental Section

3.2.1 Materials

Oxalyl chloride ((CO)₂Cl₂), N,N-dimethylformamide (DMF), acetonitrile (CH₃CN), sodium 4-vinylbenzenesulfonate, triethylamine (TEA), 4-dimethylamino pyridine (DMAP), dichloromethane (DCM), sodium bicarbonate (NaHCO₃), hydrochloric acid (HCl), potassium carbonate (K₂CO₃), lithium perchlorate (LiClO₄), tetraethylene glycol dimethyl ether (G₄), 1-hydroxycyclohexyl phenyl ketone (HPK), 1-methyl-2-pyrrolidinone (NMP), bis(trifluoromethane)sulfonimide lithium salts (LiTFSI), poly(ethylene glycol) diacrylate

(PEGDA, $M_w=700$), dimethyl sulfoxide- d_6 (DMSO- d_6), polyacrylonitrile (PAN, $M_w=150,000$), propylene carbonate (PC), and N-methyl-2-pyrrolidone (NMP) were purchased from Sigma-Aldrich. Trifluoromethanesulfonamide was purchased from Oakwood Chemical. Acetonitrile and DMF were dried and stored with 4A molecule sieves before use. Other chemicals were used as received without further purification.

3.2.2 Synthesis of monomer lithium (4-styrenesulfonyl) (trifluoromethylsulfonyl) imide

As shown in **Figure 3.1**, the lithium (4-styrenesulfonyl) (trifluoromethylsulfonyl) imide (LiSTFSI) monomer was synthesized in the two-step method as described in the literature. [49, 55] The monomer of potassium (4-styrenesulfonyl) (trifluoromethylsulfonyl) imide (KSTFSI) was synthesized in the first step and then followed with a metathesis reaction between KSTFSI and lithium ion to obtain LiSTFSI monomer.

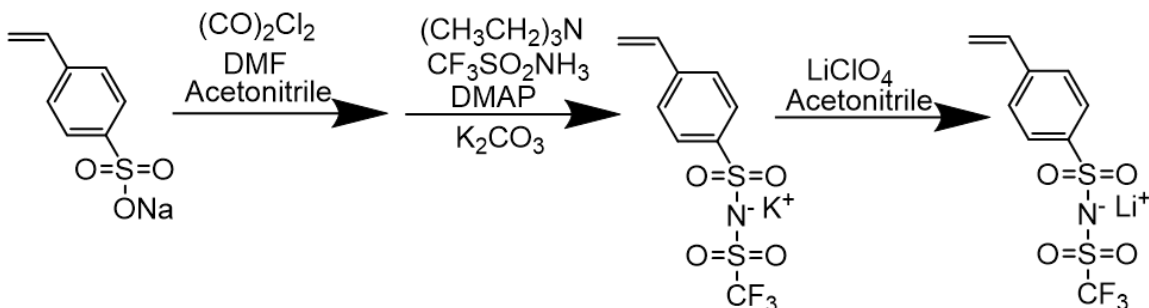


Figure 3.1. Schematic illustration of the chemical synthetic process of LiSTFSI.

During the synthesis of KSTFSI, $(CO)_2Cl_2$ (46.6 mmol, 4 ml) and DMF (2 mmol, 190 μ l) were well-dissolved in 80 ml dried acetonitrile and stirred at room temperature for 5 hours. Then, 4-vinylbenzenesulfonate (38.8 mmol, 8 g) was added into the solution under argon atmosphere when the color turned light yellow. The mixture was stirred for 24 hours inside the laboratory hood at room temperature. A separate colorless solution was formed by gradually mixing TEA

(116.2 mmol, 16.2 ml), DMAP (48.1 mmol, 5.4 g) and trifluoromethanesulfonamide (38.8 mmol, 5.78 g) in 60 ml dried acetonitrile and stirring for 1 hour at room temperature. Subsequently, a clear light-brown 4-styrene sulfonyl chloride solution was obtained after the precipitate NaCl was filtered from the mixture. The colorless solution was dropwise added into 4-styrene sulfonyl chloride solution under an ice bath with vigorous magnetic stirring. The ice bath was removed when the mixed solution cooled down. The solution turned brown and was vigorously stirred for 16 hours inside the laboratory hood at room temperature. The solvent was removed by rotary evaporation and the resulting brown solid was dissolved in 100 ml DCM. The following solution was washed by 40 ml 4% NaHCO₃ aqueous solution three times and 40 ml 37% HCl aqueous solution. The intermediate product of potassium (4-styrenesulfonyl) (trifluoromethylsulfonyl) imide (KSTFSI) was synthesized by neutralization of the acid monomer with excess 0.5 mol/L K₂CO₃ aqueous solution. The obtained white suspension was stirred at room temperature for 1 hour and filtered to get a slightly yellow solid. The resulting solid, KSTFSI, was dried under high vacuum at 60°C overnight (30% yield).

The synthesis of KSTFSI was confirmed by ¹H NMR and ¹³C NMR (**Figure 3.2**). ¹H NMR (600 MHz; DMSO-d₆; ppm): 7.7705 (d, 2H); 7.6296 (d, 2H); 6.8393 (q, 1H); 6.0254 (d, 1H); 5.4370 (d, 1H); ¹³C NMR (600 MHz; DMSO-d₆; ppm): 144.7104; 140.1258; 136.1100; 126.9751; 126.4349; 117.1459.

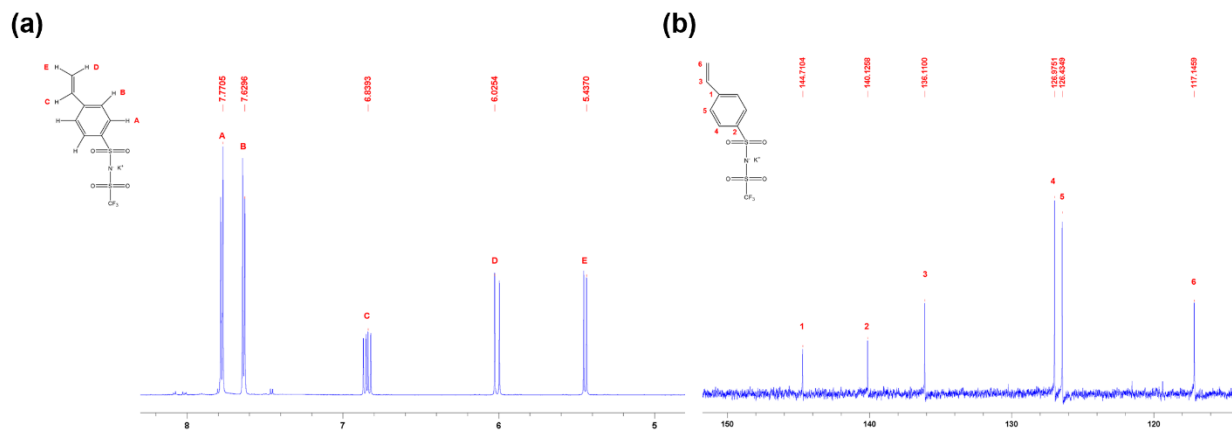


Figure 3.2. (a) ^1H NMR and (b) ^{13}C NMR spectra of KSTFSI.

After the synthesis and confirmation of KSTFSI, LiSTFSI was synthesized by a metathesis reaction between KSTFSI and LiClO_4 . KSTFSI powder (8.5 mmol, 3 g) was added in 100 ml dried acetonitrile under argon atmosphere and stirred until the powder was completely dissolved. LiClO_4 (8.5 mmol, 0.91 g) was well-dissolved in 20 ml dried acetonitrile and added into KSTFSI solution by needled syringe. The resulting solution was stirred under argon atmosphere at room temperature overnight. The white KClO_4 precipitate was filtered and the solvent was removed via rotary evaporator. The obtained white solid was recrystallized from deionized water and then dried under high vacuum at 60°C to get pure white LiSTFSI powder (37% yield). The final product LiSTFSI was stored in a glovebox (H_2O , $\text{O}_2 < 0.5$ ppm) for further use.

The obtained LiSTFSI was confirmed by ^1H NMR, ^{13}C NMR, and ^{19}F NMR (**Figure 3.3**). ^1H NMR (600 MHz; DMSO-d_6 ; ppm): 7.7845 (d, 2H); 7.6435 (d, 2H); 6.8505 (q, 1H); 6.0263 (d, 1H); 5.4553 (d, 1H); ^{13}C NMR (600 MHz; DMSO-d_6 ; ppm): 146.1972; 141.6377; 137.6047; 128.4788; 127.9381; 118.6575; ^{19}F NMR (600 MHz; DMSO-d_6 ; ppm): 77.8133 (s, 3F).

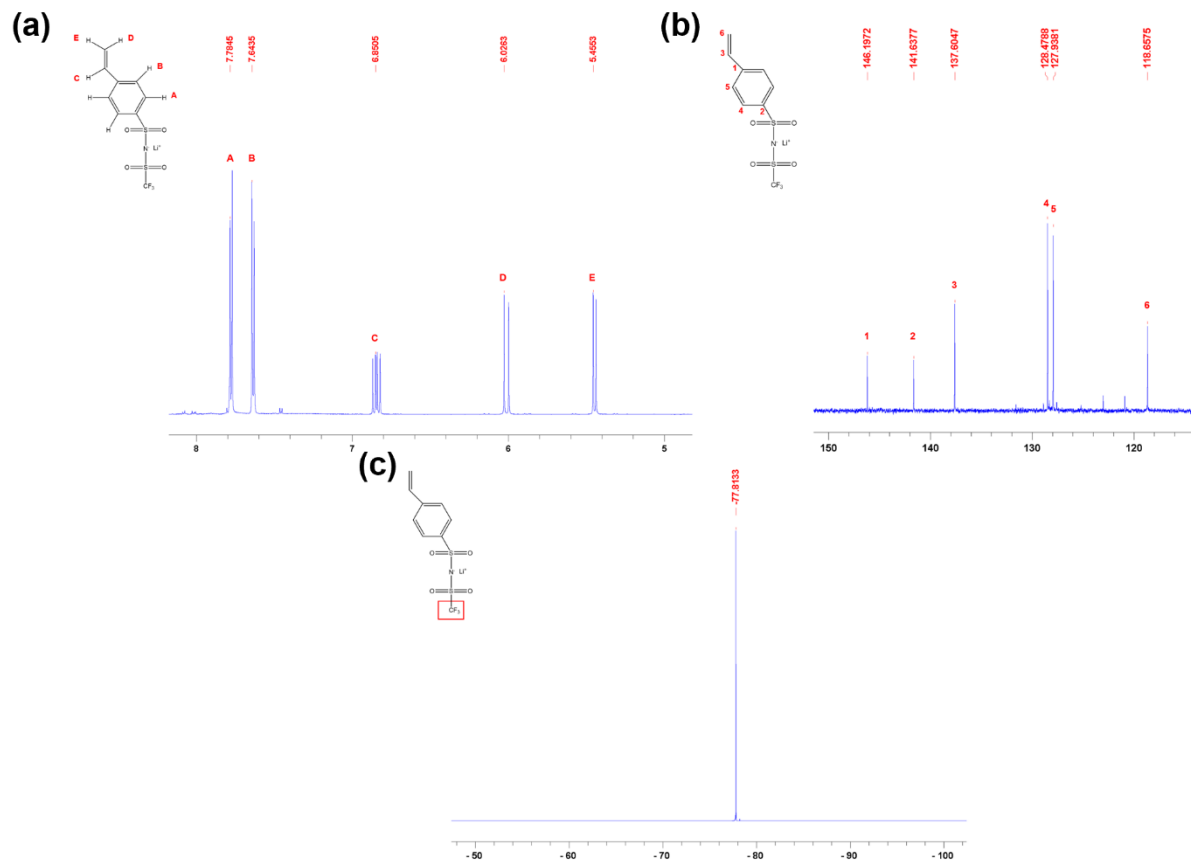


Figure 3.3. (a) ^1H NMR, (b) ^{13}C NMR, and (c) ^{19}F NMR spectra of LiSTFSI.

3.2.3 Preparation of single-ion conducting polymer electrolytes

The SIPEs were simply prepared by one-pot free radical polymerization employing HPK as the UV initiator in a glovebox. PEGDA and LiSTFSI solutions according to different molar ratios of [EO] with $[\text{Li}^+]$ were designed as the crosslinking polymer system for SIPE fabrication. Herein, LiSTFSI and PEGDA solutions containing 0.2 wt.% HPK were mixed, and different amount of organic solvent PC as plasticizer was added into the solutions in a glovebox. The resultant precursor solutions were sonicated for 1 hour and then cross-linked into thin films between two transparent quartz plates by exposing to UV light for 10 mins. The polymerized SIPE

membranes with plasticizer were denoted as SIPE-x, where x represented the weight ratio of PC to PEGDA and LiTFSI.

The SIPE-x reinforced with PAN-NFs was fabricated via applying precursor solution on PAN-NF membrane before UV-initiated polymerization, and was described as SIPE-x-PAN. PAN nanofiber membrane with a thickness around 20 μm was simply produced by electrospinning 8 wt.% PAN/DMF solution at a high voltage of 15 kV with a feeding rate of 0.75 ml h⁻¹. The distance between the stainless-steel needle and aluminum collector was fixed at 15 cm. The electrospun PAN-NF membrane was dried under high vacuum at 60°C overnight. The reinforcement of PAN-NFs would facilitate the mechanical strength of the SIPEs for better electrochemical and cycling performance in LMBs.

3.2.4 Structure characterization

¹H NMR, ¹³C NMR, and ¹⁹F NMR spectra analyses were conducted on Bruker NEO 600 MHz Polk NMR spectrometer with DMSO-d₆ as the solvent. Fourier transform-infrared spectroscopy (FTIR, Thermo Scientific™ Nicolet™ iS™10) was used to identify the functional groups of LiTFSI powder, PEGDA solution and LiTFSI-PEGDA (dry SIPE, [EO]/[Li⁺]=24) membrane at the range of 4000~500 cm⁻¹ with 32 scans and resolution of 4 cm⁻¹ at room temperature.

Dynamic mechanical analyzer (DMA Q800, TA Instruments) was employed to evaluate the viscoelastic properties of dry SIPE and SIPE-x (x=0.5, 1, 2, 2.5, the weight ratio of PC to LiTFSI and PEGDA) membranes from -100°C to 50°C. A universal mechanical test machine (MTS Criterion, Loading: 100 N) was also utilized to measure the mechanical properties of PAN-NF, SIPE-2.5 and SIPE-2.5-PAN membranes with a cross-head speed of 0.5 mm/min.

Thermo-gravimetric analysis (TGA, Perkin Elmer Pyris 1) was used with a heating rate of 10 °C

min⁻¹ under nitrogen atmosphere to test the thermal property of PAN-NF, dry SIPE and SIPE-2.5-PAN membranes. Field-emission scanning electron microscopy (FE-SEM, FEI Verios 460L, USA) was conducted to characterize the surface morphology of PAN-NF membrane and cross-section thickness of SIPE-2.5-PAN membrane. ImageJ Software was used to measure the average diameter of PAN NFs.

3.2.5 Electrochemical performance evaluation

Ionic conductivities of all SIPEs were determined by electrochemical impedance spectroscopy (EIS, Garmy Reference 600 device) over a frequency range of 0.1 Hz to 1 MHz with an AC potential of 10 mV. Polymer electrolyte membranes were pouched and sandwiched between two stainless steel blocking electrodes for electrochemical impedance test. The ionic conductivity (δ , S cm⁻¹) was calculated by the following equation:

$$\delta = t/R_bA \quad (3.2)$$

where t is the thickness of polymer electrolyte membrane, R_b the membrane bulk resistance obtained from the intercept of extended semicircle with the real axis on the Nyquist plot, and A the area of the membrane. Activation energy (E_a , eV) of SIPEs was calculated with an Arrhenius plot of ionic conductivities under different temperatures by the Arrhenius equation:

$$\delta = A\exp(-E_a/RT) \quad (3.3)$$

where δ is the ionic conductivity, A the dc conductivity of pre-exponential factor, E_a the activation energy, R the molar gas constant, and T the absolute temperature.

Lithium-ion transference number (t_{Li^+}) of each SIPE membrane was determined by chronoamperometry testing and electrochemical impedance spectroscopy (EIS) measurement at 60°C. A symmetric lithium cell was assembled and tested by EIS with a frequency ranging from

0.1 Hz to 1 MHz before and after polarization. Chronoamperometry was performed with an applied DC potential of 10 mV. The t_{Li^+} value was calculated by Bruce's equation:

$$t_{\text{Li}^+} = I_{\text{SS}} (\Delta V - I_0 R_{i,0}) / I_0 (\Delta V - I_{\text{SS}} R_{i,\text{SS}}) \quad (3.4)$$

where ΔV is the polarization potential, I_0 and I_{SS} the initial and steady-state currents before and after polarization, R_0 and R_{SS} the initial and steady-state total resistances before and after polarization.

Linear sweep voltammetry (LSV) was conducted to assess the electrochemical stability of SIPE-2.5 and SIPE-2.5-PAN using Li|SIPE|stainless steel cells with a scan rate of 10 mV s^{-1} over a voltage range of 0-6 V (vs. Li^+/Li). Cyclic voltammetry (CV) was also carried out on Li|SIPE|stainless steel cells at a scan rate of 0.5 mV s^{-1} from -0.5 to 5.5 V (vs. Li^+/Li) at room temperature. Galvanostatic cycling testing of Li|SIPE-2.5|Li and Li|SIPE-2.5-PAN|Li symmetric cells was conducted at room temperature to evaluate the structural stability of SIPE-2.5 and SIPE-2.5-PAN. Li plating/stripping cycling performance was evaluated by sandwiching a SIPE-2.5-PAN membrane (80-100 μm thickness and 1/2 inch diameter) between two Li foils (7/16 inch diameter) and cycling at current densities of 0.1, 0.2, 0.5, 1 mA cm^{-2} with current direction reversed every 30 minutes.

All-solid-state Li|LiFePO₄ (LFP) cells were fabricated for evaluating the performance of SIPE-2.5 and SIPE-2.5-PAN membranes in room-temperature all-solid-state batteries. The LFP cathode was prepared by mixing a slurry of LFP, ionic liquid solution of G4 with LiTFSI in equimolar amounts, carbon black (C65), and polyvinylidene fluoride (PVDF) binder at a weight ratio of 7:2:0.5:0.5 in NMP solvent, which was uniformly coated on aluminum foil by a doctor blade set at 10 mm. The prepared cathode was dried under high vacuum at 60 °C overnight to remove NMP solvent. The LFP cathode was then punched into disks with a diameter of 7/16

inches with an active material loading around 1.5-2.0 mg cm⁻². Standard LIR2032 coin cells were assembled in a glovebox by sandwiching SIPE-2.5 and SIPE-2.5-PAN membrane disks of 1/2 inch diameter between pre-punched LFP cathode and Li foil. The cycling performance of all-solid-state Li|LFP cells was then tested by an Arbin battery tester in a potential range of 2.5 V to 4.2 V.

3.3 Results and Discussion

3.3.1 Design of plasticized single-ion conducting polymer electrolytes reinforced with PAN-NFs

Although plasticized SIPEs possess excellent ionic conductivity and superior lithium-ion transference number, they suffer from poor mechanical strength, which could potentially lead to short-circuiting failure during prolonged cycling of LMBs. To address this challenge, a simple and mechanically-robust plasticized SIPE was developed by crosslinking monomer LiSTFSI and PEGDA, with plasticizer PC, on a free-standing, mechanically strong electrospun PAN-NF membrane, to achieve a well-designed balance between electrochemical properties and mechanical strength for developing high-performance LMBs (**Figure 3.4**).

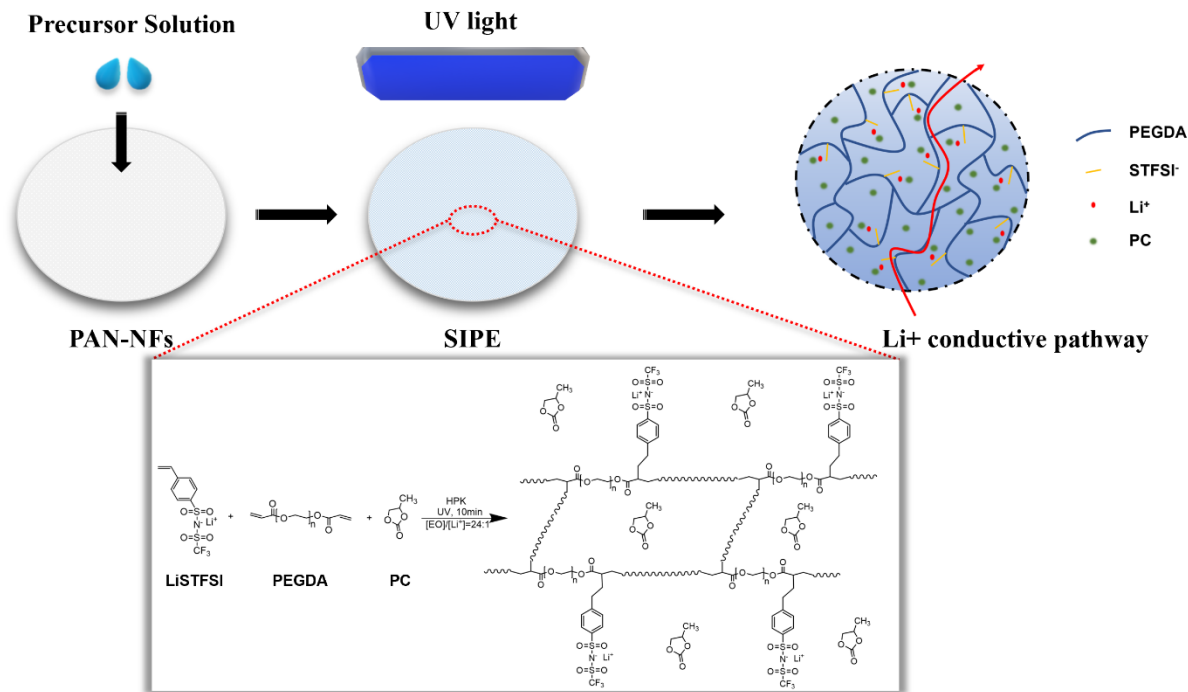


Figure 3.4. Schematic of synthesis procedure of plasticized SIPE membrane reinforced with PAN-NFs, with a crosslinked amorphous network within the polymer electrolyte, providing fast Li⁺ conductive pathways.

It is well-known that the repeat unit of -CH₂-CH₂-O- (EO) in a polyethylene oxide-based polymer is responsible for lithium-ion complexation and transportation. [7] In this work, UV-initiated crosslinked polymer electrolyte series synthesized from monomer LiSTFSI and crosslinker PEGDA were firstly investigated with [EO]/[Li⁺] molar ratio from 8 to 32. Electrochemical impedance spectroscopy (EIS) was applied for measuring the ionic conductivities of the crosslinked polymer electrolytes. The obtained results shown in **Figure 3.5a** indicate that the crosslinked polymer electrolytes with [EO]/[Li⁺] molar ratio of 24 showed the highest ionic conductivity of $7.2 \times 10^{-6} \text{ S cm}^{-1}$ at room temperature, which represents saturation of the Li⁺ in the polymer system. [203] When the [EO]/[Li⁺] molar ratio is lower than 24, the low ionic conductivities could be attributed to ion aggregation effects, which would decrease the

effective number of charge carriers for the crosslinked system. [204] When the $[\text{EO}]/[\text{Li}^+]$ molar ratio is greater than 24, the conductivity declined due to the insufficient quantity of Li^+ charge carriers for ion transportation. The successful polymerization between LiSTFSI and PEGDA was then confirmed by FTIR spectra (**Figure 3.5b**), where the absorption bands due to the stretching vibration of $=\text{C}-\text{H}$ at $3105, 3104 \text{ cm}^{-1}$; and $\text{C}=\text{C}$ at $1632, 1635 \text{ cm}^{-1}$ from LiSTFSI and PEGDA all disappeared in the crosslinked polymer electrolyte ($[\text{EO}]/[\text{Li}^+] = 24$). This indicated that both vinyl groups from LiSTFSI monomer and PEGDA crosslinker have reacted completely during UV-initiated polymerization. Since the crosslinked polymer electrolyte ($[\text{EO}]/[\text{Li}^+] = 24$) has the highest ionic conductivity among all electrolytes studied so far that did not have plasticizer, it was used as the base electrolyte in the studies below and was denoted as dry SIPE.

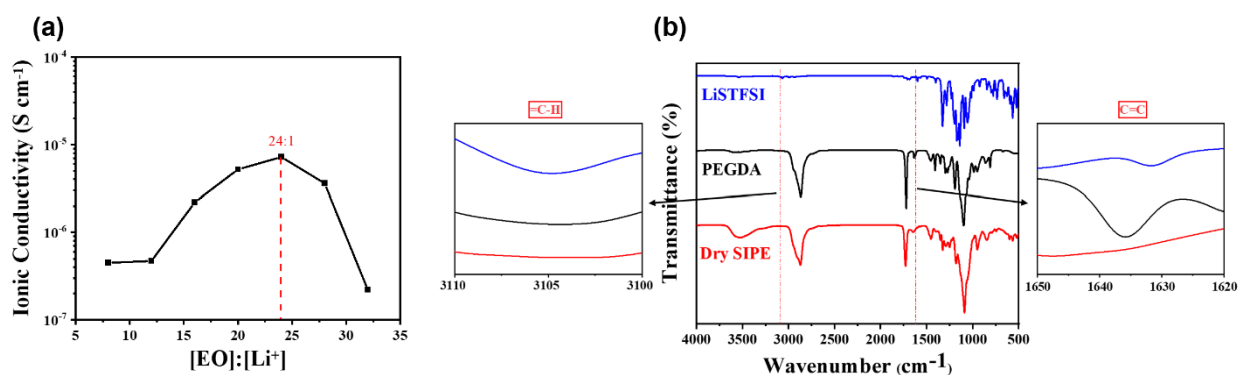


Figure 3.5. (a) Ionic conductivity versus molar ratio of $[\text{EO}]/[\text{Li}^+]$ for the crosslinked solid polymer electrolyte series at room temperature; (b) FTIR spectra of LiSTFSI, PEGDA and dry SIPE ($[\text{EO}]/[\text{Li}^+]=24$).

Plasticizers can enhance polymer segmental motion, increase ion pair dissociation, and provide different cationic species transport mechanisms by facilitating vehicular transport of the solvated cation with reduced polymer segmental dynamics of ether oxygen–cation interaction. [66] In this work, PC was added as a plasticizer to the dry SIPE, and the resultant plasticized SIPEs were

denoted as SIPE-x, where x represented the weight ratio of PC to dry SIPE (i.e., PEGDA and LiSTFSI). Ionic conductivities at room temperature were calculated using the intercept of extended semicircles measured by EIS (**Figure 3.6a**). As shown in **Figure 3.6a**, the ionic conductivity of SIPEs increased with addition of PC, and SIPE-2.5 exhibited the highest ionic conductivity of $1.18 \times 10^{-3} \text{ S cm}^{-1}$, two orders of magnitude higher than that of dry SIPE.

It has been demonstrated the SIPE-2.5 membrane has sufficient ionic conductivity for use as solid electrolyte in LMBs. However, high mechanical strength is also required to control the growth of Li dendrites in all-solid-state LMBs. [8] As shown in **Figure 3.6b**, the addition of PC plasticizer dramatically decreased the Young's modulus of SIPE membranes due to reduced intramolecular forces between the polymer chains, [205] resulting in the plasticized SIPE-2.5 membrane not sufficiently mechanically strong for use with advanced LMBs.

To improve the mechanical properties of SIPE-2.5, an electrospun PAN-NFs membrane was used as the structural support. In an Ar-filled glovebox, a precursor solution with PC was added into the well-prepared PAN-NFs membrane with a mass ratio around 12:1, followed by exposure to UV radiation to initiate free radical polymerization. This process yielded a modified SIPE membrane composed of a well-controlled polymer system, i.e., PC-plasticized LiSTFSI-PEGDA polymer electrolyte reinforced with PAN-NFs, which was denoted as SIPE-2.5-PAN. The final mass ratio of the UV crosslinked polymer with respect to PAN nanofibers is around 18:1. **Figure 3.6c** shows the strain-stress curves of electrospun PAN-NFs, SIPE-2.5 and SIPE-2.5-PAN, with the corresponding information summarized in **Table 3.1**. The original SIPE-2.5 membrane showed a Young's modulus of 0.76 MPa, tensile strength of 0.03 MPa, and maximum elongation of 2.6%. After reinforcing with PAN-NFs, the transformed SIPE-2.5-PAN membrane acquired an enhanced Young's modulus of 5.91 MPa. In addition, the tensile strength and

maximum elongation increased remarkably to 4.45 MPa and 152%, respectively, showing the robust mechanical improvement with the introduction of PAN-NFs to the plasticized SIPE.

Thermo-gravimetric analysis (TGA) under nitrogen atmosphere was then conducted for thermal property testing. As shown in **Figure 3.6d**, the weight loss before 160 °C can be ascribed mainly to PC volatilization, as only 10% weight loss was observed at 100 °C. Additionally, PAN-NFs and polymer matrix started to lose weight from 300 °C and 350 °C, respectively, indicating that SIPE-2.5-PAN had the ability to maintain sufficient thermal stability under normal working temperatures of LMBs.

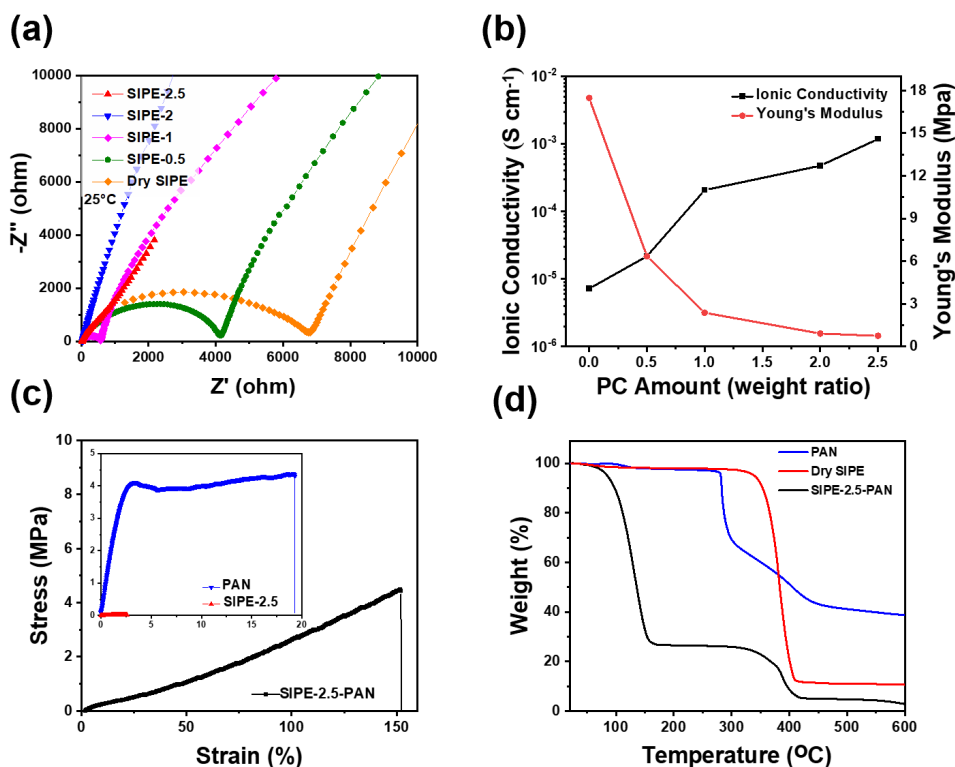


Figure 3.6. (a) EIS profiles of dry SIPE and SIPE-x at room temperature; (b) Ionic conductivity and Young's modulus versus PC weight ratio for dry SIPE and SIPE-x; (c) Stress-strain curves of PAN-NFs, SIPE-2.5 and SIPE-2.5-PAN; and (d) TGA curves of PAN-NFs, dry SIPE and SIPE-2.5-PAN from 20 to 600 °C.

Table 3.1. Mechanical properties of PAN-NFs, SIPE-2.5 and SIPE-2.5-PAN.

Samples	Young's Modulus (MPa)	Tensile Strength (MPa)	Elongation (%)
PAN-NFs	197	4.37	19.3
SIPE-2.5	0.76	0.03	2.60
SIPE-2.5-PAN	5.91	4.45	152

The surface morphologies of electrospun PAN-NFs and SIPE-2.5-PAN membrane were characterized by field-emission scanning electron microscopy (FE-SEM). It can be observed in **Figure 3.7a-b** that uniform PAN nanofibers with an average diameter of 300 nm were well-fabricated by electrospinning, and the interspace in the 3D-network structure of electrospun PAN-NFs was fully covered by plasticized SIPE. The average diameter of PAN-NFs in plasticized SIPE increased to 550 nm as a result of PC absorption during the polymerization process, which indicated that the employment of PAN-NFs not only improved the mechanical properties, but also helped to enroll organic solvent in the SIPE system. As a result, SIPE-2.5-PAN membrane maintained a robust mechanical strength due to the support from the 3D-network structure of electrospun PAN-NFs. Moreover, the obtained SIPE-2.5-PAN membrane was easily punched into discs with a thickness of just 82 μm (**Figure 3.7c-d**), which could be bent, twisted, and rolled up without breakage or cracking (**Figure 3.8**). Therefore, in addition to improved mechanical strength, SIPE-2.5-PAN membrane also possessed excellent mechanical flexibility for use in advanced LMBs.

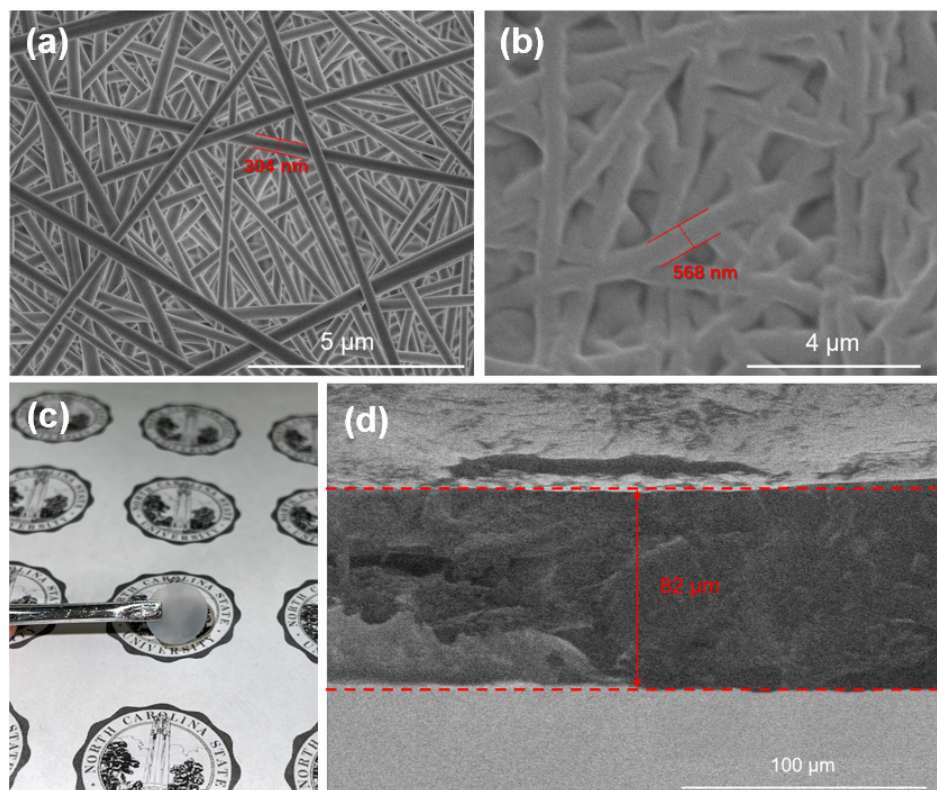


Figure 3.7. SEM images of top view of (a) PAN-NFs and (b) SIPE-2.5-PAN; (c) Digital image of SIPE-2.5-PAN; and (d) SEM image of the cross-section of SIPE-2.5-PAN.



Figure 3.8. (a-g) Digital images of bending test for SIPE-2.5-PAN membrane.

3.3.2 Electrochemical performance of plasticized single-ion conducting polymer electrolytes reinforced with PAN-NFs

The electrochemical performance of the plasticized SIPEs was investigated in **Figure 3.9** and summarized in **Table 3.2**. Ionic conductivities were tested under different temperatures, illustrated by Arrhenius plots in **Figure 3.9a**. All ionic conductivity-temperature curves obeyed the classical Arrhenius linear relationship within the testing temperature range (25~80 °C). The calculated activation energies of plasticized SIPEs declined from 0.75 to 0.18 eV with increasing amount of plasticizer, indicating a decreasing energy barrier in transporting solvated lithium cations within the polymer electrolyte system. The ionic conductivity and activation energy of SIPE-2.5-PAN membrane at room temperature were $8.09 \times 10^{-4} \text{ S cm}^{-1}$ and 0.19 eV, respectively, which were both close to those of the SIPE-2.5 membrane without PAN-NFs

(**Figure 3.10a** and **Table 3.2**). The strong polar and electron withdrawing cyan groups ($C\equiv N$) of PAN-NFs would be expected to facilitate the Li^+ ion transportation in the polymer matrix. [7, 202] The slight decrease in conductivity seen for SIPE-2.5-PAN is probably due to the tortuosity of conduction pathways with the addition of PAN-NFs compared to pristine SIPE-2.5. Lithium-ion transference number (t_{Li^+}) is an important parameter to evaluate the electrochemical performance of SIPEs. As a result of covalently bonded anions to the polymer chain, SIPEs usually possess a superior t_{Li^+} , close to unity, compared with dual-ion PEs. High t_{Li^+} values help to eliminate the concentration polarization effect and protect the lithium metal anode from dendrite formation, thereby improving the battery performance of all-solid-state LMBs. The t_{Li^+} value can be determined by Bruce's equation, combining results of chronoamperometry and electrochemical impedance spectroscopy (EIS) testing at 60 °C. [206] In this work, the t_{Li^+} values of SIPE-2.5 and SIPE-2.5-PAN were measured to be 0.93 (**Figure 3.10b**) and 0.92 (**Figure 3.9b**), respectively, indicating excellent single lithium-ion conducting behavior due to the immobilized 4-styrenesulfonyl (trifluoromethylsulfonyl) imide (STFSI⁻) anions along the polymer chain (**Figure 3.4**).

Figure 3.9c illustrates the linear sweep voltammetry (LSV) curves of SIPE-2.5 and SIPE-2.5-PAN membranes tested by sandwiching the electrolyte discs between lithium metal and stainless steel. Since an exponential increase in current density illustrates the onset of the degradation of the SIPE membrane, [207, 208] SIPE-2.5 exhibited excellent anodic stability with no obvious anodic current change until the potential reached 4.2 V vs. Li^+/Li , demonstrating the absence of electrochemically oxidized decomposition of the electrolyte. [61, 182] Compared with SIPE-2.5, the SIPE-2.5-PAN was even more electrochemically stable (4.9 V vs. Li^+/Li) due to the superior

electrochemical stability of embedded PAN-NFs. [7] In addition, as shown in **Figure 3.11a**, a wide stability window was observed for SIPE-2.5-PAN, which is favorable for advanced LIBs.

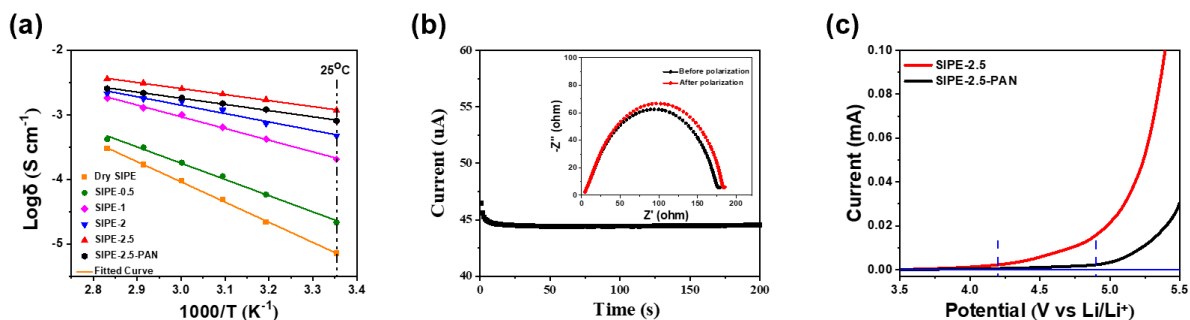


Figure 3.9. (a) Arrhenius plots of dry SIPE, SIPE-x and SIPE-2.5-PAN membranes; (b) Time-dependent response of DC polarization for Li|SIPE-2.5-PAN|Li symmetric cell (inset is the EIS plots before and after polarization); and (c) Linear sweep voltammetry curves of SIPE-2.5 and SIPE-2.5-PAN.

Table 3.2. Electrochemical properties of dry SIPE, SIPE-x and SIPE-2.5-PAN membranes.

Sample	Ionic Conductivity (S cm ⁻¹ , 25°C)	Activation Energy (eV)	t _{Li+}	T _g (°C)
Dry SIPE	7.20 × 10 ⁻⁶	0.748	0.74	0
SIPE-0.5	2.17 × 10 ⁻⁵	0.512	0.76	-39
SIPE-1	2.07 × 10 ⁻⁴	0.367	0.76	-59
SIPE-2	4.75 × 10 ⁻⁴	0.258	0.84	-77
SIPE-2.5	1.18 × 10 ⁻³	0.185	0.93	-93
SIPE-2.5- PAN	8.09 × 10 ⁻⁴	0.190	0.92	-90

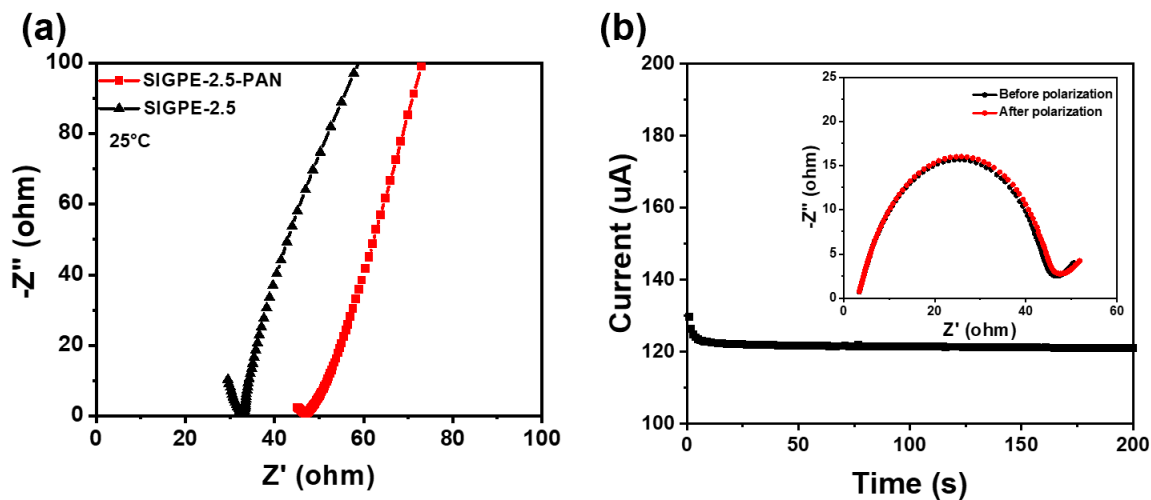


Figure 3.10. (a) EIS profiles of SIPE-2.5 and SIPE-2.5-PAN membranes; (b) time-dependent response of DC polarization curve for the Li|SIPE-2.5|Li symmetric cell (inset is the EIS plots before and after polarization).

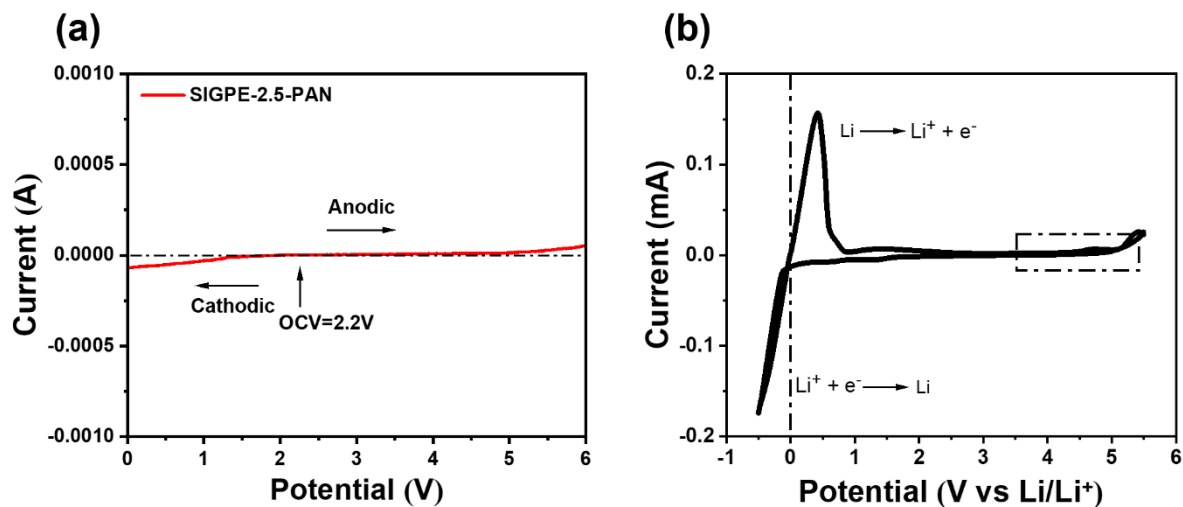


Figure 3.11. (a) LSV curve and (b) CV curve of Li|SIGPE-2.5-PAN|stainless steel cell at room temperature.

Cyclic voltammetry (CV) was carried out from -0.5 to 5.5 V (vs. Li^+/Li) at room temperature to test the electrochemical stability of plasticized SIPE reinforced with PAN-NFs. As shown in **Figure 3.11b**, there was no large current peak over the scan range from 0V to 5.5 V other than the redox peaks at 0 V versus Li^+/Li corresponding to the Li^+ plating and stripping process. [182, 209, 210] Thus, the SIPE-2.5-PAN maintained a wide, stable electrochemical window favorable for practical battery application. Meanwhile, galvanostatic tests of $\text{Li}|\text{SIPE-2.5}|\text{Li}$ and $\text{Li}|\text{SIPE-2.5-PAN}|\text{Li}$ symmetric cells shown in **Figure 3.12** were conducted by Li^+ stripping/plating cycling for 30 minutes under different current densities up to 1000 h to evaluate the long-term lithium cycling stability and dynamic interfacial compatibility of SIPEs. For the SIPE-2.5-PAN symmetric cell (**Figure 3.12a-b**), it is notable that a stable overpotential of 63 mV can be obtained at a current density of 0.1 mA cm^{-2} , after which it increased to 94 mV and 122 mV with higher current densities of 0.2 mA cm^{-2} and 0.5 mA cm^{-2} , respectively. An overpotential of 195 mV was obtained at a high current density of 1 mA cm^{-2} without short circuit, demonstrating a high interfacial stability between SIPE-2.5-PAN and the electrodes, namely, superior electrochemical stability against Li metal during cycling. [182, 211, 212] In contrast, as shown in **Figure 3.5c**, although the SIPE-2.5 symmetric cell had a lower overpotential of 45 mV at a low current density of 0.1 mA cm^{-2} , short circuiting occurred after only about 350 h of cycling when the current density was increased to 0.2 mA cm^{-2} .

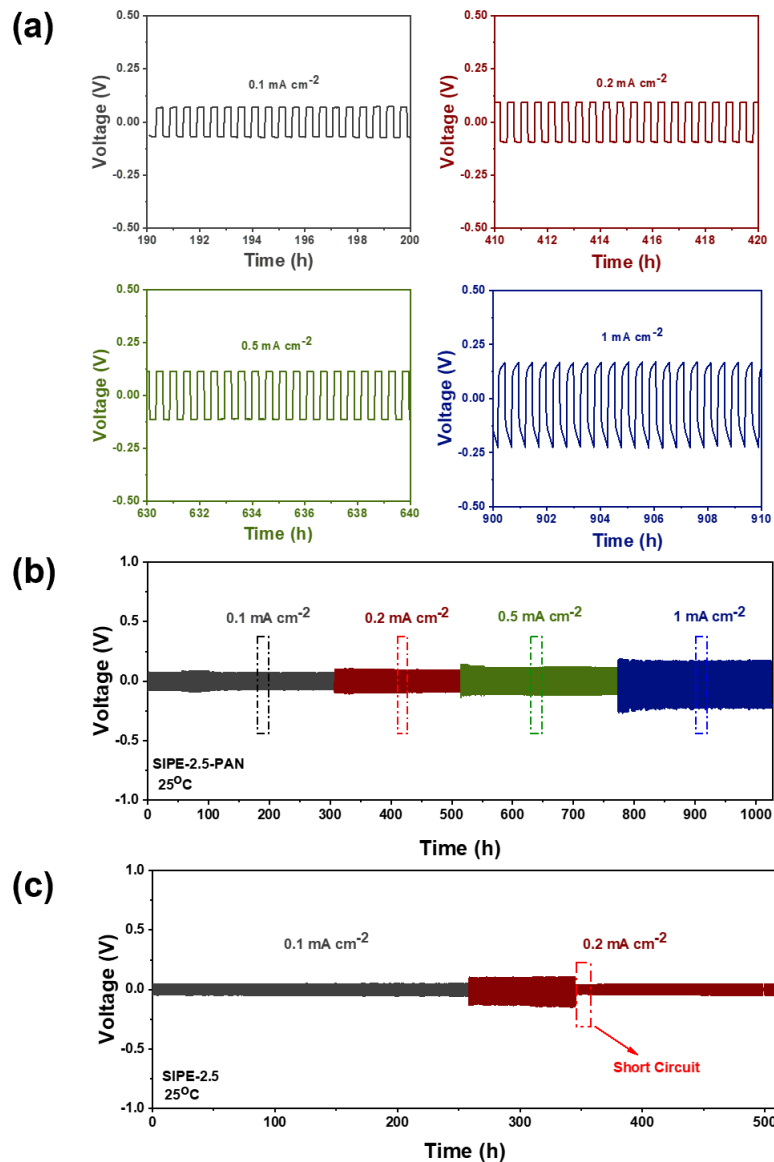


Figure 3.12. Lithium plating/stripping cycles of symmetric (a-b) Li|SIPE-2.5-PAN|Li and (c) Li|SIPE-2.5|Li cells at different current densities.

Figure 3.13a illustrates the probable interfacial lithium dendrite formation between electrolyte/electrode during cycling with the SIPE-2.5 electrolyte. The poor mechanical strength of the SIPE-2.5 membrane likely resulted in continuous lithium dendrite growth with cracking or even potential piercing of the electrolyte, leading to irreversible short circuiting of the battery

after prolonged cycling. [64] In contrast, the embedded PAN-NFs (**Figure 3.13b**) had the ability to provide a robust mechanical reinforcement to suppress dendrite growth and maintain stable battery performance. Afterward, the surface morphologies of Li metal before and after cycling were characterized by FE-SEM to evaluate the Li dendrite formation. As shown in **Figure 3.14**, the majority of Li electrode surface after cycling in Li|SIPE-2.5-PAN|Li symmetric cell was smooth without observable dendrite formation, while the surface of the Li electrode in Li|SIPE-2.5|Li symmetric cell was wrinkled and covered with Li dendrites after cycling. Therefore, the results indicated that SIPE-2.5-PAN exhibited great suppression of lithium dendrites after long cycles due to the improved mechanical strength.

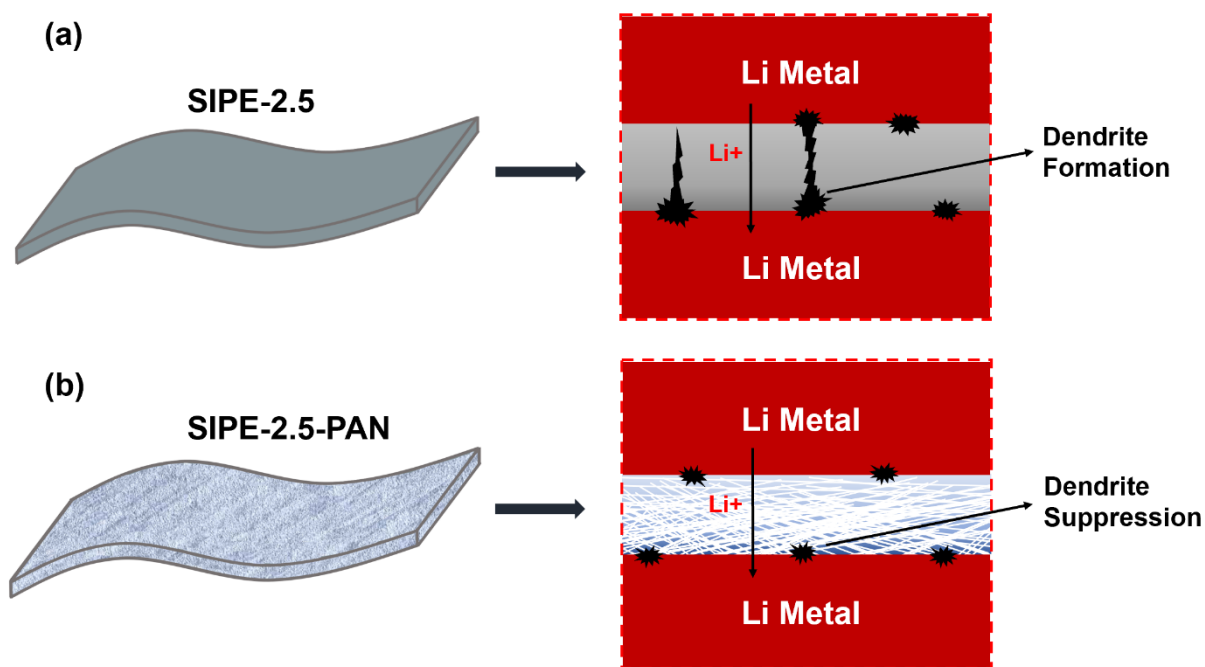


Figure 3.13. Schematic illustration of (a) lithium dendrite formation phenomenon between SIPE-2.5 membrane and Li metal; and (b) lithium dendrite suppression effect between SIPE-2.5-PAN membrane and Li metal.

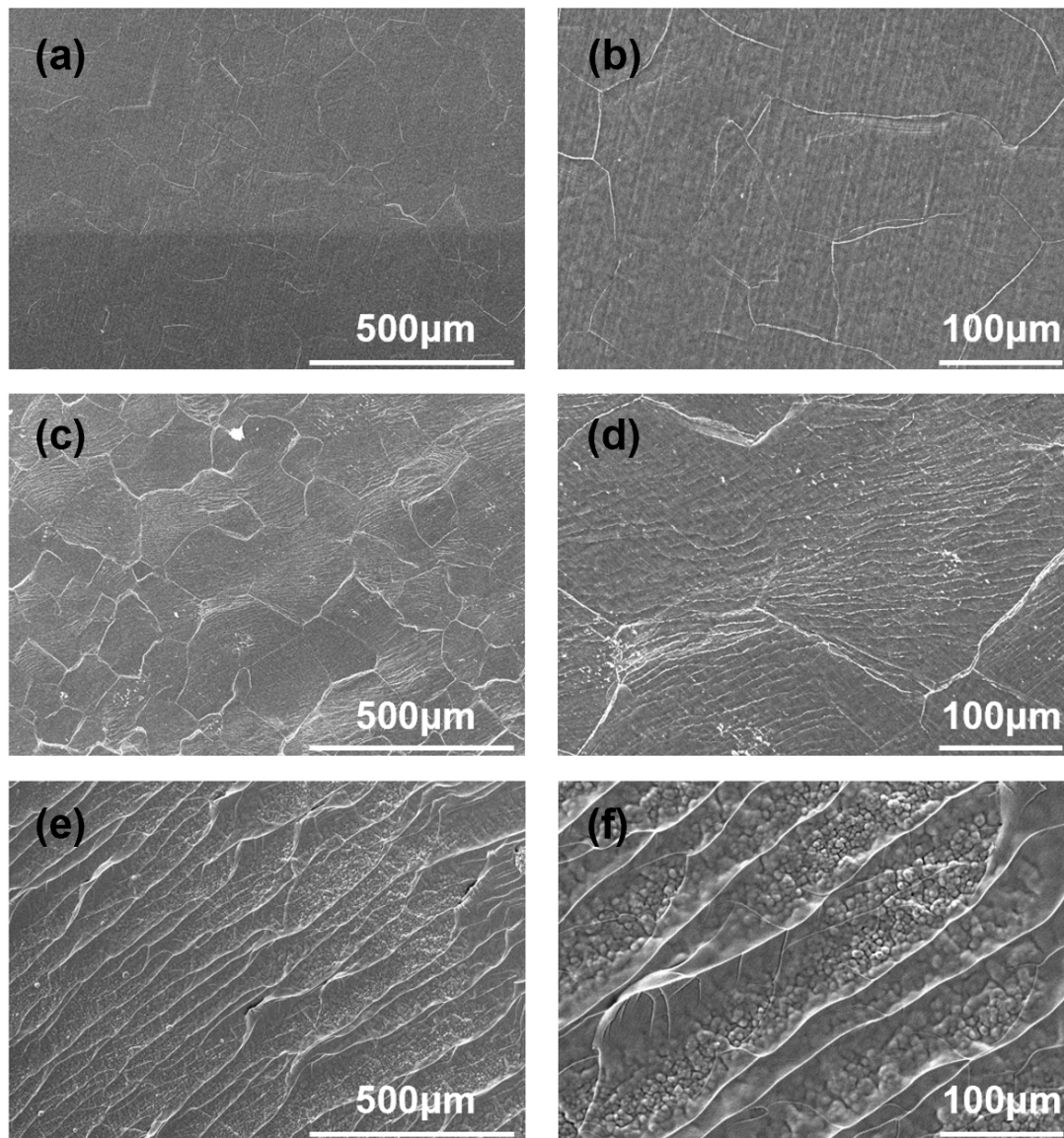


Figure 3.14. SEM images of (a) and (b) fresh Li metal surface; (b) and (c) Li metal surface after cycling in Li|SIPE-2.5-PAN|Li symmetric cell; (e) and (f) Li metal surface after cycling in Li|SIPE-2.5|Li symmetric cell.

3.3.3 High performance of all-solid-state Li-metal batteries

The fabricated plasticized SIPEs with controlled thickness of 80-100 μm were used as the electrolyte in room-temperature all-solid-state Li-metal cells with LFP as the cathode and Li

metal as the anode. Cycling performance of the SIPE-2.5 cell versus the SIPE-2.5-PAN cell running at a current density of 0.2 C (1 C = 170 mAh g⁻¹) is shown in **Figure 3.15a**. The initial discharge capacity of SIPE-2.5 cell was 161 mAh g⁻¹, slightly higher than that of SIPE-2.5-PAN cell (155 mAh g⁻¹) due to the higher ionic conductivity of SIPE-2.5, however, the capacity started to decrease around the 50th cycle and ended at 125 mAh g⁻¹ after 100 cycles (retention rate: 77.6%). In comparison, the discharge capacity of the SIPE-2.5-PAN cell remained at 158 mAh g⁻¹ with a high Coulombic efficiency of near 100% after 100 cycles, indicating an outstanding long-term stability with good reversibility in redox reactions upon cycling. Both SIPE-2.5 and SIPE-2.5-PAN cells exhibited slightly increasing trends with discharge capacity through the initial cycling stage owing to the improving interfacial contact as charging/discharging proceeded. **Figures 3.15b and 3.16** show the charge and discharge curves of 1st, 50th and 100th cycles for solid-state cells with SIPE-2.5-PAN and SIPE-2.5 electrolytes, respectively. The results suggested that the overpotential of the SIPE-2.5-PAN cell decreased from 0.3 V at 1st cycle to 0.25 V at the 50th cycle, which was maintained until the 100th cycle. This indicated an initial decrease in electrode-electrolyte interfacial resistance, followed by stable cycling performance. [182, 213] In contrast, the SIPE-2.5 cell exhibited a continuously changing overpotential of 0.24 V, 0.12 V and 0.27 V at the 1st, 50th and 100th cycles, respectively, indicating a less stable interfacial contact probably due to lithium dendrite growth. The rate capability of Li|SIPE-2.5-PAN|LFP cell was studied and is presented in **Figure 3.15c-d**. The discharge capacities obtained at increasing rates of 0.2, 0.5, 1, 2 and 5 C were 153, 145, 133, 120 and 64 mAh g⁻¹, respectively, after which, upon return to 0.2 C, the discharge capacity returned to the initial value of 153 mAh g⁻¹ (**Figure 3.15c**). Notably, stable charge and discharge plateaus between 3.68 V and 3.27 V were found at the C rates from 0.2 to 2 (**Figure 3.15d**),

corresponding to typical lithium ion extraction/insertion from and into the LFP cathode. [64]

This outstanding rate performance bodes well for all-solid-state Li metal batteries and can be attributed to the high ionic conductivity and nearly unity lithium-ion transference number from the well-crosslinked single-ion conducting structure and mechanically robust PAN-NFs in the plasticized SIPE system. The cycling performance and EIS profiles during cycling of the assembled all-solid-state Li|SIPE-2.5-PAN|LFP cell operated at a high current density of 1 C is illustrated in **Figure 3.15e-f** to ultimately present the practical utility of SIPE-2.5-PAN. As shown in **Figure 3.15e**, a discharge capacity of 117 mAh g⁻¹ can be delivered initially with a Coulombic efficiency staying at 99%. Afterward, the discharge capacity increased due to the improved electrode-electrolyte interfacial contact and remained at 121 mAh g⁻¹ with a high Coulombic efficiency of near 100% after 200 cycles, exhibiting a satisfying capacity retention. This overall performance of SIPE-2.5-PAN electrolyte is competitive in comparison with most other SIPEs reported in literature (**Table 3.3**). Afterward, the EIS changes in **Figure 3.15f** upon cycling indicated that the overall impedance decreased from 244 Ω (fresh) to 187 Ω after 40 cycles and then remained stable for 100 cycles, which likewise demonstrated the improved interfacial contact and reduced interfacial resistance of SIPE-2.5-PAN with the electrodes. In summary, the cell fabricated with SIPE-2.5-PAN presented excellent cycling performance both in low and high current densities, which can be attributed to good ionic conductivity, high lithium-ion transference number, and robust mechanical properties of the SIPE-2.5-PAN membrane.

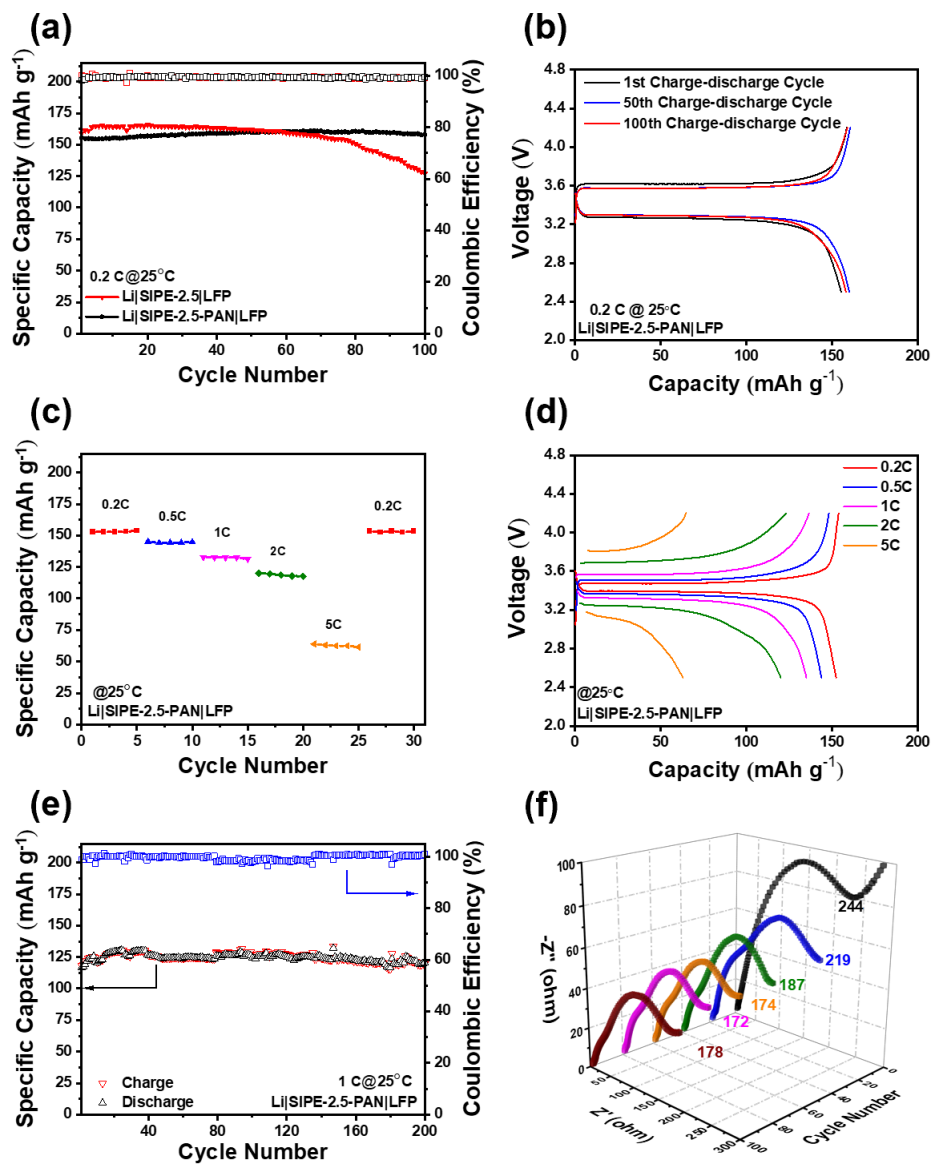


Figure 3.15. (a) Cycling performance at current density of 0.2 C of all-solid-state Li|SIPE-2.5|LFP and Li|SIPE-2.5-PAN|LFP cells operated at 25 °C; (b) Charge-discharge curves of 1st, 50th and 100th cycles of all-solid-state Li|SIPE-2.5-PAN|LFP cell at current density of 0.2 C; (c) Rate capability and (d) Charge-discharge profiles (0.2-5 C) of all-solid-state Li|SIPE-2.5-PAN|LFP cell operated at 25 °C; (e) Cycling performance and (f) EIS evolution curves of all-solid-state Li|SIPE-2.5-PAN|LFP cell at current density of 1C operated at 25 °C.

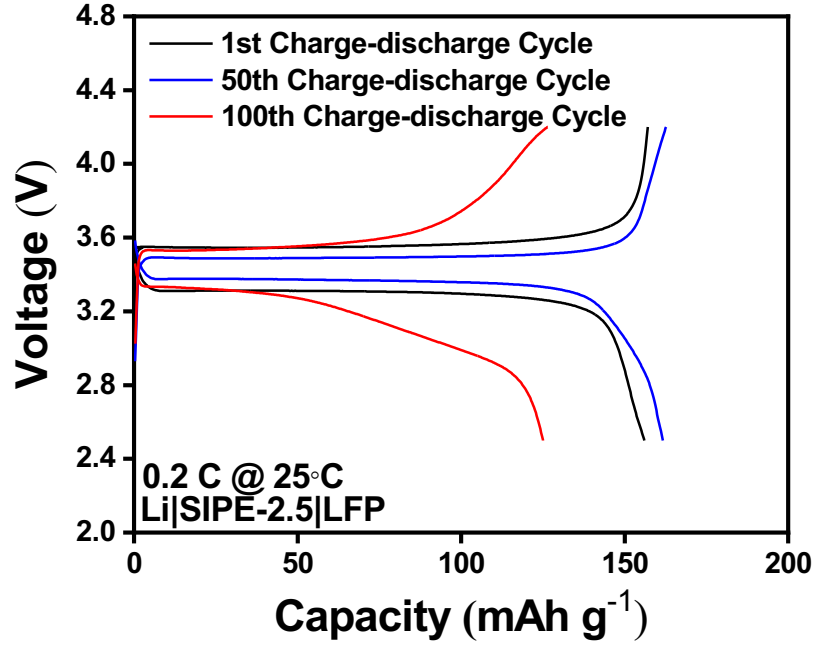


Figure 3.16. Charge-discharge curves of solid-state Li|SIPE-2.5|LFP cell at 1st, 50th and 100th cycles, 0.2 C @ 25°C.

Table 3.3. Mechanical properties, electrochemical and battery performances of different SIPEs.

SIPEs	Types of polymers	Mechanical properties (MPa)	Electrochemical performances			Battery performance		Ref.
			δ (S cm ⁻¹)	t_{Li^+}	ESW (V)	First discharge capacities (mAh g ⁻¹)	Cycling performances (mAh g ⁻¹)	
SIPE-2.5-PAN	Crosslinked polymer	5.91 (YM), 4.45 (TS)	8.09×10^{-4} (RT)	0.92 (60°C)	4.9	Li LFP, 117 @ 1C (RT)	121 @ 1C (RT) after 200 cycles	This work
PEALiFSI	Random copolymer	-	5.84×10^{-4} (25°C)	0.91 (-)	4.0	Li LFP, 159 @ 0.1C (25°C)	95.6% retention @ 0.1C (25°C) after 500 cycles	[214]

Table 3.3. (Continued)

SLIC-PEM	Crosslinked copolymer	0.114 (CM)	1.56×10^{-4} (25°C)	0.91 (30°C)	4.8	Li LFP, 153 @ 0.2C (26°C)	92% retention @ 0.2C (26°C) after 100 cycles	[60]
SIPC-2- PEGDA	Crosslinked copolymer	-	3.2×10^{-5} (70°C)	0.89 (30°C)	4.9	-	-	[215]
LPP@PP	Crosslinked polymer	2.8 (TS)	8.4×10^{-4} (RT)	0.93 (-)	5.2	Li LFP, 133 @ 1C (25°C)	83% retention @ 1C (25°C) after 400 cycles	[64]
es-PVPSI	Blend polymer	-	6.8×10^{-4} (RT)	0.85 (-)	4.5	Li LFP, 110 @ 1C (RT)	100 @ 1C (RT) after 1000 cycles	[9]
ANP-5	Crosslinked polymer	-	1.5×10^{-4} (26°C)	0.95 (26°C)	4.5	Li LFP, - @ 0.5C (RT)	102 @ 0.5C (RT) after 100 cycles	[216]
es-LiSPCE-ns	Homopolym er	10.1 (MS)	1.45×10^{-4} (RT)	0.89 (25°C)	4.7	Li LFP, 111.7 @ 1C (RT)	98.8% retention @ 1C (RT) after 500 cycles	[217]
P(SSPSILi-alt- MA)/PEO	Blend polymer	-	3.08×10^{-4} (25°C)	0.97 (80°C)	5.0	Li LFP, 158.8 @ 0.2C (80°C)	97.5% retention @ 0.2C (80°C) after 100 cycles	[218]
PEO ₈ -LiPCSI	Blend polymer	-	7.33×10^{-5} (60°C)	0.84 (60°C)	5.53	Li LFP, 141 @ 0.1C (RT)	120 @ 0.1C (RT) after 80 cycles	[219]
SII-LE	Triblock copolymer	-	1.45×10^{-4} (RT)	0.92 (RT)	-	-	-	[220]

Table 3.3. (Continued)

SLIGPE-2	Crosslinked copolymer	-	2.74×10^{-5} (RT)	0.622 (RT)	4.7	Li LFP, 133.3 @ 0.1C (RT)	101.2 @ 0.1C (RT) after 150 cycles	[221]
SI10-05- 70%PC	Multiblock copolymer	-	6×10^{-4} (20°C)	1 (30°C)	4.96	Li NMC811, 162 @ 0.5C (20°C)	80% retention @ 0.5C (20°C) after 443 cycles	[207]
Lithiated homopolymer/ PVdF-HFP	Blend polymer	-	5.2×10^{-4} (20°C)	0.9 (40°C)	4.6	Li NMC111, 116 @ 0.1C (20°C)	-, 100 cycles @ 0.1C (20°C)	[208]
HMPE	Crosslinked copolymer	4.7 (TS)	2.24×10^{-3} (25°C)	0.75 (-)	4.91	Li CC-I@GO, - @ 0.5 C (RT)	196 @ 0.5C (RT) after 200 cycles	[4]

3.4 Conclusions

A simple and mechanically-robust plasticized SIPE was successfully developed by UV-initiated polymerization on electrospun PAN-NFs. The well-crosslinked polymer matrix composed of LiSTFSI and PEGDA with PC as the plasticizer provided fast and effective Li^+ conductive pathways with a remarkable ionic conductivity of $8.09 \times 10^{-4} \text{ S cm}^{-1}$, a low activation energy of 0.19 eV, and a superior lithium-ion transference number close to unity ($t_{\text{Li}^+} = 0.92$). The introduction of PAN-NFs significantly improved the mechanical strength and flexibility of the plasticized SIPE. The PAN-NF-reinforced plasticized SIPE also exhibited a wide electrochemical stability window (4.9 V vs. Li^+/Li) and better cycling stability due to the excellent electrochemical performance of PAN-NFs. Lithium symmetric cells assembled with SIPE-2.5-PAN showed superior long-term lithium cycling stability and dynamic interfacial

compatibility. Most importantly, the assembled all-solid-state Li|SIPE-2.5-PAN|LFP cells showed stable cycling performance and remarkable rate capability. They delivered initial discharge capacities of 155 mAh g⁻¹ at 0.2 C and 117 mAh g⁻¹ at 1 C, and further kept high capacities of 158 mAh g⁻¹ at 100th cycle and 121 mAh g⁻¹ at 200th cycle, respectively, with the coulombic efficiency staying at nearly 100%. In conclusion, this straightforward and mechanically reinforced SIPE-2.5-PAN has great potential in the development of advanced all-solid-state Li-metal batteries.

CHAPTER 4: $\text{Li}_{6.28}\text{La}_3\text{Zr}_2\text{Al}_{0.24}\text{O}_{12}$ -reinforced Single-ion Conducting Composite Polymer Electrolyte for Room-Temperature Li-Metal Batteries

Abstract

Composite polymer electrolytes composed of inorganic fillers and organic polymers have been considered to be a promising electrolyte candidate for Li metal batteries with improved safety and suppressed lithium dendrite growth. However, severe concentration polarization effect often occurs in using conventional dual-ion polymer matrix, which could bring in higher internal impedance within cells with decreased lifespan. To address this challenge, plasticized single-ion conducting composite polymer electrolyte (SICE) was designed and fabricated by polymerizing the monomers of lithium (4-styrenesulfonyl) (trifluoromethanesulfonyl) imide (LiSTFSI) and poly(ethylene glycol) methyl ether acrylate (PEGMEA), crosslinker poly(ethylene glycol) diacrylate (PEGDA), silane-modified $\text{Li}_{6.28}\text{La}_3\text{Al}_{0.24}\text{Zr}_2\text{O}_{12}$ nanofibers (s@LLAZO NFs), along with the PEG-based plasticizer tetraethylene glycol dimethyl ether (TEGDME) by heat-initiation. The restrained delocalized anions allow only Li cation migration during charging/discharging process, leading to a superior lithium-ion transference number. The s@LLAZO NFs enabled direct monomer grafting with the polymer matrix, resulting in a controlled formation of an organic-inorganic network that improved the filler content and distribution with enhanced interaction between the filler and polymer matrix in the SICE system. The resultant electrolyte exhibited high ionic conductivity under room temperature, reduced activation energy and excellent oxidation stability which benefited from the well-percolated amorphous region in polymer system and extra Li ion conductive pathways in ceramic structure due to the added plasticizer and LLAZO NFs. Most importantly, all-solid-state Li-metal batteries

assembled with the fabricated SICE demonstrated stable long-term cycling performance and remarkably rate capability at room temperature owing to the improved electrochemical stability with the utilization of fast Li^+ conductors (LLAZO) in the composite structure. Therefore, this novel and straightforward single-ion conducting composite polymer electrolyte has great potential in the development of advanced all-solid-state Li-metal batteries.

4.1 Introduction

Lithium (Li) metal has been considered to be a very promising anode material for next-generation rechargeable energy storage owing to the ultra-high theoretical specific capacity (3860 mA h g^{-1}), low density (0.59 g cm^{-3}), and the most negative electrochemical potential (-3.04 V vs. standard hydrogen electrode). [4, 8-10, 12, 222] Therefore, compared with traditional Li-ion batteries, Li-metal batteries (LMBs) can potentially provide higher capacity and larger operating voltage, thus delivering higher energy density while remaining lightweight, which is extremely promising to satisfy the ever-growing energy demands for portable electronic devices, electric vehicles and grid-energy storage systems. [2, 223] However, severe cycling problem and safety concern happen if Li metal is directly applied to Li-metal batteries with the use of liquid electrolytes. These are the consequences of its dramatic volume variation and related performance degradation due to the intrinsic hostless feature of Li deposition, Li dendritic growth, and accumulation of inactive Li debris. [224] Since the process of Li plating/stripping is a “hostless” behavior, Li atoms tend to aggregate into isolated atomic groups and form into dendritic shapes driven by the thermodynamic factor of a high diffusion barrier. [225] The continuously growing Li dendrites could pierce the separator and cause short circuits and thermal runaway, resulting in catastrophic battery failure. [11] Besides, the Li debris, called “dead Li” that lose electrochemical activity could also be generated when the prolonged Li dendrites detach from the Li metal surface, causing severe active material loss during cycling. [2, 225] Moreover, the drastic volume changes of Li metal anode upon cycling can damage the solid-electrolyte interphase (SEI) film formed between the electrode and the electrolyte, which results in extra consumption of the electrolyte and low Coulombic efficiency, further shortening the lifespan of cells. [226-231]

Tremendous efforts have been taken to develop composite polymer electrolytes (CPEs) to address the aforementioned issues for Li-metal batteries. Composite polymer electrolytes, simply fabricated by introducing inorganic fillers into the polymer electrolyte matrix, can both maintain the advantages of each material, such as high Li ion conductivity, good mechanical rigidity from the inorganic fillers, and excellent electrode/electrolyte interfacial contact, good mechanical flexibility from the organic polymer matrix. [232] In addition, thanks to the embedded inorganic fillers, CPEs also present improved chemical and electrochemical stability for practical applications. [234] Among different types of inorganic fillers, garnet-based ceramic $\text{Li}_7\text{La}_3\text{Zr}_2\text{O}_{12}$ (LLZO), first reported by R. Murugan et al. in 2007, has been considered to be a very most promising Li ion conductor and has been widely investigated due to its high lithium-ion conductivity (10^{-3} to 10^{-4} S cm^{-1}) at room temperature, low activation energy (~ 0.31 eV), excellent stability against lithium metal, wide electrochemical window (~ 5 V), and high mechanical strength. [85, 106, 117, 120] However, the commonly used polymer matrices employing lithium salts like LiTFSI, LiPF_6 , LiClO_4 , LiCF_3SO_3 , etc. for composite polymer electrolytes are usually binary systems. Both Li^+ cations and their counter anions migrate during the charging/discharging process and the overall conductivities of binary salt electrolytes are predominated by the motion of counter anions that have greater mobility than lithium cations. [23-28] Thus, their lithium-ion transference numbers (t_{Li^+}), defined as the fraction of the ionic conductivity that is carried by lithium ions, are undesirably low, typically ranging from 0.1 to 0.4. Consequently, anions are easy to accumulate at the electrode surface and cause severe concentration polarization effect, further resulting in higher internal impedance within cells with decreased lifespan. [1, 37] Although the introduction of inorganic fillers can restrain the movement of anions via strong Lewis acid-base interaction between ceramics and Li salts and

improve the lithium-ion transference numbers to ~ 0.7 , concentration polarization effect could still happen after long-term cycling.

In this work, a novel single-ion conducting composite polymer electrolyte (SICE) was fabricated by anchoring the delocalized anions as side chains on the polymeric backbone of the polymer matrix with the introduction of garnet-type ceramic fillers. Meanwhile, in order to improve the interactions between inorganic fillers and polymer matrix, electrospun $\text{Li}_{6.28}\text{La}_3\text{Al}_{0.24}\text{Zr}_2\text{O}_{12}$ nanofibers (LLAZO NFs) were modified by covalently bonding silane with acrylate functional groups ($\text{CH}_2=\text{CHCOO}-$) on the surface, enabling the chemical reactivity of silane-decorated LLAZO NFs with functional monomers. [182] Herein, this new SICE was realized by polymerizing the monomers of lithium (4-styrenesulfonyl) (trifluoromethanesulfonyl) imide (LiSTFSI) and poly(ethylene glycol) methyl ether acrylate (PEGMEA), crosslinker poly(ethylene glycol) diacrylate (PEGDA), silane-modified LLAZO NFs, along with the PEG-based plasticizer tetraethylene glycol dimethyl ether (TEGDME) by heat-initiation. The resultant polymerization created a well-percolated organic-inorganic network within the SICE system, generating continuously effective and fast Li ion conductive pathways. The covalently bonded lithium salt anions on the polymer backbone yielded a high lithium-ion transference number. The silane coupling agent dramatically enhanced the interaction between the LLAZO NFs and the polymer matrix, leading to more homogeneous distribution of inorganic Li^+ conductors with improved mechanical strength. [17] As a result, the fabricated SICE presented high ionic conductivity, reduced activation energy, wider electrochemical stability window, and better cycling stability. The all-solid-state Li|LFP cells constructed by this introduced SICE exhibited stable cycling performance and remarkable rate capability with high Coulombic efficiency.

4.2 Experimental Section

4.2.1 Materials

Oxalyl chloride ((CO)₂Cl₂), N,N-dimethylformamide (DMF), acetonitrile (CH₃CN), sodium 4-vinylbenzenesulfonate, triethylamine (TEA), 4-dimethylamino pyridine (DMAP), dichloromethane (DCM), sodium bicarbonate (NaHCO₃), hydrochloric acid (HCl), potassium carbonate (K₂CO₃), lithium perchlorate (LiClO₄), tetraethylene glycol dimethyl ether (TEGDME), lithium nitrate (LiNO₃), zirconium butoxide solution (Zr(OCH₂CH₂CH₂CH₃)₄), aluminum nitrate nonahydrate (Al(NO₃)₃·9H₂O), 80 wt.% in ethanol), acetic acid (CH₃CO₂H), polyvinylpyrrolidone (PVP, M_w=1,300,000), 3-(trimethoxysilyl)propyl methacrylate (silane), ethanol, 1-methyl-2-pyrrolidinone (NMP), bis(trifluoromethane)sulfonimide lithium salts (LiTFSI), poly(ethylene glycol) diacrylate (PEGDA, M_w=700), poly(ethylene glycol) methyl ether acrylate (PEGMEA, M_w= 360), 2,2'-Azobis(2-methylpropionitrile) (AIBN), dimethyl sulfoxide-d₆ (DMSO-d₆), and N-methyl-2-pyrrolidone (NMP) were purchased from Sigma-Aldrich. Trifluoromethanesulfonamide was purchased from Oakwood Chemical. Lanthanum nitrate hexahydrate (La(NO₃)₃·6H₂O) was purchased from Alfa-Aesar. Acetonitrile and DMF were dried and stored with 4A molecule sieves before use. Other chemicals were used as received without further purification.

4.2.2 Synthesis of monomer lithium (4-styrenesulfonyl) (trifluoromethylsulfonyl) imide

As shown in **Figure 4.1**, the lithium (4-styrenesulfonyl) (trifluoromethylsulfonyl) imide (LiSTFSI) monomer was synthesized in the two-step method as described in the literature [61, 213] Monomer potassium (4-styrenesulfonyl) (trifluoromethylsulfonyl) imide (KSTFSI) was

synthesized in the first step and then it was converted to the LiSTFSI monomer with a metathesis reaction, as described below in more details.

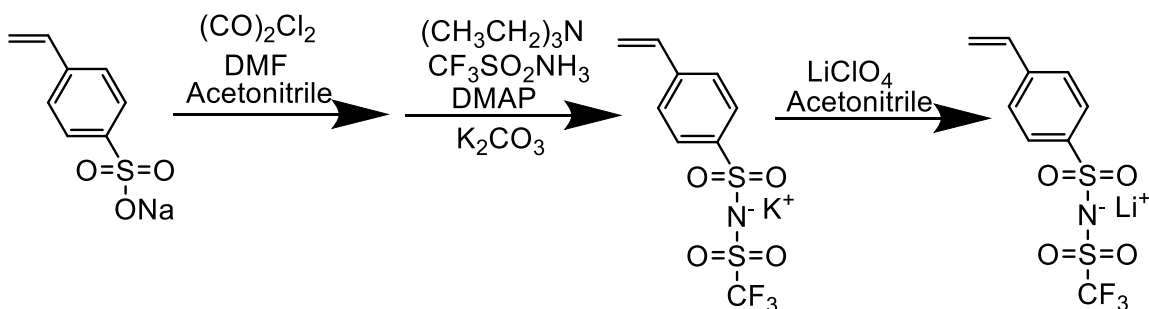


Figure 4.1. Schematic illustration of the chemical synthetic process of LiSTFSI.

During the synthesis of KSTFSI, $(\text{CO})_2\text{Cl}_2$ (46.6 mmol, 4 ml) and DMF (2 mmol, 190 μl) were well-dissolved in 80 ml dried acetonitrile and stirred at room temperature for 5 hours. Then, 4-vinylbenzenesulfonate (38.8 mmol, 8 g) was added into the solution under argon atmosphere when the color turned light yellow. The mixture was stirred for 24 hours inside the laboratory hood at room temperature. A separate colorless solution was formed by gradually mixing TEA (116.2 mmol, 16.2 ml), DMAP (48.1 mmol, 5.4 g) and trifluoromethanesulfonamide (38.8 mmol, 5.78 g) in 60 ml dried acetonitrile under magnetic stirring for 1 hour at room temperature. Subsequently, a clear light-brown 4-styrene sulfonyl chloride solution was obtained after the precipitate NaCl was filtered from the mixture. The colorless solution was dropwise added into 4-styrene sulfonyl chloride solution under an ice bath with vigorous magnetic stirring. The ice bath was removed when the mixed solution cooled down. The solution turned brown and was vigorously stirred for 16 hours inside the laboratory hood at room temperature. The solvent was removed by rotary evaporation and the resulting brown solid was dissolved in 100 ml DCM. The following solution was washed by 40 ml 4% NaHCO_3 aqueous solution three times and 40 ml 37% HCl aqueous solution. The intermediate product of potassium (4-styrenesulfonyl)

(trifluoromethylsulfonyl) imide (KSTFSI) was synthesized by neutralization of the acid monomer with excess 0.5 mol/L K_2CO_3 aqueous solution. The obtained white suspension was stirred at room temperature for 1 hour and filtered to get a slightly yellow solid. The resulting solid, KSTFSI, was dried under high vacuum at 60°C overnight (30% yield).

The synthesis of KSTFSI was confirmed by 1H NMR and ^{13}C NMR (**Figure 4.2**). 1H NMR (600 MHz; DMSO- d_6 ; ppm): 7.7705 (d, 2H); 7.6296 (d, 2H); 6.8393 (q, 1H); 6.0254 (d, 1H); 5.4370 (d, 1H); ^{13}C NMR (600 MHz; DMSO- d_6 ; ppm): 144.7104; 140.1258; 136.1100; 126.9751; 126.4349; 117.1459.

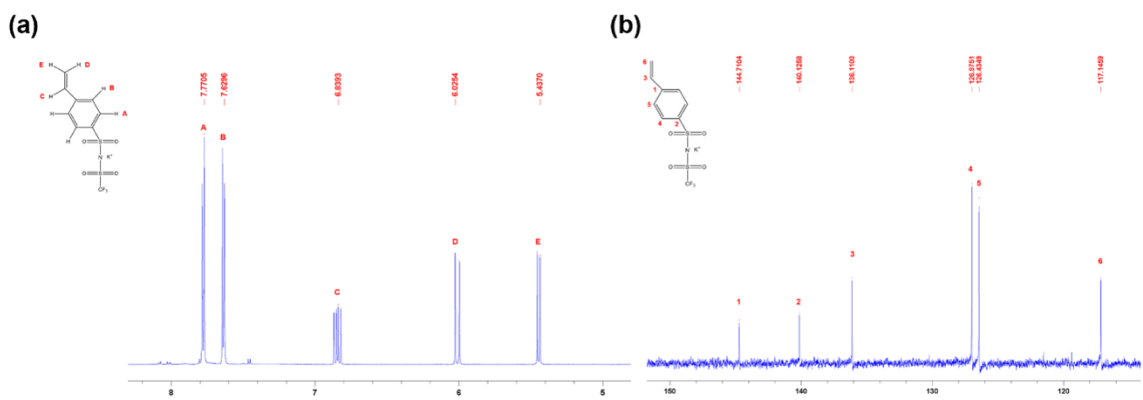


Figure 4.2. (a) 1H NMR and (b) ^{13}C NMR spectra of KSTFSI.

After the synthesis and confirmation of KSTFSI, LiSTFSI was synthesized by a metathesis reaction between KSTFSI and $LiClO_4$. KSTFSI powder (8.5 mmol, 3 g) was added in 100 ml dried acetonitrile under argon atmosphere and stirred until the powder was completely dissolved. $LiClO_4$ (8.5 mmol, 0.91 g) was well-dissolved in 20 ml dried acetonitrile and added into the KSTFSI solution by needled syringe. The resulting solution was stirred under argon atmosphere at room temperature overnight. The white $KClO_4$ precipitate was filtered and the solvent was removed via rotary evaporator. The obtained white solid was recrystallized from deionized water

and then dried under high vacuum at 60°C to get pure white LiSTFSI powder (37% yield). The final product LiSTFSI was stored in a glovebox (H_2O , $\text{O}_2 < 0.5$ ppm) for further use.

The obtained LiSTFSI was confirmed by ^1H NMR, ^{13}C NMR, and ^{19}F NMR (**Figure 4.3**). ^1H NMR (600 MHz; DMSO-d_6 ; ppm): 7.7845 (d, 2H); 7.6435 (d, 2H); 6.8505 (q, 1H); 6.0263 (d, 1H); 5.4553 (d, 1H); ^{13}C NMR (600 MHz; DMSO-d_6 ; ppm): 146.1972; 141.6377; 137.6047; 128.4788; 127.9381; 118.6575; ^{19}F NMR (600 MHz; DMSO-d_6 ; ppm): 77.8133 (s, 3F).

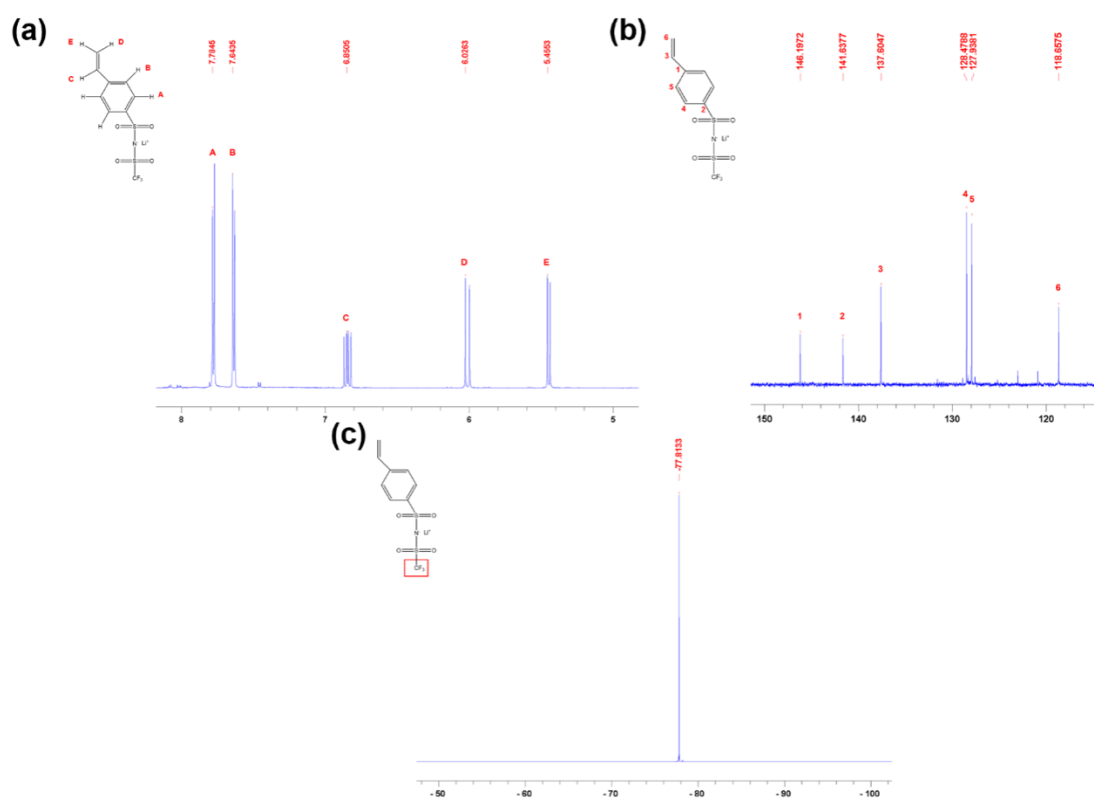


Figure 4.3. (a) ^1H NMR, (b) ^{13}C NMR, and (c) ^{19}F NMR spectra of LiSTFSI.

4.2.3 Fabrication of $\text{Li}_{6.28}\text{La}_3\text{Al}_{0.24}\text{Zr}_2\text{O}_{12}$ nanofibers

The electrospinning precursor solution was first prepared by dissolving stoichiometric amount of 9.42 mmol of LiNO_3 , 4.5 mmol of $\text{La}(\text{NO}_3)_3 \cdot 6\text{H}_2\text{O}$, 3 mmol of $(\text{Zr}(\text{OCH}_2\text{CH}_2\text{CH}_2\text{CH}_3)_4$ and 0.36 mmol of $\text{Al}(\text{NO}_3)_3 \cdot 9\text{H}_2\text{O}$ in a mixed solvent composed of 16 ml DMF and 4 ml acetic acid.

Excess LiNO_3 (15 wt%) was added to compensate for lithium loss during the subsequent calcination procedure. Then 2 g of PVP was added after stirring the mixed solution for 30 min. The precursor solution was mechanically stirred overnight. Electrospinning was conducted at a high voltage of 10 kV with a feeding rate of 0.45 ml h^{-1} . The as-spun nanofibers were later calcined at $850 \text{ }^\circ\text{C}$ for 2 h at ambient environment to obtain LLAZO nanofibers (LLAZO NFs). The calcinated LLAZO were further stored at vacuum oven under high temperature for future use.

4.2.4 Fabrication of silane modified $\text{Li}_{6.28}\text{La}_3\text{Al}_{0.24}\text{Zr}_2\text{O}_{12}$ nanofibers (s@LLAZO)

For the fabrication of silane-modified $\text{Li}_{6.28}\text{La}_3\text{Al}_{0.24}\text{Zr}_2\text{O}_{12}$ nanofibers (s@LLAZO), the silane precursor solution was first prepared by mixing 2.5 vol% 3-(trimethoxysilyl)propyl methacrylate, 2.5 vol% acetic acid, 5 vol% water, and 90 vol% ethanol, and stirred for 1 h to stabilize the pH value and to activate alkoxy groups to silanols ($\equiv\text{Si}-\text{OH}$). LLAZO nanofibers (600 mg) were introduced into 40 ml of precursor solution, which was stirred for 6 h for hydrolysis reaction according to our previous work. [182] After silanization, the resulting s@LLAZO nanofibers were washed three times with ethanol by centrifugation, followed by drying at 60°C under high vacuum overnight for further use.

4.2.5 Preparation of single-ion conducting composite polymer electrolytes

The single-ion conducting composite polymer electrolytes (SICEs) were simply prepared by one-pot free radical polymerization employing AIBN as the initiator in a glovebox. According to our previous work, [11] PEGDA, PEGMEA and LiSTFSI solution with a molar ratio of [EO] and $[\text{Li}^+]$ fixed at 24:1 was prepared as the crosslinking polymer system for SICE fabrication. Herein,

a polymer solution of PEGMEA and PEGDA at a weight ratio of 3:2 was mixed with 0.2 wt.% AIBN, after which 32 mg LiSTFSI was added to prepare the precursor solution matrix. Different amount of s@LLAZO NFs based on the weight percentage of polymer matrix from 0 to 50% was introduced and the resulting solutions were sonicated until s@LLAZO NFs were uniformly distributed. The well-prepared precursor SICE solutions were cross-linked into thin films between two transparent quartz plates by heating at 110 °C for 10 mins in a glovebox. The fabricated SICE membranes with different weight percentages of s@LLAZO NFs were denoted as SICE_x, where x represents to 0, 10, 20, 30, 40, 50, corresponding to 0, 10%, 20%, 30%, 40%, 50%, respectively. In order to improve the ionic conductivity and wetting ability of SICE, 50% TEGDME based on the weight of the precursor solution was introduced before crosslinking and the resulting plasticized system was denoted as p-SICE_x for further electrochemical test and battery assembly.

4.2.6 Structure characterization

¹H NMR, ¹³C NMR, and ¹⁹F NMR spectra analyses were conducted on Bruker NEO 600 MHz Polk NMR spectrometer with DMSO-d₆ as the solvent. Fourier transform-infrared spectroscopy (FTIR, Thermo Scientific™ Nicolet™ iS™10) was used to identify the functional groups of silane, LLAZO NFs, s@LLAZO NFs, LiSTFSI powder, PEGDA, PEGMEA solution and SICE₃₀ membrane at the range of 1800~700 cm⁻¹ with 32 scans and resolution of 4 cm⁻¹ at room temperature. X-ray diffraction (XRD) was applied to identify the crystal structures of calcinated LLAZO NFs using a Rigaku D/Max 2400 (Japan) with Cu K α radiation ($\lambda=1.5418$ Å) in a 2 θ angle range from 10° to 50°. A universal mechanical test machine (MTS Criterion, Loading: 100 N) was also utilized to measure the mechanical properties of SICE_x membranes with a cross-

head speed of 0.5 mm/min. Thermo-gravimetric analysis (TGA, Perkin Elmer Pyris 1) was used with a heating rate of 10 °C min⁻¹ under nitrogen atmosphere to test the thermal properties of s@LLAZO NFs, p-SICE₀, p-SICE₃₀ membranes. Differential scanning calorimetry (DSC) was carried out at a heating/cooling rate of 2 °C min⁻¹ using a TA Instrument Discovery Series to measure the glass transition temperatures (T_g) of SICE₀, SICE₃₀ and p-SICE₃₀ membranes. The morphologies of LLAZO NFs, s@LLAZO NFs, p-SICE₃₀ membrane and Li metal anode after cycling were characterized by field-emission scanning electron microscopy (FE-SEM, FEI Verios 460L, USA) with EDX mapping. ImageJ Software was used to measure the thickness of p-SICE₃₀.

4.2.7 Electrochemical performance evaluation

Ionic conductivities of all SICEs were determined by electrochemical impedance spectroscopy (EIS, Garmy Reference 600 device) over a frequency range of 0.1 Hz to 1 MHz with an AC potential of 10 mV. SICE membranes were pouched and sandwiched between two stainless steel blocking electrodes for electrochemical impedance test. The ionic conductivity (δ , S cm⁻¹) was calculated by the following equation:

$$\delta = t/R_b A \quad (4.1)$$

where t is the thickness of SICE membrane, R_b the membrane bulk resistance obtained from the intercept of extended semicircle with the real axis on the Nyquist plot, and A the area of the membrane. Activation energy (E_a , eV) of SICEs was calculated with an Arrhenius plot of ionic conductivities under different temperatures by the Arrhenius equation:

$$\delta = A \exp(-E_a/RT) \quad (4.2)$$

where δ is the ionic conductivity, A the dc conductivity of pre-exponential factor, E_a the activation energy, R the molar gas constant, and T the absolute temperature.

Lithium-ion transference number (t_{Li^+}) of each SICE membrane was determined by chronoamperometry testing and electrochemical impedance spectroscopy (EIS) measurement at 60°C. A symmetric lithium cell was assembled and tested by EIS with a frequency ranging from 0.1 Hz to 1 MHz before and after polarization. Chronoamperometry was performed with an applied DC potential of 10 mV. The t_{Li^+} value was calculated by Bruce's equation:

$$t_{Li^+} = I_{SS} (\Delta V - I_0 R_{i,0}) / I_0 (\Delta V - I_{SS} R_{i,SS}) \quad (4.3)$$

where ΔV is the polarization potential, I_0 and I_{SS} the initial and steady-state currents before and after polarization, R_0 and R_{SS} the initial and steady-state total resistances before and after polarization.

Linear sweep voltammetry (LSV) was conducted to assess the electrochemical stability of p-SICE₃₀ using Li|p-SICE₃₀|stainless steel cells with a scan rate of 10 mV s⁻¹ over a voltage range of 0-6 V (vs. Li⁺/Li). Cyclic voltammetry (CV) was also carried out on Li|p-SICE₃₀|stainless steel cells at a scan rate of 0.5 mV s⁻¹ from -0.5 to 5.5 V (vs. Li⁺/Li) at room temperature.

Galvanostatic cycling testing of Li|p-SICE₃₀|Li symmetric cell was conducted at room temperature to evaluate the structural stability of p-SICE₃₀ by sandwiching a p-SICE₃₀ membrane (60-80 μm thickness and 1/2 inch diameter) between two Li foils (7/16 inch diameter) and cycling at current densities of 0.2 and 0.5 mA cm⁻² with current direction reversed every 30 minutes.

4.2.8 Battery Performance Evaluation

All-solid-state Li|LiFePO₄ (LFP) cells were fabricated for evaluating the performance of p-SICE₃₀ membranes in room-temperature all-solid-state batteries. For comparison, liquid electrolyte Li|LFP cells were also prepared by placing PP separator (Celgard, LLC) and soaking with commercial liquid electrolyte (1 M LiPF₆ in (1:1 vol) EC/DMC). The LFP cathode was prepared by mixing a slurry of LFP, ionic liquid solution of TEGDME with LiTFSI in equimolar amounts, carbon black (C65), and polyvinylidene fluoride (PVDF) binder at a weight ratio of 7:2:0.5:0.5 in NMP solvent, which was uniformly coated on aluminum foil by a doctor blade set at 15 mm. The prepared cathode was dried under high vacuum at 60 °C overnight to remove NMP solvent. The LFP cathode was then punched into disks with a diameter of 7/16 inches with an active material loading around 1.5-2.0 mg cm⁻². Standard LIR2032 coin cells were assembled in a glovebox by sandwiching p-SICE₃₀ and liquid electrolyte-soaked PP membrane disks of 1/2 inch diameter between pre-punched LFP cathode and Li foil. The cycling performance of all-solid-state and liquid-state Li|LFP cells was then tested by an Arbin battery tester in a potential range of 2.5 V to 4.2 V.

4.3 Results and Discussion

Figure 4.4 shows the schematic of synthesis procedure of plasticized SICE membrane used in this work. According to our previous work, [182] silane-coated LLAZO NFs (s@LLAZO) were fabricated via a hydrolysis reaction between activated alkoxy groups of silanols ($\equiv\text{Si}-\text{OH}$) and LLAZO NFs under acidic environment for 6 h. After that, s@LLAZO NFs were introduced into the polymer matrix composed of the monomers of LiSTFSI, PEGMEA and crosslinker PEGDA mixed in the plasticizer of TEGDME. It is seen that the acrylate functional groups

(CH₂=CHCOO-) on s@LLAZO surface can involve the polymerization and form a controlled organic-inorganic crosslinked network by heat-initiation.

Consequently, the well-controlled SICE membrane maintained a homogenous distribution of ceramic fillers, forming a percolated network with fast Li⁺ transportation. In addition, the improved binding force and reduced interfacial resistance between the polymer and inorganic nanofibers can endow the SICE with a higher content of inorganic fillers and enhanced mechanical property. [182] Meanwhile, the plasticizer can not only help to decrease the crystallinity and increase the amorphous region of polymer matrix, but also refine the wetting ability of the SICE, thus enabling a better interfacial contact between the electrolyte and electrodes. Free-standing SICE films with different s@LLAZO contents were prepared and denoted as p-SICP_x, where p represents plasticized electrolyte and x is the weight content of s@LLAZO nanofibers.

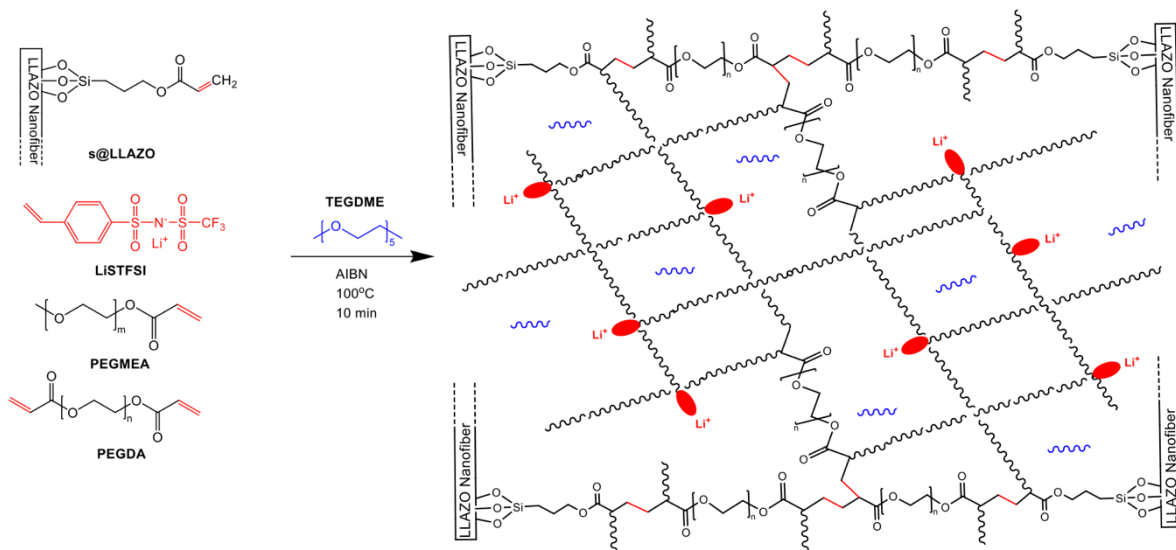


Figure 4.4. Schematic of synthesis procedure of plasticized SICE membrane with a well-crosslinked inorganic-organic network, providing fast Li⁺ conductive pathways.

4.3.1 Design of single-ion conducting composite polymer electrolytes

The scanning electron microscopy (SEM) images and X-ray diffraction (XRD) pattern in **Figure 4.5** show the morphology and crystal structure of calcined LLAZO NFs, respectively. It can be observed that the fabricated LLAZO ceramic fillers retained nanofibrous shape after calcination with the main peaks in XRD diffraction pattern clearly indexed with the cubic LLZO crystal structure. [182] Afterward, silane coupling agent was grafted on the surface of calcined LLAZO NFs via hydrolysis reaction. As shown in **Figure 4.6a**, the SEM image and EDAX mapping of s@LLAZO NFs demonstrated that silane coupling agent was uniformly coated along the one-dimensional fiber direction. To further investigate the surface structure of silane-grafted ceramic nanofillers, Fourier transform Infrared Spectroscopy (FTIR) was conducted to analyze silane agent, pristine LLAZO and s@LLAZO NFs. The FTIR spectra in **Figure 4.7** indicates that there are additional absorption peaks presenting for s@LLAZO NFs after hydrolysis reaction compared to pristine LLAZO NFs. The main absorption peaks located at 1310, 1090, and 940 cm^{-1} can be attributed to the stretch of COO- (acrylate), stretching vibration of Si-O (siloxane), and bending vibration of C=C (vinyl group), respectively, [244, 245] confirming the presence of silane coupling agent chemically bonded on the surface of s@LLAZO NFs. As for the single-ion conducting polymer matrix, the repeat unit of $-\text{CH}_2-\text{CH}_2-\text{O}-$ (EO) in a PEO-based polymer is responsible for lithium-ion complexation and transportation, [7] so that the molar ratio of $[\text{EO}]/[\text{Li}^+]$ was kept at 24:1 for polymer system in this paper according to our previous work. [11]

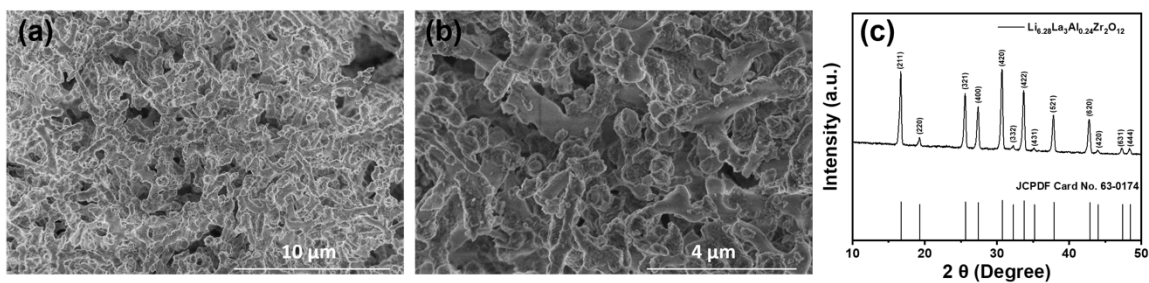


Figure 4.5. (a and b) SEM images and (c) XRD pattern of calcinated LLAZO NFs.

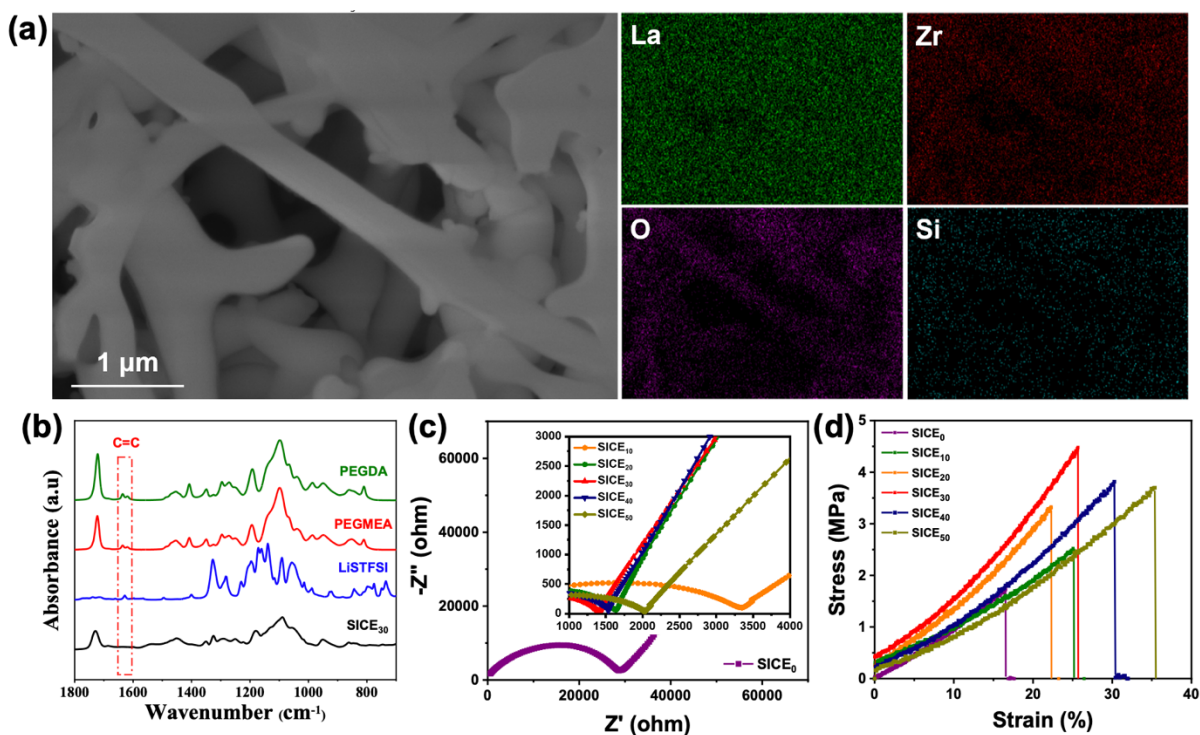


Figure 4.6. (a) SEM image and EDAX mapping of La, Zr, O, Si elements of s@LLAZO NFs; (b) FTIR spectra of PEGDA, PEGMEA, LiSTFSI and SICE₃₀; (c) EIS profiles of SICE_x with different s@LLAZO NF contents at room temperature; (d) Stress–strain curves of SICE_x at room temperature.

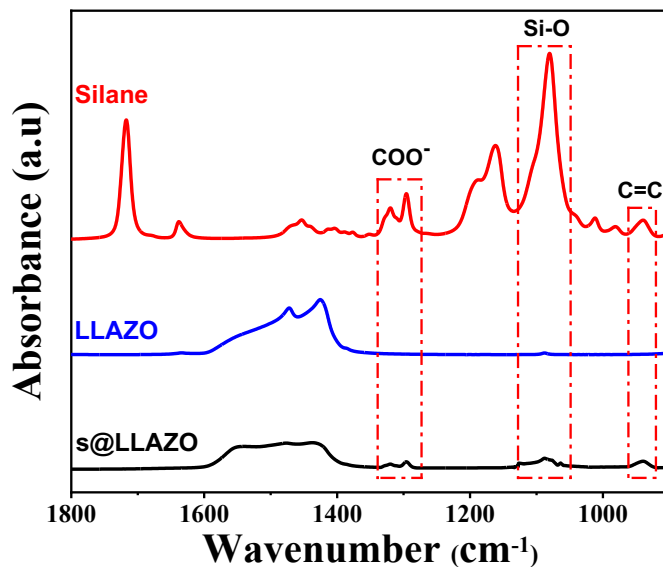


Figure 4.7. FTIR spectra of silane, LLAZO and s@LLAZO NFs.

Table 4.1. Ionic conductivities and mechanical properties of SICE_x with different s@LLAZO NF contents at room temperature.

SICE samples	s@LLAZO content (%)	Ionic conductivities (S cm ⁻¹)	Young's modulus (MPa)	Tensile strength (MPa)	Elongation (%)
SICE ₀	0	5.05×10 ⁻⁷	12.6	1.72	16.53
SICE ₁₀	10	4.32×10 ⁻⁶	11.4	2.48	25.13
SICE ₂₀	20	8.89×10 ⁻⁶	18.7	3.31	22.30
SICE ₃₀	30	1.03×10 ⁻⁵	19.8	4.48	25.67
SICE ₄₀	40	9.44×10 ⁻⁶	15.0	3.82	30.30
SICE ₅₀	50	7.15×10 ⁻⁶	12.7	3.70	35.37

Different contents of s@LLAZO NFs were introduced into the polymer matrix to investigate the ionic conductivities of the resultant SICEs. As shown in **Figure 4.6c**, the electrochemical impedance spectroscopy (EIS) was applied for testing the ionic conductivities of SICE films with different contents of s@LLAZO NFs and the results are summarized in **Table 4.1**. Without s@LLAZO NFs, the ionic conductivity of bare polymer electrolyte was $5.05 \times 10^{-7} \text{ S cm}^{-1}$ (SICE₀). The ionic conductivity increased dramatically to $1.03 \times 10^{-5} \text{ S cm}^{-1}$ (SICE₃₀) with introducing 30 wt.% s@LLAZO NFs to the system. This is because well-percolated organic-inorganic network was created in the resultant SICE₃₀, where the amorphous region of polymer matrix was increased with added fillers and LLAZO NFs provided extra Li ion conductive pathway within the inorganic structure by ion hopping, [8] consequently leading to the increased ionic conductivity. In order to better realize the improvement on Li ion transportation with well-percolated organic-inorganic structure by introducing silane-modified LLAZO NFs, the ionic conductivity comparison was illustrated in **Figure 4.8** between SICEs with s@LLAZO NFs and pristine LLAZO NFs. It is seen that after introducing 10 wt.% pristine LLAZO NFs, the ionic conductivity decreased to $3.85 \times 10^{-6} \text{ S cm}^{-1}$, which was close to the conductivity of bare polymer electrolytes, due to the severe aggregation of inorganic filler within the polymer matrix. [246-248] In contrast, after introducing 30 wt.% s@LLAZO, the resultant SICE possessed the optimum ionic conductivity of $1.03 \times 10^{-5} \text{ S cm}^{-1}$, after which the ionic conductance reduced slightly with continue increase in s@LLAZO NF content, probably because the content of the fillers was beyond to the maximum capacity of the system and fillers reached to the interface created between filler and polymer. [249, 250] The increased ionic conductivity by the introduction of s@LLAZO NFs is owing to the silane coated layer that helped to mitigate the agglomeration effect of introduced fillers and further establish percolated network within the

SICE system for faster and more effective Li^+ conduction. [182] The mechanical properties of resultant SICE membranes were further studied and shown as the strain-stress curves in **Figure 4.6d** with data summarized in **Table 4.1**. The pristine crosslinked polymer electrolyte showed a Young's modulus of 12.6 MPa, a tensile strength of 1.72 MPa, and maximum elongation of 16.53%. After the introduction of s@LLAZO NFs, SICE₃₀ exhibited the maximum Young's modulus and tensile strength of 19.8 MPa and 4.48 MPa, respectively, due to the high rigidity nature of inorganic ceramics and enhanced filler/polymer interface interaction.

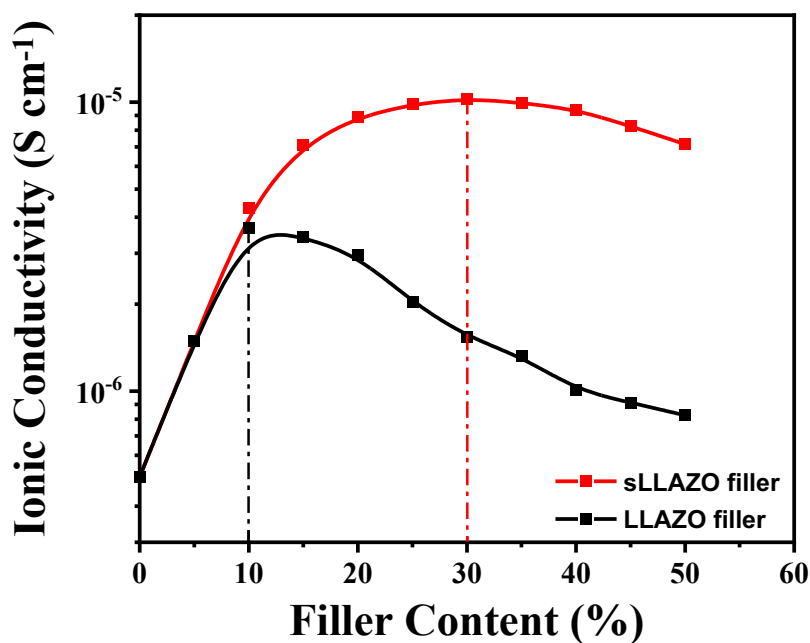


Figure 4.8. Ionic conductivities of SICEs with s@LLAZO NFs and pristine LLAZO NFs at different filler contents.

4.3.2 Electrochemical performance of single-ion conducting composite polymer electrolytes

PEG-based plasticizer was added into the SICE₃₀ system, named as p-SICE₃₀, to increase its ionic conductivity for room-temperature battery cycling and improve the electrolyte/electrode

interfacial contact for better cycling stability. The reasons for employing oligomer PEG molecules are that they not only help space the long chains apart to improve the mobility of amorphous region, but also enhance the interface between inorganic fillers and organic polymer matrix. [251] As presented in **Figure 4.9a** and **Table 4.2**, p-SICE₃₀ exhibited an enhanced ionic conductivity of $3.43 \times 10^{-4} \text{ S cm}^{-1}$ at room temperature owing to the improved ion pair dissociation, polymer segmental motion and vehicular transport of the solvated cation. [66] Their activation energies were investigated by testing the ionic conductivities under different temperatures, illustrated by Arrhenius plots in **Figure 4.9b**, and the calculated results are presented in **Table 4.2**. All ionic conductivity-temperature curves obeyed the classical Arrhenius linear relationship within the testing temperature range (20 ~ 80 °C). The activation energy was calculated as 0.44 eV for bare polymer electrolyte, while it decreased significantly to 0.20 eV with the introduction of s@LLAZO NFs and plasticizer for p-SICE₃₀, indicating a lower energy barrier in transporting lithium cations within the plasticized composite polymer system. Afterward, differential scanning calorimetry (DSC) was then conducted to measure the glass transition temperatures (T_g) of SICE films, presented in **Figure 4.10**. From **Figure 4.10** and **Table 4.2**, it is seen that due to the introduction of s@LLAZO NFs which decreased the crystallinity of polymer matrix, SICE₃₀ had a lower glass transition temperature of -39.2 °C compared to the bare polymer electrolyte (-22.5 °C). Then the added plasticizer further reduced the glass transition temperature to -74.6 °C for p-SICE₃₀, demonstrating the greatly increased amorphous network within polymer system.

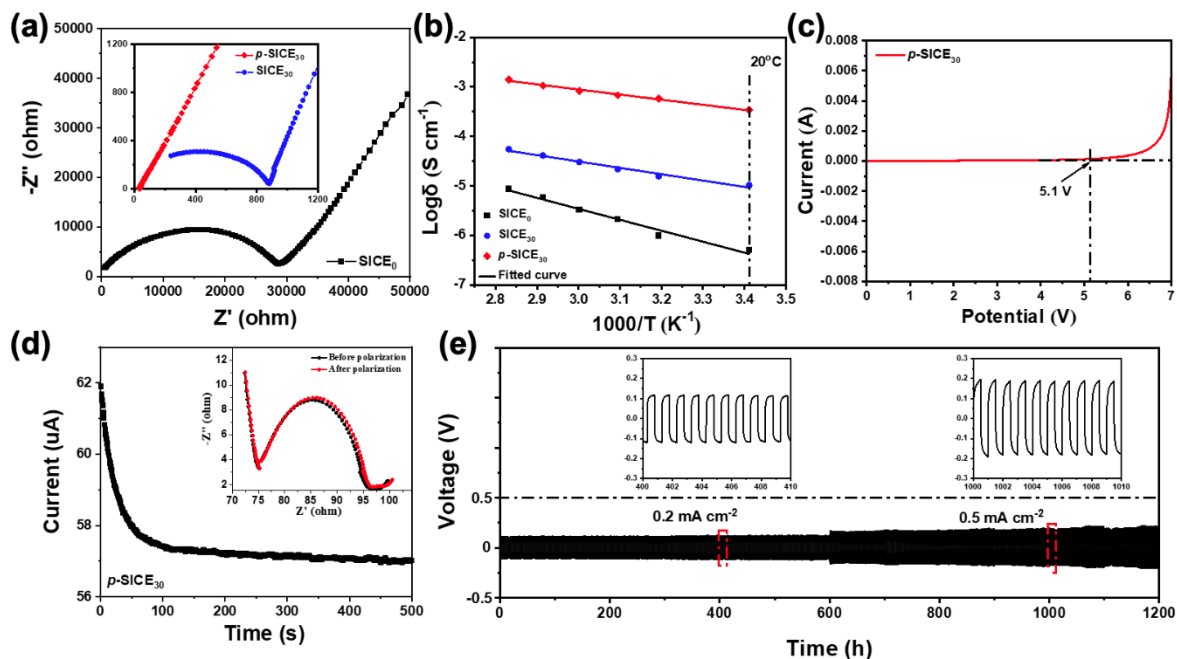


Figure 4.9. (a) EIS profiles and (b) Arrhenius plots of SICE₀, SICE₃₀ and p-SICE₃₀; (c) linear sweep voltammetry curves of p-SICE₃₀ membrane at room temperature; (d) time-dependent response of DC polarization curve for the Li|p-SICE₃₀|Li symmetric cell (inset is the EIS plots before and after polarization) at 60 °C; (e) lithium plating/stripping cycles of symmetric Li|p-SICE₃₀|Li cell at different current densities under room temperature.

Table 4.2. Electrochemical properties of SICE₀, SICE₃₀ and p-SICE₃₀.

SICE samples	s@LLAZO content (%)	TEGDME Content (%)	Ionic conductivities (S cm ⁻¹)	E _a (eV)	T _g (°C)
SICE ₀	0	0	5.05×10 ⁻⁷	0.44	-22.5
SICE ₃₀	30	0	1.03×10 ⁻⁵	0.25	-39.2
p-SICE ₃₀	30	40	3.43×10 ⁻⁴	0.20	-74.6

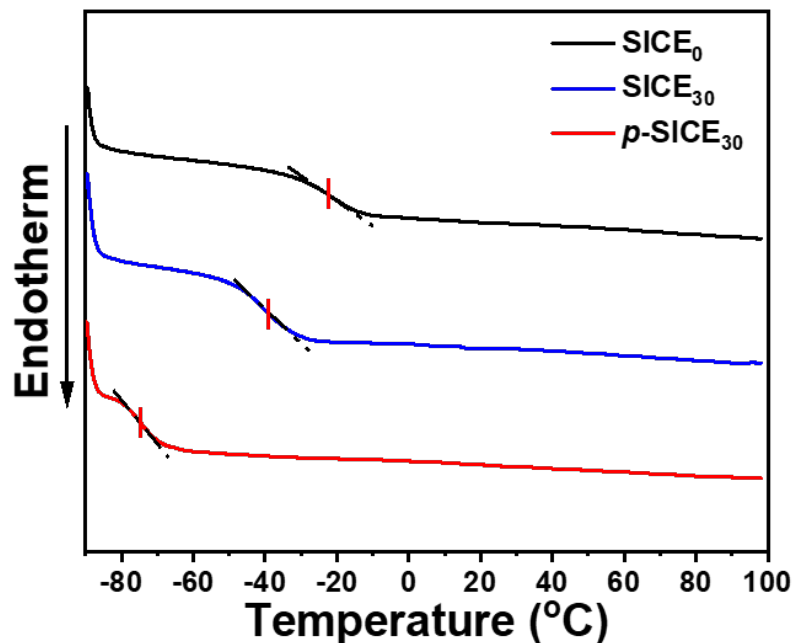


Figure 4.10. DSC curves tested from -80 to 100 °C of SICE₀, SICE₃₀ and p-SICE₃₀ membranes.

Moreover, linear sweep voltammetry (LSV) curve of p-SICE₃₀ (**Figure 4.9c**) tested by sandwiching the electrolyte discs between lithium metal and stainless steel illustrated an excellent anodic stability observed with no obvious anodic current change until the potential reached 5.1 V vs. Li⁺/Li, demonstrating the absence of electrochemically oxidized decomposition of the electrolyte. [61] In addition, as shown in **Figure 4.11**, a wide stability window was observed for p-SICE₃₀, which is favorable for advanced lithium metal batteries. **Figure 4.9d** illustrates the lithium-ion transference number (t_{Li^+}) of p-SICE₃₀ determined by Bruce's equation by combining the results of chronoamperometry and electrochemical impedance spectroscopy (EIS) testing at 60 °C (**Table 4.3**). [206] As a result of covalently immobilized 4-styrenesulfonyl (trifluoromethylsulfonyl) imide (STFSI⁻) to the polymer chain (**Figure 4.4**), p-SICE₃₀ possessed a superior t_{Li^+} up to 0.87, indicating an excellent single

lithium-ion conducting behavior, which can help to eliminate the concentration polarization effect and protect the lithium metal anode from dendrite formation, thereby improving the battery performance of all-solid-state LMBs.

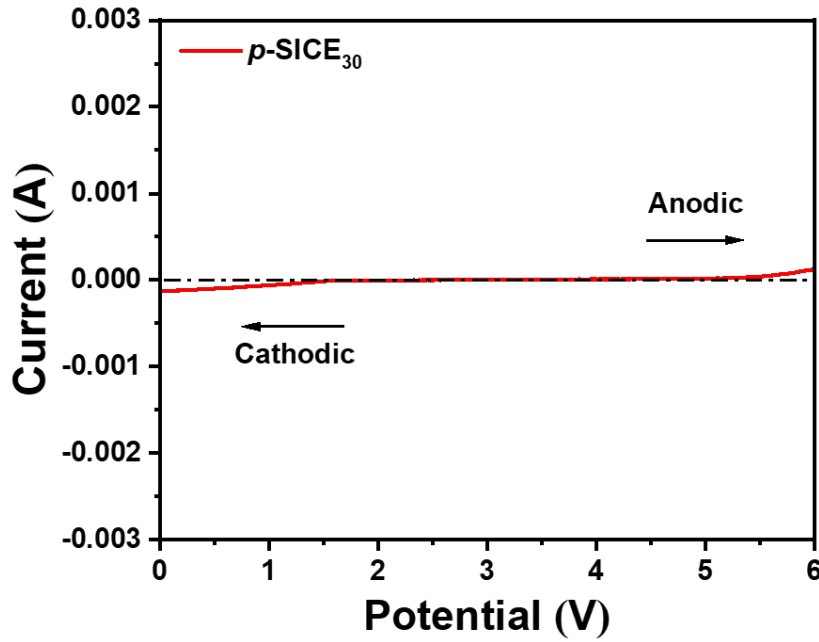


Figure 4.11. LSV curve of Li|p-SICE₃₀|stainless steel cell at room temperature.

Table 4.3. The data summary and calculated lithium-ion transference number of p-SICE₃₀ at 60 °C.

SICE samples	$R_{i,0}$ (Ω)	$R_{i,ss}$ (Ω)	I_0 (μA)	I_{ss} (μA)	t_{Li^+}
p-SICE ₃₀	96.12	97.30	61.90	57.45	0.87

The electrochemical stability of p-SICE₃₀ against Li metal was investigated by galvanostatic tests of Li|p-SICE₃₀|Li symmetric cell. As shown in **Figure 4.9e**, the test was conducted by Li⁺ stripping/plating cycling for 30 min under different current densities of 0.2 and 0.5 mA cm⁻² to evaluate its long-term lithium cycling stability and dynamic interfacial compatibility. It is notable that an extremely stable overpotential of 117 mV can be obtained at a current density of 0.2 mA cm⁻², after which it increased to 183 mV with a higher current density of 0.5 mA cm⁻². The whole test was running up to 1200 h without any short circuit, demonstrating a high interfacial stability between p-SICE₃₀ and the electrodes, namely, superior electrochemical stability against Li metal during cycling. [211, 212]

4.3.3 High performance of all-solid-state Li-metal batteries

As illustrated in **Figure 4.12a** and **Figure 4.13**, the fabricated p-SICE₃₀ membrane was easily punched into discs with a thickness of just 62 μm with uniformly distributed s@LLAZO NFs. The digital images in **Figure 4.14** further demonstrated that the resultant membrane could be bent and twisted without breakage or cracking. Therefore, in addition to improved mechanical strength, p-SICE₃₀ membrane also possessed excellent mechanical flexibility for use in advanced LMBs. Later, the well-controlled p-SICE₃₀ discs were used as the electrolyte at room temperature for all-solid-state Li-metal cells with LFP as the cathode and Li metal as the anode. The assembled cells were charged and discharged at a current density of 0.2 C (1 C = 170 mAh g⁻¹). To better understand the improved cycling performance by employing the designed electrolyte, the cell prepared by placing PP separator (Celgard, LLC) and soaking with commercial liquid electrolyte (1 M LiPF₆ in (1:1 vol) EC/DMC) was cycled at the same situation. As shown in **Figure 4.12b**, the Li|p-SICE₃₀|LFP cell exhibited an initial discharge

capacity of 148 mAh g⁻¹ with a Coulombic efficiency of 97% due to the formation of solid-electrolyte interface (SEI), after which it increased and maintained at 99.9%. The discharge capacity exhibited slightly increasing trend through the initial cycling stage, which is a result of the improved interfacial contact as charging/discharging proceeded. After 300 cycles, the cell could remain at 146 mAh g⁻¹ with a high capacity retention of 98.6% (0.67% capacity decay per cycle), indicating an outstanding long-term stability with good reversibility in redox reactions upon cycling. In comparison, although the discharge capacity of the Li|LiPF₆|LFP cell increased to 160 mAh g⁻¹ at initial cycles, it dropped sharply to 81 mAh g⁻¹ after 300 cycles, corresponding to a retention rate of 60.4%. This huge capacity fading was probably due to the unstable interfacial contact between the liquid electrolyte and Li metal associated with the formation of Li dendrites in liquid electrolyte. **Figures 4.12c and d** present the charge-discharge curves of 1st, 150th and 300th cycles for solid-state Li|p-SICE₃₀|LFP and liquid-state Li|LiPF₆|LFP cells, respectively. The results suggested that the overpotential of the Li|p-SICE₃₀|LFP cell (**Figures 4.12c**) decreased from 0.3 V (1st cycle) to 0.12 V (150th cycle) owing to an initial decrease in electrode-electrolyte interfacial resistance. The overpotential maintained the same until the 300th cycle, indicating a stable interfacial contact upon cycling. [213] However, the Li|LiPF₆|LFP (**Figures 4.12d**) cell exhibited a continuously changing overpotential of 0.29 V, 0.18 V and 0.37 V at the 1st, 150th and 300th cycles, respectively, leading to an unstable compatibility between liquid electrolyte against Li metal probably due to the dendrite growth.

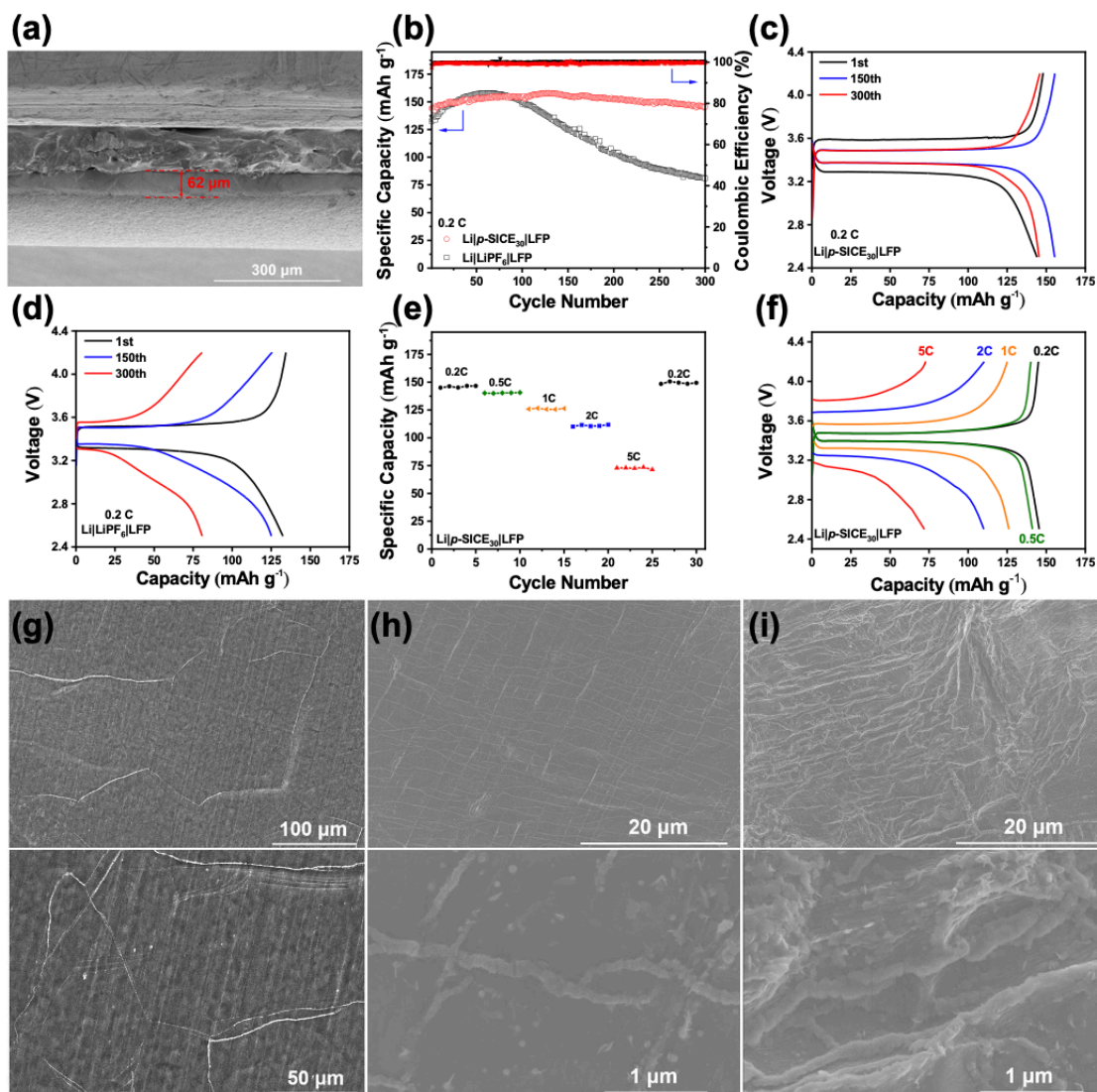


Figure 4.12. (a) SEM image of the cross-section of p-SICE₃₀ membrane; (b) cycling performance at current density of 0.2 C of all-solid-state Li|p-SICE₃₀|LFP and liquid-state Li|LiPF₆|LFP cells operated at room temperature; (c) and (d) charge–discharge curves of 1st, 150th and 300th cycles of all-solid-state Li|p-SICE₃₀|LFP and liquid-state Li|LiPF₆|LFP cells at current density of 0.2 C; (e) rate capability and (f) charge-discharge profiles (0.2-5 C) of all-solid-state Li|p-SICE₃₀|LFP cell operated at room temperature; SEM images of (g) fresh Li metal surface, (h) Li metal surface after 300-cycling in all-solid-state Li|p-SICE₃₀|LFP cell and (i) Li metal surface after 300-cycling in liquid-state Li|LiPF₆|LFP cell.

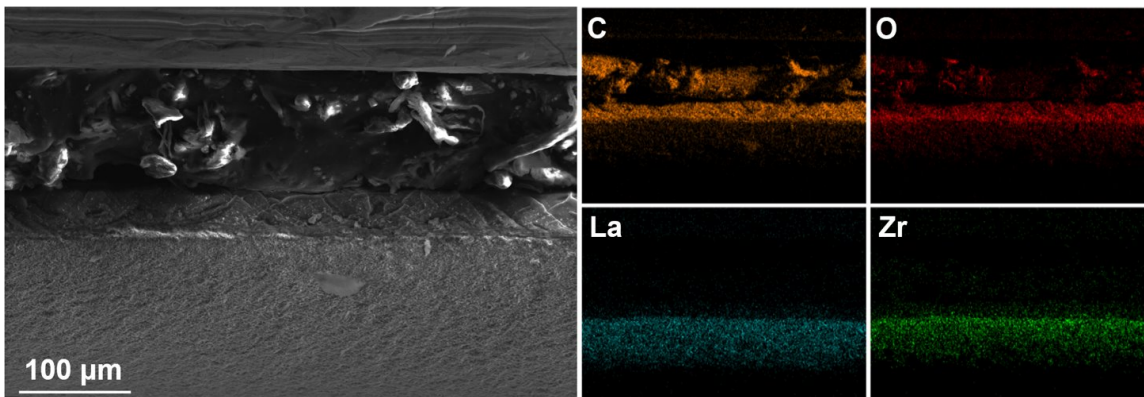


Figure 4.13. SEM image of the cross-section of p-SICE₃₀ membrane and EDAX mapping of C, O, La, and Zr elements.



Figure 4.14. Digital images of p-SICE₃₀ membrane.

The rate capability of the solid-state cell with p-SICE₃₀ membrane was studied and is presented in **Figure 4.12e and f**. The discharge capacities obtained at increasing rates of 0.2, 0.5, 1, 2 and

5 C were 145, 140, 126, 110 and 73 mAh g⁻¹, respectively, after which, upon return to 0.2 C, the discharge capacity returned to the initial value of 148 mAh g⁻¹ (**Figure 4.12e**). Notably, stable charge and discharge plateaus between 3.65 V and 3.25 V were found at the C rates from 0.2 to 2 (**Figure 4.12f**), corresponding to typical lithium ion extraction/insertion from and into the LFP cathode. [64] This outstanding rate performance bodes well for all-solid-state Li metal batteries and can be attributed to the high ionic conductivity and excellent lithium-ion transference number from the well-percolated single-ion conducting organic-inorganic structure. Meanwhile, the surface morphologies of Li metal before and after battery cycling were characterized by SEM to evaluate the Li dendrite formation and shown in **Figure 4.12g-i**. **Figure 4.12g** is the fresh Li metal before cycling, after which the majority of Li electrode surface in Li|p-SICE₃₀|LFP cell was smooth with slightly observable dendrite formation, while the surface of the Li electrode in Li|LiPF₆|LFP cell was wrinkled and covered with Li dendrites. Therefore, the results indicated that p-SICE₃₀ exhibited sufficient mechanical strength owing to the well-designed 3D organic-inorganic network, further suppressing lithium dendrites for better and long cycling performance.

4.4 Conclusions

Plasticized single-ion conducting composite polymer electrolyte was designed and fabricated with silane-modified LLAZO ceramic fillers. The delocalized anions were covalently bonded as side chains on the polymeric backbone of the polymer matrix, which led to a superior lithium-ion transference number. The s@LLAZO NFs enabled direct monomer grafting with polymer matrix, resulting in a controlled formation of an organic-inorganic network that improved the filler content and distribution with enhanced filler-matrix interaction in the SICE system. The resultant electrolyte exhibited a high ionic conductivity (3.43×10^{-4} S cm⁻¹) under room

temperature, reduced activation energy (0.20 eV) and glass transition temperature (-74.6 °C), and excellent oxidation stability (5.1 V). These improvements are beneficial from the well-percolated amorphous region in the polymer system and extra Li ion conductive pathways in ceramic structure due to the added plasticizer and LLAZO NFs. Most importantly, all-solid-state Li-metal batteries assembled with the fabricated SICE demonstrated stable cycling performance for 300 cycles and remarkably rate capability up to 5 C at room temperature owing to the improved electrochemical stability with the utilization of fast Li⁺ conductors (LLAZO) in the composite structure. In short, this novel and straightforward single-ion conducting composite polymer electrolyte has great potential in the development of advanced all-solid-state Li-metal batteries.

CHAPTER 5: Garnet-type Composite Polymer Electrolyte for Room-Temperature All-Solid-State Li-S Battery

Abstract

Lithium-sulfur batteries are considered as one of the most promising rechargeable energy storage systems due to their extremely high theoretical specific capacity and large energy density. However, the commercialization of Li-S batteries is hindered due to long-chain polysulfides diffusion and Li dendrite formation when using organic liquid electrolytes. To address these problems, a $\text{Li}_{6.28}\text{La}_3\text{Al}_{0.24}\text{Zr}_{12}\text{O}_{12}$ nanofiber (LLAZO NF) reinforced composite polymer electrolyte with superior ionic conductivity was designed and fabricated by introducing a garnet nanofiber filler into the PEO-based polymer system. The well-percolated organic-inorganic network provided fast and continuous Li ion conductive pathway with high lithium-ion transference number. The addition of LLAZO NFs not only endows the composite polymer electrolyte good electrochemical stability and improved mechanical property to suppress the Li dendrite formation, but also help to mitigate the polysulfides diffusion during cycling. Therefore, the all-solid-state Li-S battery based on this garnet-type composite polymer electrolyte shows improved cycling stability and good rate performance at room temperature.

5.1 Introduction

The development of safe, low-cost, high-energy-density and long-lasting rechargeable batteries is highly required for electric vehicles and large-scale stationary energy storage. [253, 254]

Intercalation-type Li ion batteries (LIBs), first introduced into the commercial market by Sony in the early 1990s, are currently considered the most significant achievement for electrochemical energy storage technologies owing to their relatively high energy density, high operating voltage, and long cycle life. [11] However, conventional LIBs with using Li transition-metal oxide cathodes and graphite anodes can only deliver a specific capacity approximate 250 mAh g^{-1} , which is far from satisfying the ever-growing requirement for higher energy density due to the limitation of the intercalation mechanism. [235] Therefore, it is urgent to explore other advanced cathode materials to further increase the energy density and overcome the limitations. [255-259]

Lithium-sulfur (Li-S) batteries, regarded as one of the most promising candidates, can theoretically deliver a high capacity of 1670 mAh g^{-1} and energy density of 2600 Wh kg^{-1} by using sulfur as the cathode active material and Li metal as the anode active material. [148, 232, 234, 260-262] In addition, the element sulfur is low-cost, environmentally benign, nontoxic and abundant in earth's crust. [263, 264]

Despite its considerable advantages, the practical application and commercialization of Li-S batteries have been hindered by multiple fundamental problems and technological challenges. [265, 266] The element S (ca. $10^{-30} \text{ S cm}^{-1}$ at $25 \text{ }^\circ\text{C}$) and its discharge product Li_2S (ca. $10^{-13} \text{ S cm}^{-1}$ at $25 \text{ }^\circ\text{C}$) are highly electrically and ionically insulating, thus S must maintain intimate contact with adequate electrically conductive additive to enable a reversible electrochemical reaction. [262, 267] Besides, the electrochemical mechanism based in Li-S battery is different as the intercalation-type mechanism and is more complex than that of other conversion reactions.

[268, 269] The overall electrochemical reaction of the discharge process on the S cathode can be briefly described by a single equation of $S_8 + 16Li \leftrightarrow 8Li_2S$, while the transformation from S to final discharge product Li_2S involves a series of complicated stepwise reactions with two plateaus. [265, 270] At the higher plateau of approximate 2.4 V, S is first reduced to long/middle-length-chain polysulfides (PSs, Li_2S_n , $4 \leq n \leq 8$), which are highly soluble in the polar organic solvents used in liquid electrolytes. [269, 271] At the second plateau region, the soluble PSs can penetrate the separator and migrate to the Li metal anode side and further be reduced into short-chain PSs (Li_2S_2/Li_2S), which are insoluble and tend to precipitate on the lithium metal surface and passivate the anode, leading to both active material loss and increased interfacial impedance. [269, 272-276] This phenomenon is called “shuttle effect” and usually causes severe capacity degradation on the repeated discharging/charging process, which is one of the most critical problems reducing electrochemical performance and cycle stability of Li-S batteries. [251, 259, 277-279] Another serious problem that the Li-S batteries encounter is originated from the usage of lithium metal as the anode, where the growth of dendritic Li is hazardous and can lead to internal short circuit and thermal runaway of the battery upon cycling. [224]

In order to address the aforementioned issues and improve the electrochemical performance of Li-S batteries, tremendous efforts and strategies have been studied and employed, including sulfur host material and cathode structure design, polar binders addition, separator modification, interlayer fabrication, and solid-state electrolyte adoption, etc. [259, 268, 280-285] The recent developments in solid-state electrolyte provide a promising way to restrain the PS shuttle effect and suppress Li dendrite formation for better Li-S battery performance, among which composite polymer electrolytes (CPEs) by introducing inorganic fillers into polymer matrix can not only possess high ionic conductivity but also maintain excellent interfacial contact between the

electrode and electrolyte. [8, 240] In addition, CPEs also exhibit several benign characteristics such as better thermal, chemical and electrochemical stability and outstanding mechanical strength for practical applications. [235] As for the different types of inorganic additives, garnet-type ceramic $\text{Li}_7\text{La}_3\text{Zr}_2\text{O}_{12}$ (LLZO) has been demonstrated to be one of the most promising Li ion conductors owing to its particularly high ionic conductivity (10^{-3} to 10^{-4} S cm^{-1}), superior interfacial stability with Li metal, large electrochemical window, excellent compatibility with the redox range of sulfur and high affinity to polysulfides, offering a great opportunity for solid-state Li-S batteries. [85, 106, 182, 236-240, 242, 243]

In this work, a garnet-type CPE was designed and fabricated for all-solid-state Li-S batteries to mitigate the shuttle effect of long-chain PSs and suppress the growth of dendrite Li. Herein, one-dimensional $\text{Li}_{6.28}\text{La}_3\text{Al}_{0.24}\text{Zr}_2\text{O}_{12}$ nanofiber (LLAZO NF) fillers with high surface area and excellent ionic conductivity were made by electrospinning, followed with calcination at high temperature in air environment. Later, LLAZO NF-reinforced CPE was manufactured by introducing the inorganic fillers into highly ionic-conductive crosslinked poly(ethylene glycol) (PEG)-based polymer system with using LiTFSI as the Li ion source and tetraethylene glycol dimethyl ether (TEGDME) as the plasticizer. The resulting CPE can provide a superior ionic conductivity of 5.71×10^{-4} S cm^{-1} at room temperature owing to the highly conductive inorganic three-dimensional network and well-crosslinked polymer matrix, providing continuous Li^+ conductive channels within the electrolyte system. [240] In addition, a high lithium-ion transference number (t_{Li^+}) of up to 0.70 can be obtained for the CPEs, which was attributed to the strong Lewis acid-base interaction between LLAZO NFs and Li salt, restricting the delocalized anions and further promoting Li^+ mobility. [182] Moreover, compact electrode-electrolyte interfaces were generated by directly coating CPE precursor solution on the surface of S cathode

and Li metal. Owing to these improvements, the all-solid-state Li-S battery prototype based on this garnet-type composite polymer electrolyte showed improved cycling ability at room temperature.

5.2 Experimental Section

5.2.1 Materials

Lithium nitrate (LiNO_3), zirconium butoxide solution ($\text{Zr}(\text{OCH}_2\text{CH}_2\text{CH}_2\text{CH}_3)_4$), aluminum nitrate nonahydrate ($\text{Al}(\text{NO}_3)_3 \cdot 9\text{H}_2\text{O}$), 80 wt.% in ethanol), N,N-dimethylformamide (DMF), acetic acid ($\text{CH}_3\text{CO}_2\text{H}$), polyvinylpyrrolidone (PVP, $M_w=1,300,000$), bis(trifluoromethane)sulfonimide lithium salts (LiTFSI), tetraethylene glycol dimethyl ether (TEGDME), 1-hydroxycyclohexyl phenyl ketone (HPK), poly(ethylene glycol) diacrylate (PEGDA, $M_w=700$), poly(ethylene glycol) methyl ether acrylate (PEGMEA, $M_w=360$) and N-methyl-2-pyrrolidone (NMP) were purchased from Sigma-Aldrich. Lanthanum nitrate hexahydrate ($\text{La}(\text{NO}_3)_3 \cdot 6\text{H}_2\text{O}$) was purchased from Alfa-Aesar. All chemicals were used as received without further purification.

5.2.2 Fabrication of $\text{Li}_{6.28}\text{La}_3\text{Al}_{0.24}\text{Zr}_2\text{O}_{12}$ nanofibers

The electrospinning precursor solution was first prepared by dissolving stoichiometric amounts of 9.42 mmol of LiNO_3 , 4.5 mmol of $\text{La}(\text{NO}_3)_3 \cdot 6\text{H}_2\text{O}$, 3 mmol of $\text{Zr}(\text{OCH}_2\text{CH}_2\text{CH}_2\text{CH}_3)_4$ and 0.36 mmol of $\text{Al}(\text{NO}_3)_3 \cdot 9\text{H}_2\text{O}$ in a mixed solvent composed of 16 ml DMF and 4 ml acetic acid. Excess LiNO_3 (15 wt%) was added to compensate for lithium loss during the subsequent calcination procedure. Then 2 g of PVP was added after stirring the mixed solution for 30 min. The precursor solution was mechanically stirred overnight. Electrospinning was conducted at a high voltage of 10 kV with a feeding rate of 0.45 ml h^{-1} . The as-spun nanofibers were later

calcined at 850 °C for 2 h in air environment to obtain LLAZO nanofibers (LLAZO NFs). The calcinated LLAZO were further stored at vacuum oven at 160 °C for future use.

5.2.3 Preparation of LLAZO incorporated composite polymer electrolytes

The composite polymer electrolytes (CPEs) were simply prepared by one-pot free radical polymerization employing HPK as the UV initiator in a glovebox. PEGDA, PEGMEA and LiTFSI solution with a molar ratio of [EO] and [Li⁺] fixed at 12:1 was designed as the crosslinking polymer system for CPE fabrication. Herein, a polymer solution of 96 wt.% PEGMEA and 4 wt.% PEGDA was mixed with 0.4 wt.% HPK, after which 140 mg LiTFSI/TEGDME, ionic liquid solution in equimolar amounts, was added to prepare the precursor solution matrix. Different amount of LLAZO NFs based on the weight percentage of polymer matrix from 0 to 50% was introduced and the resulting solutions were sonicated until LLAZO NFs were uniformly distributed in the solutions. The well-prepared precursor CPE solutions were cross-linked into thin films between two transparent quartz plates by exposing to UV light for 10 mins in a glovebox. The fabricated CPE membranes with different weight percentage of LLAZO NFs were denoted as CPE-x, where x = 0, 1, 2, 3, 4, or 5, corresponding to 0, 10%, 20%, 30%, 40%, or 50%, respectively.

As for CPE-coated sulfur cathode and Li metal anode preparation, the well-sonicated precursor solutions of CPE-x were directly dropping on the surface of sulfur cathode and Li metal anode. Transparent quartz plates were then placed on the top to obtain a smooth and uniform surface, followed by exposing to UV light for 15 mins in a glove box.

5.2.4 Structure characterization

Fourier transform-infrared spectroscopy (FTIR, Thermo Scientific™ Nicolet™ iS™10) was used to identify the functional groups of LLAZO NFs, PEGDA, PEGMEA and CPE-x (x=0, 1, 2, 3, 4, 5) membranes at the range of 1800~700 cm^{-1} with 32 scans and resolution of 4 cm^{-1} at room temperature. X-ray diffraction (XRD) was applied to identify the crystal structures of calcinated LLAZO NFs using a Rigaku D/Max 2400 (Japan) with Cu Ka radiation ($\lambda=1.5418 \text{ \AA}$) in a 2-Theta angle range from 10° to 50°. A universal mechanical test machine (MTS Criterion, Loading: 100 N) was also utilized to measure the mechanical properties of CPE-x (x=0, 1, 2, 3, 4, 5) membranes with a cross-head speed of 0.5 mm/min. Thermo-gravimetric analysis (TGA, Perkin Elmer Pyris 1) was used with a heating rate of 10 $^{\circ}\text{C min}^{-1}$ under nitrogen atmosphere to test the thermal property of CPE-0 and CPE-2 membranes. Differential scanning calorimetry (DSC) was carried out at a heating/cooling rate of 2 $^{\circ}\text{C min}^{-1}$ using a TA Instrument Discovery Series to measure the glass transition temperatures (T_g) of CPE-x (x=0, 1, 2, 3, 4, 5) membranes. The morphologies of LLAZO NFs, CPE-2 coated sulfur cathode and Li metal anode after cycling were characterized by field-emission scanning electron microscopy (FE-SEM, FEI Verios 460L, USA) with EDX mapping. ImageJ Software was used to measure the thickness of CPE-2 membranes.

5.2.5 Electrochemical performance evaluation

Ionic conductivities of all CPEs were determined by electrochemical impedance spectroscopy (EIS, Garmy Reference 600 device) over a frequency range of 0.1 Hz to 1 MHz with an AC potential of 10 mV. CPE membranes were pouched and sandwiched between two stainless steel

blocking electrodes for electrochemical impedance test. The ionic conductivity (δ , S cm⁻¹) was calculated by the following equation:

$$\delta = t/R_b A \quad (5.1)$$

where t is the thickness of CPE membrane, R_b the membrane bulk resistance obtained from the intercept of extended semicircle with the real axis on the Nyquist plot, and A the area of the membrane. Activation energy (E_a , eV) of CPEs was calculated with an Arrhenius plot of ionic conductivities under different temperatures by the Arrhenius equation:

$$\delta = A \exp(-E_a/RT) \quad (5.2)$$

where δ is the ionic conductivity, A the dc conductivity of pre-exponential factor, E_a the activation energy, R the molar gas constant, and T the absolute temperature.

Lithium-ion transference number (t_{Li^+}) of each CPE membrane was determined by chronoamperometry testing and electrochemical impedance spectroscopy (EIS) measurement at 60°C. A symmetric lithium cell was assembled and tested by EIS with a frequency ranging from 0.1 Hz to 1 MHz before and after polarization. Chronoamperometry was performed with an applied DC potential of 10 mV. The t_{Li^+} value was calculated by Bruce's equation:

$$t_{Li^+} = I_{ss} (\Delta V - I_0 R_{i,0}) / I_0 (\Delta V - I_{ss} R_{i,ss}) \quad (5.3)$$

where ΔV is the polarization potential, I_0 and I_{ss} the initial and steady-state currents before and after polarization, and R_0 and R_{ss} the initial and steady-state total resistances before and after polarization.

Galvanostatic cycling testing of Li|CPE|Li symmetric cells was conducted at room temperature to evaluate the structural stability of CPE membranes by sandwiching a CPE membrane (60-80 μm thickness and 1/2 inch diameter) between two Li foils (7/16 inch diameter) and cycling at current densities of 0.05, 0.1, 0.2 and 0.5 mA cm^{-2} with current direction reversed every 30 minutes.

5.2.6 Battery Performance Evaluation

All-solid-state lithium sulfur (Li-S) cells were fabricated for evaluating the performance of CPE membranes in room-temperature all-solid-state batteries. Sulfur was first mixed with carbon black (C65) in weight ratio of 1:1 and then transferred to a sealed hydrothermal kettle and heated to 155 $^{\circ}\text{C}$ for overnight to obtain the S/C composite. The sulfur cathode was prepared by mixing a slurry of S/C composite, ionic liquid solution of G_4 with LiTFSI in equimolar amounts, carbon black (C65), and polyacrylic acid (PAA) binder at a weight ratio of 7:1:1:1 in NMP solvent, which was uniformly coated on aluminum foil by a doctor blade set at 30 mm. The prepared cathode was dried under high vacuum at 60 $^{\circ}\text{C}$ overnight to remove NMP solvent. The sulfur cathode was coated with CPE precursor solution in a glovebox and then punched into disks with a diameter of 1/2 inches with an active material loading around 0.8-1 mg cm^{-2} . The Li metal cathode was coated with the same precursor solution and then punched into disks with a diameter of 9/16 inches for use. Standard LIR2032 coin cells were assembled in a glovebox by stacking coated sulfur cathode and Li anode. The cycling performance of all-solid-state Li-S cells was then tested by an Arbin battery tester in a potential range of 1.7 V to 2.8 V.

5.3 Results and Discussion

CPEs by embedding inorganic fillers into polymer matrix can both maintain the advantages of each material, such as high Li ion conductance and good mechanical rigidity of the inorganic fillers, and good interfacial contact and mechanical flexibility of the organic polymer matrix. [233] Among various inorganic fillers, garnet-type ceramic LLZO is considered to be one of the most promising Li ion conductors for all-solid-state Li batteries due to its excellent ionic conductivity (10^{-3} to 10^{-4} S cm^{-1}), large electrochemical window and superior interfacial stability with Li metal. Moreover, LLZO also possessed excellent compatibility with the redox range of sulfur and high affinity to polysulfides, which are favorable for solid-state Li-S batteries. [260] In addition to the advantaged garnet ceramic LLZO, acrylate-based PEO monomer and crosslinker were employed in this work because the atactic methacrylate backbones form interconnected “cages” that can spatially besiege the PEO molecules to decrease the degree of crystallinity of PEO, thus increasing the Li ion conductance. [286-288] As shown in **Figure 5.1**, the garnet-type CPE was fabricated by dispersing calcinated-electrospun LLAZO NFs into the polymer matrix composed of monomer poly(ethylene glycol) methyl ether acrylate (PEGMEA), crosslinker poly(ethylene glycol) diacrylate (PEGDA), bis(trifluoromethane)sulfonimide lithium salts (LiTFSI), plasticizer tetraethylene glycol dimethyl ether (TEGDME), and initiator 1-hydroxycyclohexyl phenyl ketone (HPK) before UV-initiated polymerization in a glovebox. Owing to the crosslinking polymer network and the introduction of inorganic active nanofillers, which both helped to inhibit the crystallinity of PEO, a three-dimensional (3D) inorganic-organic framework was well-created, providing continuously Li-ion conductive pathways for high conduction. Moreover, in order to maintain good interfacial contact between electrodes/electrolyte, CPE precursor solution was directly coating on the surface of S cathode

and Li metal, resulting in an interconnected interface between S cathode and electrolyte for fast Li ion transportation and compact contact between Li metal and electrolyte for Li dendrite suppression.

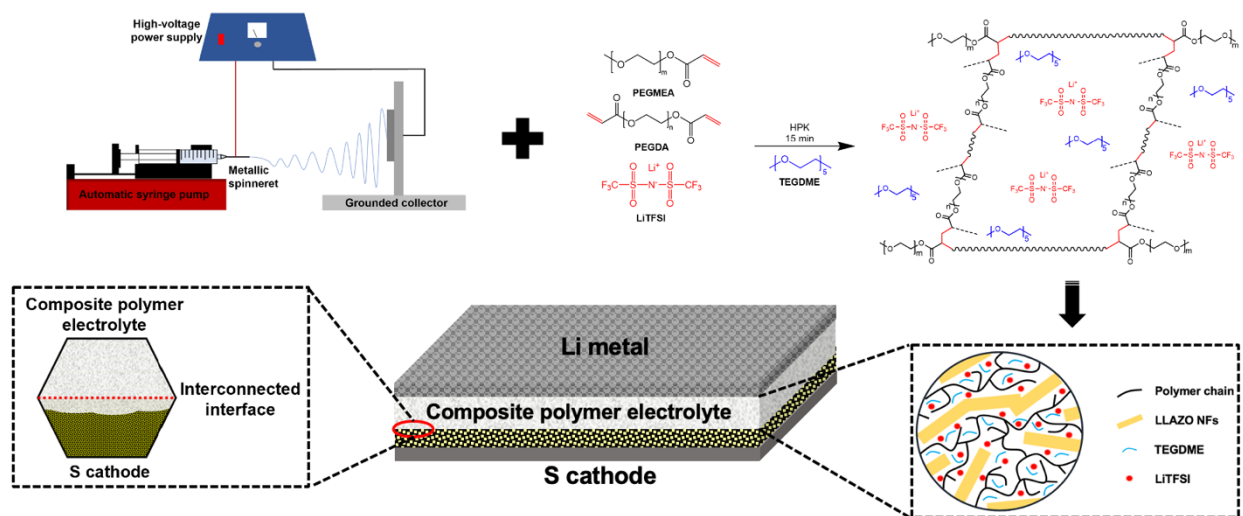


Figure 5.1. Schematic of fabrication procedure of all-solid-state Li-S battery with garnet-type CPE coated S cathode and Li anode, in which the LLAZO NFs was manufactured by electrospinning with high temperature calcination.

5.3.1 Design of LLAZO NFs-reinforced composite polymer electrolytes

As illustrated in **Figure 5.2a-b**, the morphology and crystal structure of calcined LLAZO NFs were obtained by scanning electron microscopy (SEM) image and X-ray diffraction (XRD) test, respectively. The calcined LLAZO ceramic fillers maintained well-defined nanofibrous shape with the main peaks in XRD diffraction pattern clearly indexed with the cubic LLZO crystal structure. [182] **Figure 5.3** further demonstrated the structure of LLAZO NFs with SEM image and EDAX mapping, where all elements (La, Zr, O) were uniformly distributed along the one-dimensional fiber direction. In this work, the molar ratio of $[\text{EO}]/[\text{Li}^+]$ was selected as 12:1 to the

polymer matrix with adding equimolar PEG-based plasticizer of TEGDME, approximately 17-25% based on the CPE system. The oligomer PEG molecules can not only space the long chains apart to improve the amorphous region, but also enhance the interface between inorganic fillers and organic polymer matrix. [252] Later, different contents of LLAZO NFs were introduced into the polymer matrix to obtain CPEs with improved ionic conductivity and mechanical property. The resulting CPE membranes were denoted as CPE-x, where x represents to 0, 1, 2, 3, 4, 5, corresponding to 0, 10%, 20%, 30%, 40%, 50% based on the weight of polymer matrix, respectively. **Figure 5.4a** shows the Fourier transform-infrared spectroscopy (FTIR) spectra of PEGDA, PEGMEA, LLAZO and CPE-x. All the absorption bands due to the stretching vibration of vinyl groups ($1630-1640\text{ cm}^{-1}$) and acrylate groups (1410 and 810 cm^{-1}) in PEGDA and PEGMEA disappeared in the FTIR spectra of the synthesized CPE-x, indicating that both the monomer PEGMEA and crosslinker PEGDA have reacted completely during UV-initiated polymerization. [11, 289, 290]

The ionic conductivity and EIS changing of CPEs with different contents of fillers at room temperature are presented in **Figure 5.2c and 5.4b**, respectively, and the results are summarized in **Table 5.1**. It is seen that the fabricated CPE with 20% LLAZO NFs exhibited the highest ionic conductivity of $5.71 \times 10^{-4}\text{ S cm}^{-1}$, before which the ionic conductivity of CPEs raised with increasing filler content due to the improved amorphous region of polymer matrix and enhanced Li ion conductive pathways. After reaching the peak, ionic conductivity decreased because of severe agglomeration effect of inorganic fillers, where LLAZO NFs were easy to form large and separated aggregates at higher concentration, resulting in discontinuous Li ion transfer channels within the CPE system. [182] In addition, **Figure 5.2d** explores the effect of LLAZO NFs on mechanical properties of CPEs and the corresponding values are summarized in **Table 5.1**. The

pristine crosslinked polymer electrolyte (CPE-0) showed a Young's modulus of 2.42 MPa, a tensile strength of 0.86 MPa, and a maximum elongation of 43.17%. With the introduction of LLAZO NFs, the mechanical properties were improved due to the high rigidity nature of inorganic ceramics, where CPE-2 possessed the optimum Young's modulus and tensile strength of 4.46 MPa and 1.87 MPa, respectively. The continuously growing elongation with increasing LLAZO NFs was probably due to the improved amorphous region, causing more free volume within the polymer network. While the Young's modulus decreased after 20% filler content addition, which may result from the agglomeration effect of inorganic fillers within the polymer matrix.

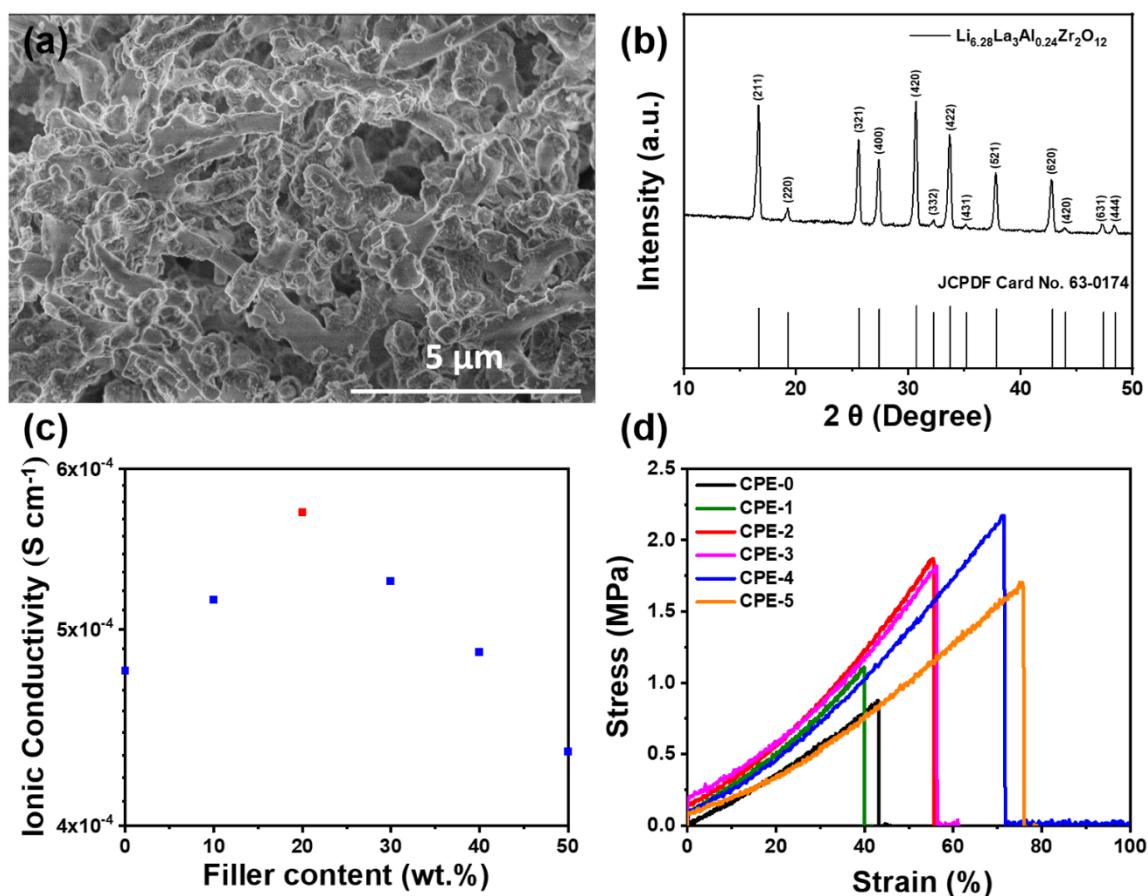


Figure 5.2. (a) SEM image and (b) XRD pattern of calcinated LLAZO NFs; (c) Ionic conductivity versus filler content and (d) Stress–strain curves of the CPEs at room temperature.

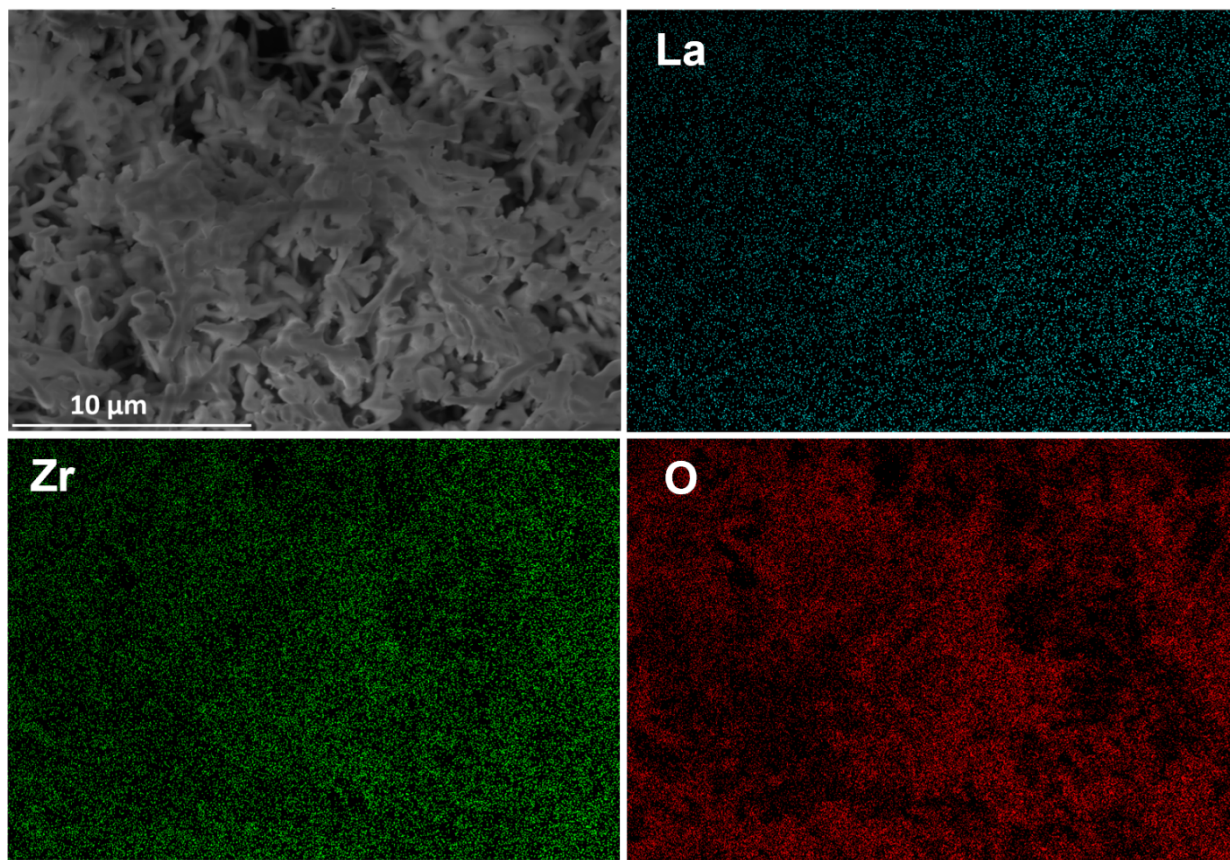


Figure 5.3. SEM image and EDAX mapping of La, Zr, O elements of LLAZO NFs.

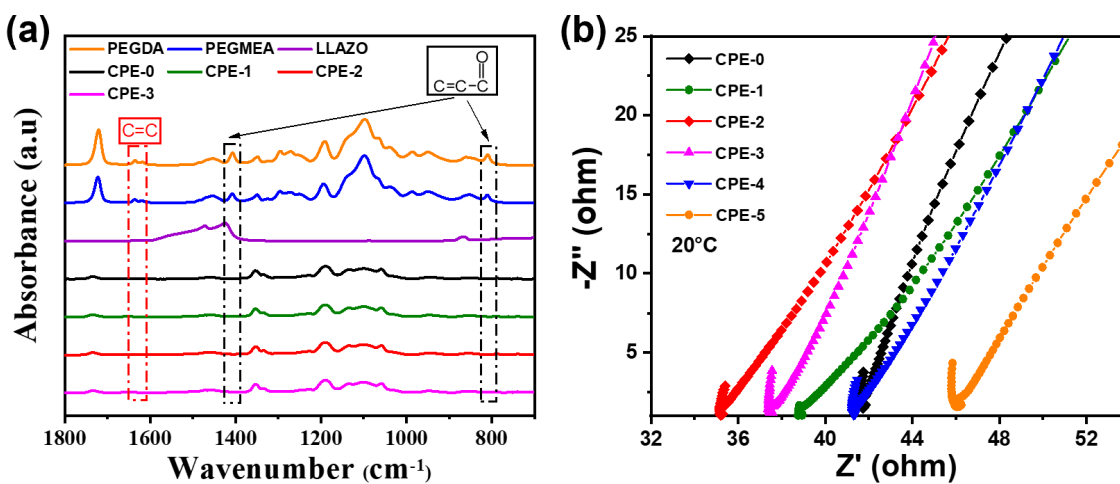


Figure 5.4. (a) FTIR spectra of PEGDA, PEGMEA, LLAZO NFs and CPE-x with different content fillers; (b) EIS profiles of CPE-x with different content fillers at room temperature.

Table 5.1 Ionic conductivities and mechanical properties of CPEs with different LLAZO contents at room temperature.

CPE samples	LLAZO content (%)	Ionic conductivities (S cm ⁻¹)	Young's modulus (MPa)	Tensile strength (MPa)	Elongation (%)
CPE-0	0	4.77×10^{-4}	2.42	0.86	43.17
CPE-1	10	5.17×10^{-4}	3.46	1.11	39.97
CPE-2	20	5.71×10^{-4}	4.46	1.87	55.61
CPE-3	30	5.28×10^{-4}	3.98	1.82	56.29
CPE-4	40	4.87×10^{-4}	3.72	2.17	71.55
CPE-5	50	4.35×10^{-4}	2.74	1.70	75.93

5.3.2 Electrochemical performance characterization of LLAZO NFs-reinforced composite polymer electrolytes

The electrochemical performance of the CPEs with different LLAZO contents is shown in **Figure 5.5** and **Table 5.2**. **Figure 5.5a** illustrates the Arrhenius plots of their ionic conductivities tested under different temperatures, where all ionic conductivity-temperature curves obey the classical Arrhenius linear relationship within the testing temperature range (20 ~ 80 °C). The calculated activation energy of bare polymer electrolyte is 0.291 eV, which declines to 0.268 eV with addition of LLAZO NFs for CPE-2, indicating a lower energy barrier in transporting lithium cations within the polymer system. This was attributed from the well-organized three-dimensional inorganic-organic framework, where Li ions preferred to be conducted by

interconnected fibrous garnet phase. [14, 58] When the filler content exceeded 20%, Li ions were mostly conducted by the segmental motion of polymer chains due to the highly aggregated LLAZO phase with discontinuous Li ion conduction. [211, 246] Afterwards, the differential scanning calorimetry (DSC) curves in **Figure 5.5b** indicated that the glass transition temperature of CPE-2 (-71.46 °C) is lower than that of pristine polymer electrolyte (-69.62 °C), demonstrating that the inorganic ceramic LLAZO NFs are beneficial to increase the amorphous region of the polymer network. Moreover, the lithium ion transference number (t_{Li^+}) values were determined by Bruce's equation using the obtained initial current (I_0), steady-state current (I_{ss}) via chronoamperometry and the corresponding impedances at two states via EIS testing at 60 °C (see **Figure 5.5c** and **Figure 5.6**) [206] As shown in **Table 5.3**, due to the strong Lewis acid-base interaction between LLAZO NFs and Li salts, which restrains the anions mobility and further promotes Li cations migration, [182] all CPEs with different content of LLAZO NFs exhibited higher t_{Li^+} values in contrast with pristine polymer electrolyte (0.31). CPE-2 shows the highest t_{Li^+} value of up to 0.70, which may attribute from its relatively more uniform LLAZO NF distribution within the polymer system. **Figure 5.5d** illustrates the linear sweep voltammetry (LSV) curve of CPE-2 tested by sandwiching the electrolyte disc between lithium metal and stainless steel. The CPE-2 membrane exhibited excellent electrochemical window with no obvious current change until the potential reaches 4.6 V vs. Li^+/Li , indicating the absence of electrochemically oxidized decomposition of the electrolyte and superior electrochemical stability which is favorable for Li-S battery application. [61]

In addition to electrochemical properties, **Figure 5.7** investigates the thermal stability of CPE-2 and bare polymer electrolyte by thermo-gravimetric analysis (TGA), where both electrolytes showed good thermal property and stay stable up to 110 °C, after which only 10% weight loss

was observed at 150 °C, proving that they are able to maintain sufficient thermal stability under normal working temperatures for battery application. Compared to bare polymer electrolyte, the last 20% residue left for CPE-2 after 700°C should be the LLAZO NFs. Meanwhile, galvanostatic tests were conducted on Li|CPE-0|Li and Li|CPE-2|Li symmetric cells with Li⁺ stripping/plating cycling for 30 min under different current densities up to 1200 h, shown in **Figure 5.5e-f and Figure 5.8**. It is notable that symmetric cell with bare polymer electrolyte can maintain a stable overpotential of 46 mV at a current density of 0.05 mA cm⁻², after which it increased to 100 mV at a higher current density of 0.1 mA cm⁻². However, short circuiting occurred when current density kept increasing after 600-hour cycling. This may be a reason from low mechanical properties of the polymer electrolyte without ceramic fillers, which cannot endure the continuously volume changing of the Li metal during cycling and lose the compact interfacial contact with electrode, eventually resulting in unstoppable Li dendrite growth. In contrast, benefited from the improved mechanical properties and superior electrochemical stability of embedded LLAZO NFs against Li metal, [182] the Li|CPE-2|Li symmetric cell can provide stable overpotentials of 52, 96, 168 and 267 mV at current densities of 0.05 mA cm⁻², 0.1 mA cm⁻², 0.2 mA cm⁻² and 0.5 mA cm⁻², respectively, further demonstrating a high interfacial stability between CPE-2 and electrodes.

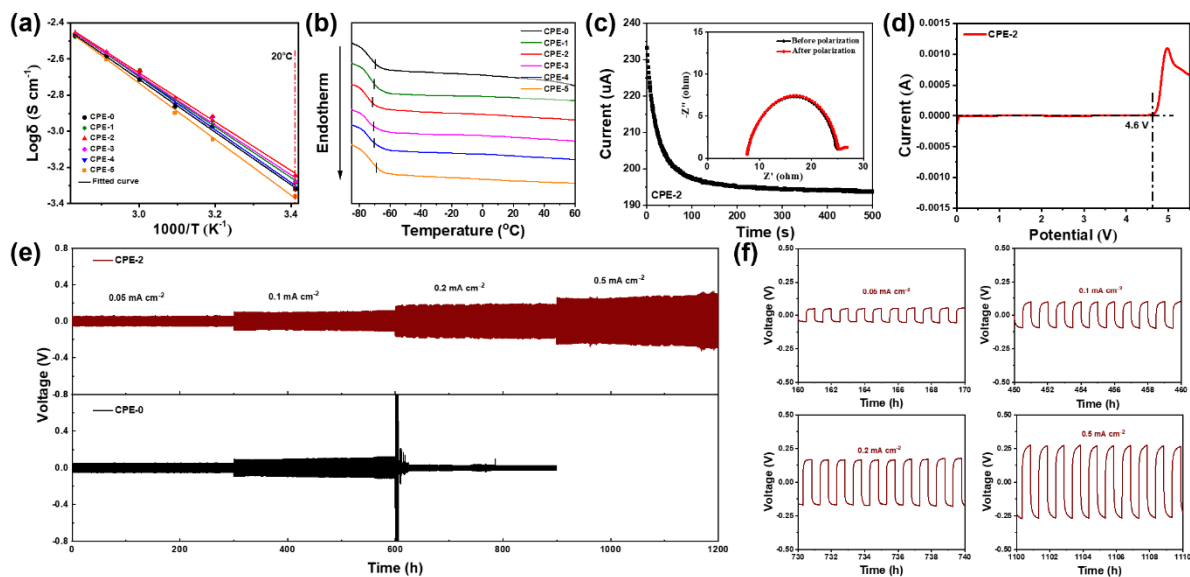


Figure 5.5. (a) Arrhenius plots and (b) DSC curves of CPE membranes; (c) time-dependent response of DC polarization curve for the Li|CPE-2|Li symmetric cell (inset is the EIS plots before and after polarization) at 60 °C; (d) linear sweep voltammetry curves of CPE-2 membrane at room temperature; (e) and (f) lithium plating/stripping cycles of symmetric Li|CPE-2|Li and Li|CPE-0|Li cells at different current densities under room temperature.

Table 5.2 Electrochemical properties of CPEs with different LLAZO contents.

CPE samples	LLAZO content (%)	E _a (eV)	T _g (°C)	t _{Li+}
CPE-0	0	0.291	-69.62	0.31
CPE-1	10	0.279	-70.35	0.52
CPE-2	20	0.268	-71.46	0.70
CPE-3	30	0.274	-70.52	0.60
CPE-4	40	0.291	-70.32	0.67
CPE-5	50	0.307	-69.01	0.62

Table 5.3 The data summary and calculated lithium-ion transference numbers of CPEs with different filler contents at 60 °C.

CPE samples	$R_{i,0}$ (Ω)	$R_{i,ss}$ (Ω)	I_0 (μA)	I_{ss} (μA)	t_{Li^+}
CPE-0	30.21	30.39	226.9	129.4	0.31
CPE-1	29.61	29.77	189.1	133.8	0.52
CPE-2	25.24	25.48	233.1	195.3	0.70
CPE-3	35.20	35.31	139.7	103.6	0.60
CPE-4	32.22	32.36	144.4	113.6	0.67
CPE-5	36.03	38.54	136.5	99.5	0.62

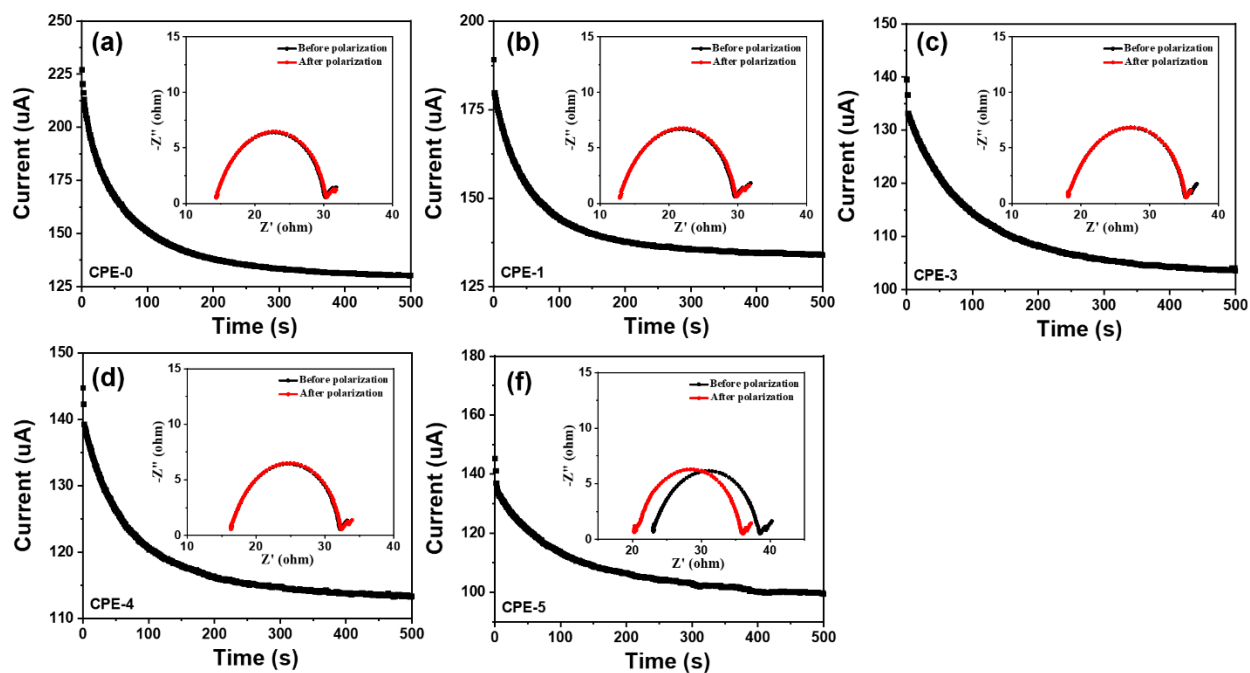


Figure 5.6. Time-dependent response of DC polarization curve for the Li|CPE-x|Li symmetric cell (inset is the EIS plots before and after polarization, and x=0, 1, 3, 4, 5) at 60 °C.

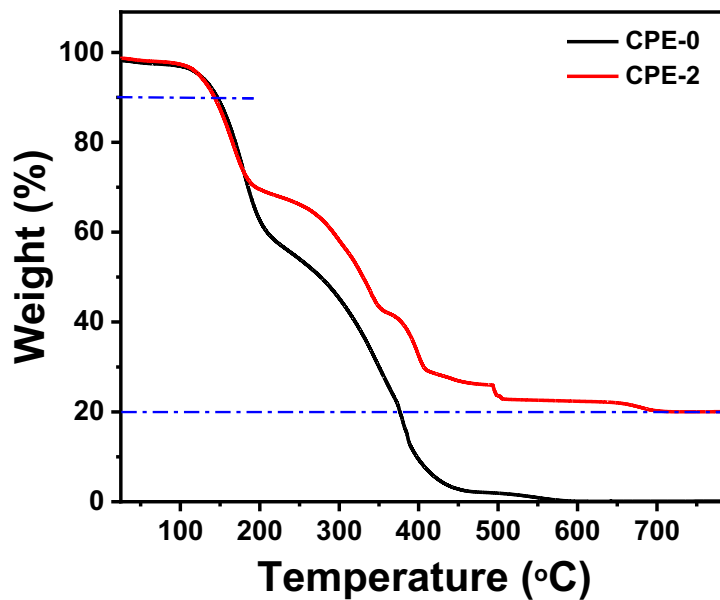


Figure 5.7. TGA curves of CPE-0 and CPE-2 from 0 to 800 °C.

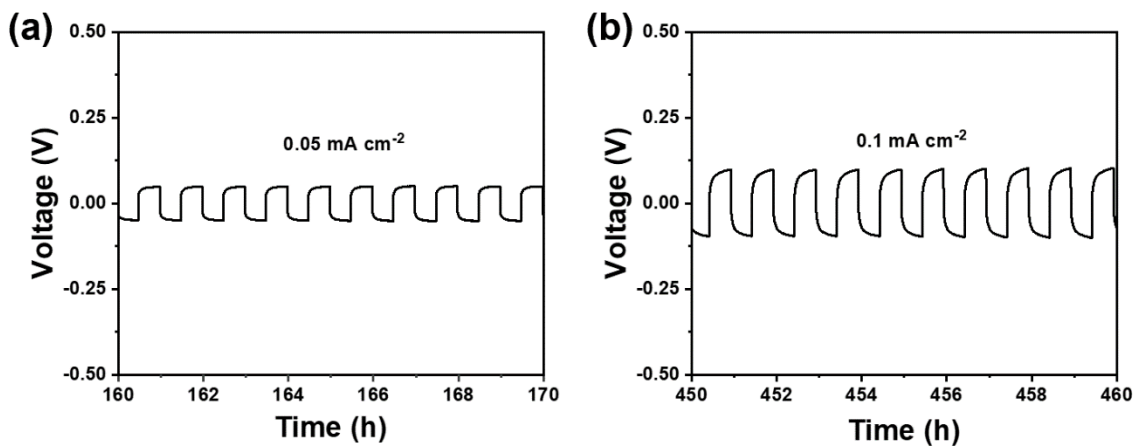


Figure 5.8. Lithium plating/stripping cycles of symmetric Li|CPE-0|Li cell at current densities of (a) 0.05 mA cm^{-2} and (b) 0.1 mA cm^{-2} under room temperature.

5.3.3 Battery performance evaluation of all-solid-state Li-S batteries

All-solid-state batteries were assembled with the LLAZO NF-embedded CPEs as the electrolyte, S as the cathode and Li metal as the anode. As shown in **Figure 5.9a**, the original surface of the S cathode was rough and covered by small cracks. In order to maintain good interfacial contact between S cathode and electrolyte, CPE-2 precursor solution was directly coated on the surface of S cathode by UV-initiated polymerization (**Figure 5.9b**), after which the surface turned much smoother without any breakage, further providing a stable surface environment for battery assembly. In addition, Li anode was also coated with the same CPE precursor solution to both improve the interfacial stability and thus protect Li metal from dendrite growth. **Figure 5.10a and b** show the SEM images of the cross-section of CPE-2 coated S cathode and Li anode. It is seen that thin coating layers with thicknesses of 20 and 25 μm were obtained on the cathode and anode, respectively. To mention, the S cathode used here for SEM and EDAX mapping test did not contain any LiTFSI/TEGDME solution and LLAZO NFs, which means no F and Zr should appear within the bulk structure of the cathode. The F and Zr elements mapping shown in **Figure 5.11** was the EDAX test of the SEM image in **Figure 5.10a**, which indicates that the precursor solution penetrated inside the cathode structure through the cracks on the surface mentioned above, building an interconnect interface network for continuous Li ion transfer between the cathode and electrolyte.

Room-temperature cycling performance of the assembled cells with CPE-0 and CPE-2 running at a current density of 0.1 C (1 C=1675 mAh g⁻¹) is shown in **Figure 5.10c**. Both Li-S cells show low Coulombic efficiencies at the first cycle, which are 83% for Li|CPE-0|S cell and 90% for Li|CPE-2|S cell. This is a result of polysulfides formation and diffusion out from the cathode initially, after which their Coulombic efficiencies increase and keep staying around 98.95% and

99.80% for CPE-0 and CPE-2, respectively. For Li|CPE-0|S cell, it can deliver an initial discharge capacity of 881 mAh g⁻¹, while the capacity continuously descended to 247 mAh g⁻¹ with a capacity retention of only 28% eventually. In contrast, an initial discharge capacity of 968 mAh g⁻¹ can be obtained by the cell with CPE-2 owing to the improved Li ion conductive pathway for higher ionic conductivity, which ends up at 591 mAh g⁻¹ after 100 cycles. The capacity retention for Li|CPE-2|S cell is 61%, much higher than that of Li|CPE-0|S cell due to the introduction of LLAZO NFs, which not only increased the physical barriers for polysulfides migration and mitigated the trend of capacity fading, but also improved the mechanical strength and suppressed the Li dendrite growth upon cycling. **Figure 5.10d** presents the charge-discharge curves of different cycles of the Li|CPE-2|S cell. It is seen that the typical charge-discharge profile is similar to PEO-based solid-state Li-S batteries with two plateaus corresponded to the multistep redox reactions of sulfur to long-chain polysulfides (Li₂S_n, 4 ≤ n ≤ 8) at 2.4-2.1 V and then low-order Li₂S at 2.1-1.7 V, [235, 291] and the two plateaus maintained until 100 cycles. As a control group shown in **Figure 5.12**, the charge-discharge curves for Li|CPE-0|S cell are out of the shape and fluctuating, indicating a poor oxidation stability of the pristine polymer electrolyte without LLAZO NFs. [291] Afterward, the rate capability of CPE-2 electrolyte was further studied by testing the assembled Li|CPE-2|S cell under different current densities. As shown in **Figure 5.10e**, discharge capacities of 1211, 915, 758 and 556 mAh g⁻¹ were obtained at increasing current densities of 0.05, 0.1, 0.2 and 0.5 C, respectively. It is notable that a capacity of 422 mAh g⁻¹ can still be delivered at a high current density of 1C, after which, upon return to 0.05 C, the discharge capacity mostly returned to the initial value of 1150 mAh g⁻¹, which is promising for high-current-density battery cycling application.

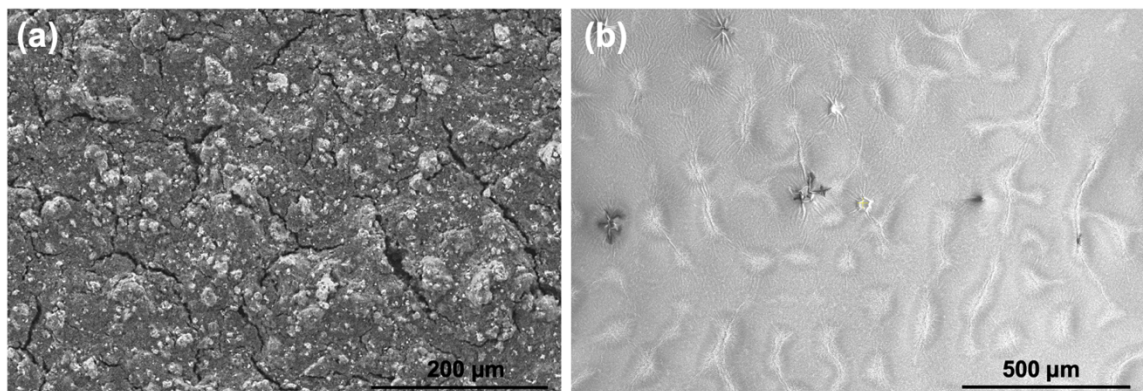


Figure 5.9. SEM images of the surface morphologies of (a) S cathode and (b) CPE-2 coated S cathode.

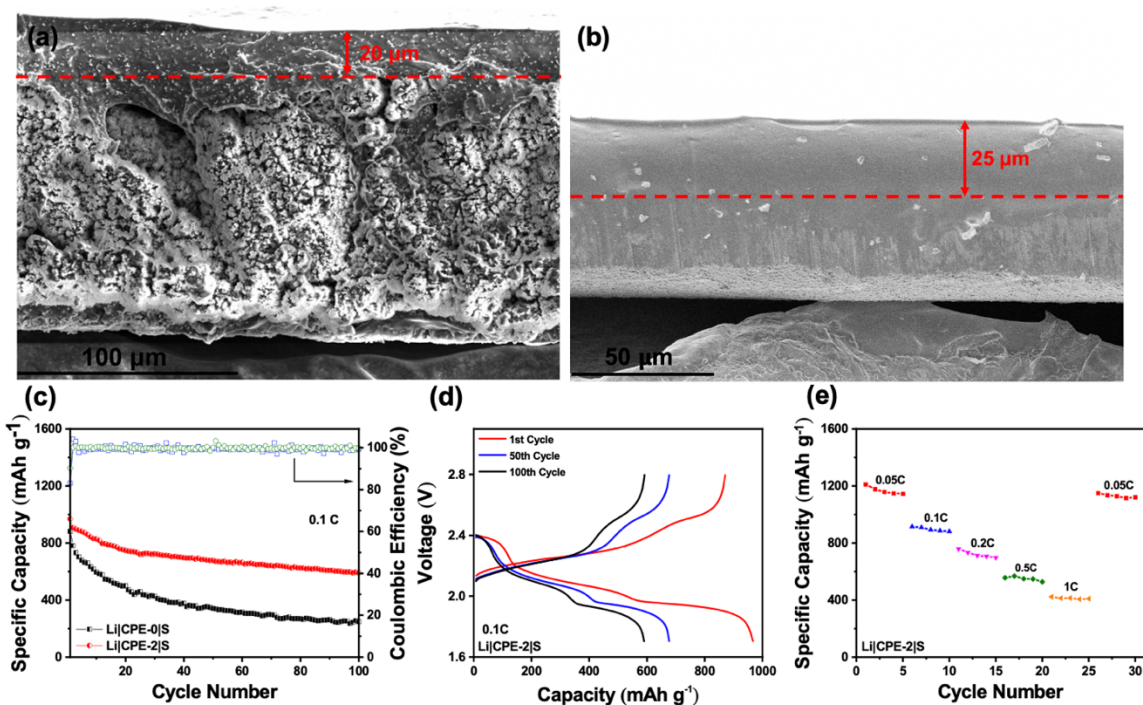


Figure 5.10. SEM images of the cross-section of (a) CPE-2 coated S cathode and (b) CPE-2 coated Li metal anode; (c) cycling performance at current density of 0.1 C of all-solid-state Li|CPE-0|S and Li|CPE-2|S cells operated at room temperature; (d) charge–discharge curves of 1st, 50th and 100th cycles of all-solid-state Li|CPE-2|S cell at current density of 0.1 C; (e) Rate capability (0.05–1 C) of all-solid-state Li|CPE-2|S cell operated at room temperature.

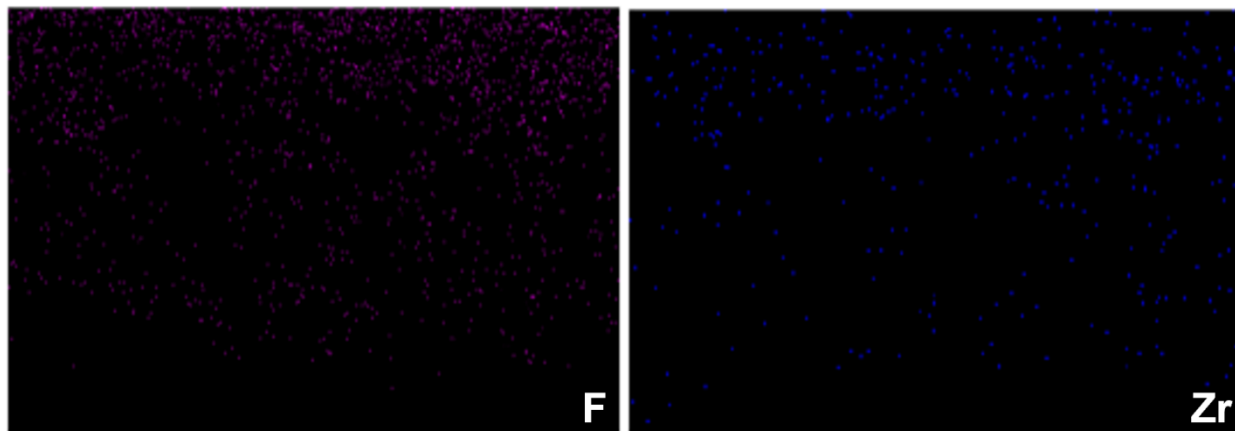


Figure 5.11. The EDAX mapping of F, Zr elements of CPE-2 coated S cathode of the SEM image on Figure 4(a), the S cathode used here did not contain any LiTFSI/ TEGDME solution and LLAZO NFs.

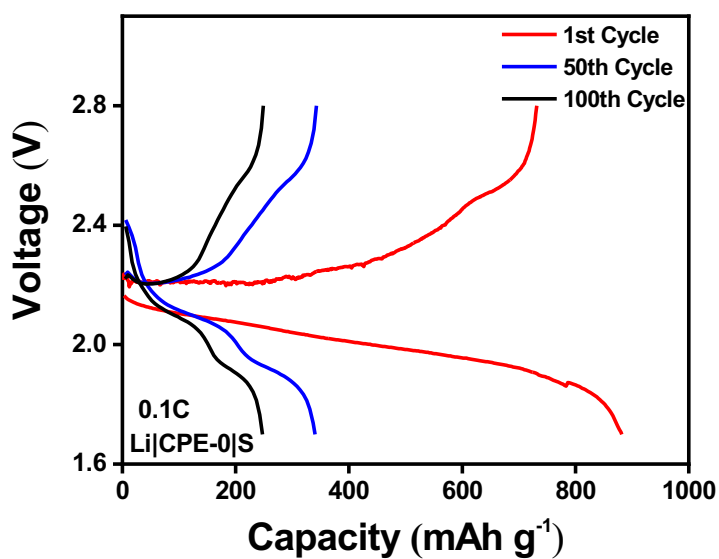


Figure 5.12. Charge–discharge curves of 1st, 50th and 100th cycles of all-solid-state Li|CPE-0|S cell at current density of 0.1 C.

After cycling, the SEM was applied to observe the surface morphologies of Li metal to evaluate the Li dendrite formation and shown in **Figure 5.13**. **Figure 5.13a** is the fresh Li metal before

cycling, and the Li electrode surface after cycling in Li|CPE-0|S cell shown in **Figure 5.13b** was fully covered with Li dendrites. In contrast, the majority of the Li anode surface in Li|CPE-2|S cell was smooth with slightly observable dendrite formation, which indicates that CPE-2 membrane exhibited sufficient mechanical strength owing to the LLAZO NFs reinforced well-crosslinked polymer network, further suppressing lithium dendrites for better and long cycling performance. Meanwhile, the SEM and EDAX mapping (**Figure 5.14**) were used to detect the polysulfide migration to Li metal anode. Since lithium salt of LiTFSI, which contains S element, was employed in CPE membranes fabrication and later directly coated on Li anode surface, an uncycled Li metal anode from Li|CPE-0|S cell with EDAX mapping of S element shown in **Figure 5.14a and b** were used as the control group, where the S element on its surface is from LiTFSI. **Figure 5.14c and e** are the SEM images of Li metal anodes running after 100 cycles from Li|CPE-0|S and Li|CPE-2|S cells, respectively. It is obviously that cycled Li metal via using bare polymer electrolyte lost the surface morphology because plenty of Li dendrites formed and polysulfide aggregates diffused from cathode and remained on the anode surface, which was also confirmed at the EDAX mapping of S element (**Figure 5.14d**) marked by red circles. On the contrary, the surface of the cycled Li anode from Li|CPE-2|S cell remained relatively clear and smooth with less detected S element (**Figure 5.14f**), demonstrating that the introduced LLAZO NFs can help restrain the polysulfide migration and reduce the Li dendrite formation for better cycling performance.

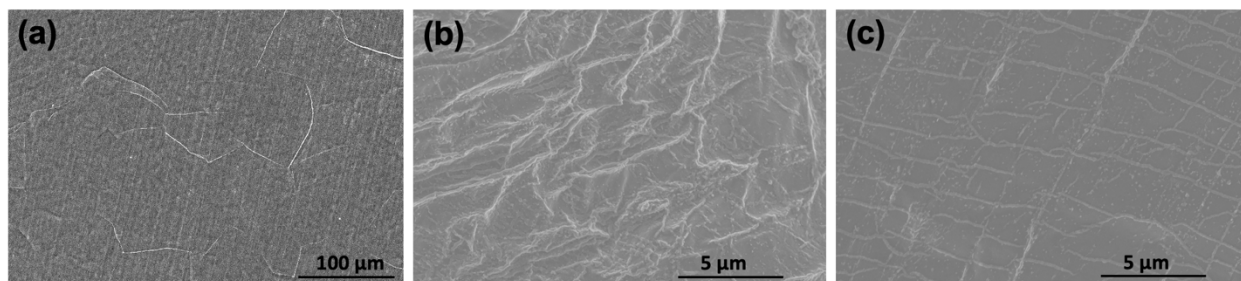


Figure 5.13. SEM images of (a) fresh Li metal surface, (b) Li metal surface after 100-cycling in all-solid-state Li|CPE-0|S cell and (c) Li metal surface after 100-cycling in all-solid-state Li|CPE-2|S cell.

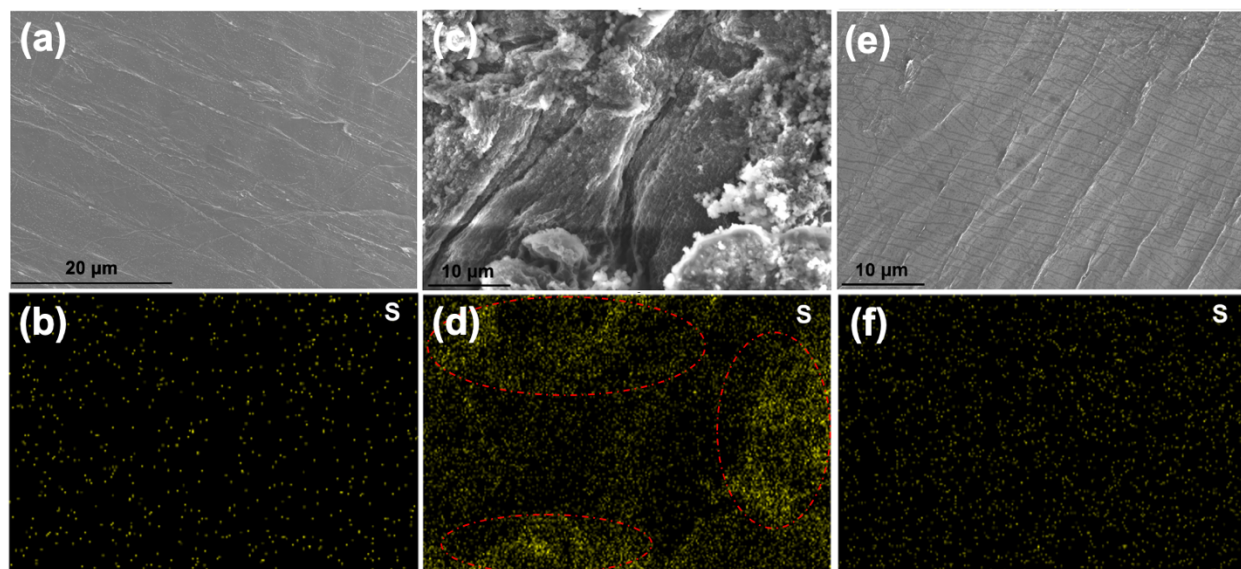


Figure 5.14. (a) SEM image of uncycled Li metal anode from Li|CPE-0|S cell with (b) EDAX mapping of S element; (c) SEM image of cycled Li metal anode from Li|CPE-0|S cell with (d) EDAX mapping of S element; (e) SEM image of cycled Li metal anode from Li|CPE-2|S cell with (f) EDAX mapping of S element.

5.4 Conclusions

A garnet-type composite polymer electrolyte (CPE) was designed and directly coated on both S cathode and Li metal anode for assembling all-solid-state Li-S batteries. One-dimensional nanofibrous shaped LLAZO fillers with high surface area and excellent ionic conductivity were made by electrospinning, followed with calcination at high temperature in air environment. The LLAZO NFs reinforced CPE exhibits well-fabricated organic-inorganic network with a superior ionic conductivity of $5.71 \times 10^{-4} \text{ S cm}^{-1}$ at room temperature and improved mechanical properties. The introduction of LLAZO NFs can not only increase the amorphous region of crosslinked polymer matrix, but also offer continuous Li^+ conductive channels within the inorganic 3D structure, decreasing the activation energy to 0.268 eV. In addition, a high lithium-ion transference number (t_{Li^+}) up to 0.70 can be obtained for the CPE attributed to the strong Lewis acid-base interaction between LLAZO NFs and Li salt, restricting the delocalized anions and further promoting Li^+ mobility. Interconnected compact contact were created at cathode/electrolyte and anode/electrolyte interfaces, respectively, by coating and then polymerization, which enhanced the interfacial stability and reduced the interfacial impedance. Moreover, the LLAZO reinforced CPE was able to mitigate the polysulfides diffusion and suppress the Li dendrite formation during cycling. Owing to these improvements, the all-solid-state Li-S battery prototype based on this garnet-type composite polymer electrolyte shows improved cycling stability up to 100 cycles and good rate performance at room temperature.

CHAPTER 6: Recommended Future Work

Cathode design:

Because of the high specific energy capacity and density, low cost and eco-friendliness, Li-S battery has been regarded as one of the most promising next-generation batteries in the realm of energy storage. Thus, extensive research has shifted to Li-S battery to satisfy the rapidly growing demands for portable electronic devices, electric vehicles, and grid-energy storage systems.

However, the commercialization of Li-S battery is still hindered due to the relatively low attainable energy density, short cycling life and insufficient mass loading. The cathodes of Li-S batteries have been extensively researched and their structural design is important on maximizing the synergetic effects to enhance the electrochemical performance of Li-S batteries. The future work on sulfur cathode design should focus on improving the distribution, content and mass loading of the active materials with high electronic/ionic conductivity. In addition, functional framework such as electrospun nanostructure materials and carbon-based nano-compounds with tunable specific surface area and excellent surface functionalization can be applied to restrain polysulfides migration as well as to buffer the volume change between sulfur and its final reduction product Li_2S during the cycling process to further increase the active materials utilization and power density of Li-S batteries.

Solid electrolyte:

Besides sulfur cathode, the electrolyte in Li-S battery also greatly influences the electrochemical reaction rate, the polarization potential as well as the utilization of sulfur. Intensive efforts have been taken on the study of all-solid-state Li-S battery due to the severe safety concern, lithium

dendrite formation, and polysulfides dissolution caused by using organic liquid electrolytes. To improve the viability of solid electrolyte in advanced all-solid-state Li-S battery, various requirements should be satisfied in solid electrolyte design, such as high ionic conductivity, excellent interface compatibility between electrodes/electrolyte, wide electrochemical window, and robust mechanical properties. Inorganic solid electrolyte usually possesses a high ionic conductivity for superior fast Li ions conductive pathways but brittle mechanical property and worse interfacial contact between electrode/electrolyte. In contrast, organic polymer electrolyte exhibits good mechanical strength and flexibility for lithium dendrites suppression but low ionic conductivity. Thus, composite solid polymer electrolyte integrating inorganic and organic solid compounds, such as the electrospun inorganic LLTO nanofibers embedded in PEO matrix, has been considered as one of the most potential ways to achieving the high rate, high capacity, and long cycles of the Li-S battery for practical applications.

REFERENCES

- [1] H. Zhang, C. Li, M. Piszcz, E. Coya, T. Rojo, L.M. Rodriguez-Martinez, M. Armand, Z. Zhou, Single lithium-ion conducting solid polymer electrolytes: advances and perspectives, *Chemical Society Reviews* 46(3) (2017) 797-815.
- [2] X.-B. Cheng, C.-Z. Zhao, Y.-X. Yao, H. Liu, Q. Zhang, Recent advances in energy chemistry between solid-state electrolyte and safe lithium-metal anodes, *Chem* 5(1) (2019) 74-96.
- [3] Z. Cheng, T. Liu, B. Zhao, F. Shen, H. Jin, X. Han, Recent advances in organic-inorganic composite solid electrolytes for all-solid-state lithium batteries, *Energy Storage Materials* (2020).
- [4] D. Zhou, A. Tkacheva, X. Tang, B. Sun, D. Shanmukaraj, P. Li, F. Zhang, M. Armand, G. Wang, Stable conversion chemistry-based lithium metal batteries enabled by hierarchical multifunctional polymer electrolytes with near-single ion conduction, *Angewandte Chemie* 131(18) (2019) 6062-6067.
- [5] X. Ren, S. Chen, H. Lee, D. Mei, M.H. Engelhard, S.D. Burton, W. Zhao, J. Zheng, Q. Li, M.S. Ding, Localized high-concentration sulfone electrolytes for high-efficiency lithium-metal batteries, *Chem* 4(8) (2018) 1877-1892.
- [6] C. Sun, J. Liu, Y. Gong, D.P. Wilkinson, J. Zhang, Recent advances in all-solid-state rechargeable lithium batteries, *Nano Energy* 33 (2017) 363-386.
- [7] G. Xi, M. Xiao, S. Wang, D. Han, Y. Li, Y. Meng, Polymer-Based Solid Electrolytes: Material Selection, Design, and Application, *Advanced Functional Materials* 31(9) (2021) 2007598.
- [8] C. Yan, P. Zhu, H. Jia, J. Zhu, R.K. Selvan, Y. Li, X. Dong, Z. Du, I. Angunawela, N. Wu, High-performance 3-D fiber network composite electrolyte enabled with Li-ion conducting

- nanofibers and amorphous PEO-based cross-linked polymer for ambient all-solid-state lithium-metal batteries, *Advanced Fiber Materials* 1(1) (2019) 46-60.
- [9] C. Li, B. Qin, Y. Zhang, A. Varzi, S. Passerini, J. Wang, J. Dong, D. Zeng, Z. Liu, H. Cheng, Single-ion conducting electrolyte based on electrospun nanofibers for high-performance lithium batteries, *Advanced Energy Materials* 9(10) (2019) 1803422.
- [10] A. Manthiram, X. Yu, S. Wang, Lithium battery chemistries enabled by solid-state electrolytes, *Nature Reviews Materials* 2(4) (2017) 1-16.
- [11] H. Cheng, C. Yan, R. Orenstein, M. Dirican, S. Wei, N. Subjaleandee, X. Zhang, Polyacrylonitrile Nanofiber-Reinforced Flexible Single-Ion Conducting Polymer Electrolyte for High-Performance, Room-Temperature All-Solid-State Li-Metal Batteries, *Advanced Fiber Materials* (2022) 1-15.
- [12] X. Shen, H. Hua, H. Li, R. Li, T. Hu, D. Wu, P. Zhang, J. Zhao, Synthesis and molecular dynamic simulation of a novel single ion conducting gel polymer electrolyte for lithium-ion batteries, *Polymer* 201 (2020) 122568.
- [13] Y. Zhang, J. Wang, C. Tan, Y. He, Y. Chen, S. Huo, D. Zeng, C. Li, H. Cheng, Fire-retardant sp³ boron-based single ion conducting polymer electrolyte for safe, high efficiency and dendrite-free Li-metal batteries, *Journal of Membrane Science* 620 (2021) 118921.
- [14] N. Meng, X. Zhu, F. Lian, Particles in composite polymer electrolyte for solid-state lithium batteries: A review, *Particuology* 60 (2022) 14-36.
- [15] I. Villaluenga, K.H. Wujcik, W. Tong, D. Devaux, D.H. Wong, J.M. DeSimone, N.P. Balsara, Compliant glass-polymer hybrid single ion-conducting electrolytes for lithium batteries, *Proceedings of the National Academy of Sciences* 113(1) (2016) 52-57.

- [16] L. Fan, S. Wei, S. Li, Q. Li, Y. Lu, Recent progress of the solid-state electrolytes for high-energy metal-based batteries, *Advanced Energy Materials* 8(11) (2018) 1702657.
- [17] M. Dirican, C. Yan, P. Zhu, X. Zhang, Composite solid electrolytes for all-solid-state lithium batteries, *Materials Science and Engineering: R: Reports* 136 (2019) 27-46.
- [18] D. Fenton, Complexes of alkali metal ions with poly (ethylene oxide), *polymer* 14 (1973) 589.
- [19] P.V. Wright, Electrical conductivity in ionic complexes of poly (ethylene oxide), *British polymer journal* 7(5) (1975) 319-327.
- [20] C. Berthier, W. Gorecki, M. Minier, M. Armand, J. Chabagno, P. Rigaud, Microscopic investigation of ionic conductivity in alkali metal salts-poly (ethylene oxide) adducts, *Solid State Ionics* 11(1) (1983) 91-95.
- [21] F. Croce, G. Appetecchi, L. Persi, B. Scrosati, Nanocomposite polymer electrolytes for lithium batteries, *Nature* 394(6692) (1998) 456-458.
- [22] L. Long, S. Wang, M. Xiao, Y. Meng, Polymer electrolytes for lithium polymer batteries, *Journal of Materials Chemistry A* 4(26) (2016) 10038-10069.
- [23] N. Karan, D. Pradhan, R. Thomas, B. Natesan, R. Katiyar, Solid polymer electrolytes based on polyethylene oxide and lithium trifluoro-methane sulfonate (PEO–LiCF₃SO₃): Ionic conductivity and dielectric relaxation, *Solid State Ionics* 179(19-20) (2008) 689-696.
- [24] S. Ramesh, A. Arof, Ionic conductivity studies of plasticized poly (vinyl chloride) polymer electrolytes, *Materials Science and Engineering: B* 85(1) (2001) 11-15.
- [25] W. Gorecki, M. Jeannin, E. Belorizky, C. Roux, M. Armand, Physical properties of solid polymer electrolyte PEO (LiTFSI) complexes, *Journal of Physics: Condensed Matter* 7(34) (1995) 6823.

- [26] H. Xie, Z. Tang, Z. Li, Y. He, Y. Liu, H. Wang, PVDF-HFP composite polymer electrolyte with excellent electrochemical properties for Li-ion batteries, *Journal of Solid State Electrochemistry* 12(11) (2008) 1497-1502.
- [27] P. Jayathilaka, M. Dissanayake, I. Albinsson, B.-E. Mellander, Dielectric relaxation, ionic conductivity and thermal studies of the gel polymer electrolyte system PAN/EC/PC/LiTFSI, *Solid State Ionics* 156(1-2) (2003) 179-195.
- [28] S. Das, A. Ghosh, Effect of plasticizers on ionic conductivity and dielectric relaxation of PEO-LiClO₄ polymer electrolyte, *Electrochimica Acta* 171 (2015) 59-65.
- [29] J. Newman, K.E. Thomas-Alyea, *Electrochemical systems*, John Wiley & Sons 2012.
- [30] M. Doyle, T.F. Fuller, J. Newman, The importance of the lithium ion transference number in lithium/polymer cells, *Electrochimica Acta* 39(13) (1994) 2073-2081.
- [31] N. Kamaya, K. Homma, Y. Yamakawa, M. Hirayama, R. Kanno, M. Yonemura, T. Kamiyama, Y. Kato, S. Hama, K. Kawamoto, A lithium superionic conductor, *Nature materials* 10(9) (2011) 682-686.
- [32] R. Bouchet, S. Maria, R. Meziane, A. Aboulaich, L. Lienafa, J.-P. Bonnet, T.N. Phan, D. Bertin, D. Gigmes, D. Devaux, Single-ion BAB triblock copolymers as highly efficient electrolytes for lithium-metal batteries, *Nature materials* 12(5) (2013) 452-457.
- [33] H.G. Buss, S.Y. Chan, N.A. Lynd, B.D. McCloskey, Nonaqueous polyelectrolyte solutions as liquid electrolytes with high lithium ion transference number and conductivity, *ACS Energy Letters* 2(2) (2017) 481-487.
- [34] M. Ue, Mobility and ionic association of lithium and quaternary ammonium salts in propylene carbonate and γ -butyrolactone, *Journal of the electrochemical society* 141(12) (1994) 3336.

- [35] H.B. Youcef, B. Orayech, J.M.L. Del Amo, F. Bonilla, D. Shanmukaraj, M. Armand, Functionalized cellulose as quasi single-ion conductors in polymer electrolyte for all-solid-state Li/Na and LiS batteries, *Solid State Ionics* 345 (2020) 115168.
- [36] K.D. Fong, J. Self, K.M. Diederichsen, B.M. Wood, B.D. McCloskey, K.A. Persson, Ion transport and the true transference number in nonaqueous polyelectrolyte solutions for lithium ion batteries, *ACS central science* 5(7) (2019) 1250-1260.
- [37] K.M. Diederichsen, E.J. McShane, B.D. McCloskey, Promising routes to a high Li⁺ transference number electrolyte for lithium ion batteries, *ACS Energy Letters* 2(11) (2017) 2563-2575.
- [38] L. Li, M. Wang, J. Wang, F. Ye, S. Wang, Y. Xu, J. Liu, G. Xu, Y. Zhang, Y. Zhang, Asymmetric gel polymer electrolyte with high lithium ion conductivity for dendrite-free lithium metal batteries, *Journal of Materials Chemistry A* 8(16) (2020) 8033-8040.
- [39] J.-N. Chazalviel, Electrochemical aspects of the generation of ramified metallic electrodeposits, *Physical review A* 42(12) (1990) 7355.
- [40] P.Y. Ji, J. Fang, Y.Y. Zhang, P. Zhang, J.B. Zhao, Novel Single Lithium-Ion Conducting Polymer Electrolyte Based on Poly (hexafluorobutyl methacrylate-co-lithium allyl sulfonate) for Lithium-Ion Batteries, *ChemElectroChem* 4(9) (2017) 2352-2358.
- [41] Z. Shao, P. Jannasch, Single lithium-ion conducting poly (tetrafluorostyrene sulfonate)-polyether block copolymer electrolytes, *Polymer Chemistry* 8(4) (2017) 785-794.
- [42] D. Benrabah, S. Sylla, J.-Y. Sanchez, M. Armand, Cationic conductivity in poly (oxyethylene oxide) networks, *Journal of power sources* 54(2) (1995) 456-460.
- [43] D. Benrabah, S. Sylla, F. Alloin, J.-Y. Sanchez, M. Armand, Perfluorosulfonate-polyether based single ion conductors, *Electrochimica acta* 40(13-14) (1995) 2259-2264.

- [44] E. Tsuchida, H. Ohno, N. Kobayashi, H. Ishizaka, Poly [(*t*-carboxy) oligo (oxyethylene) methacrylate] as a new type of polymeric solid electrolyte for alkali-metal ion transport, *Macromolecules* 22(4) (1989) 1771-1775.
- [45] M. Zhang, S. Yu, Y. Mai, S. Zhang, Y. Zhou, A single-ion conducting hyperbranched polymer as a high performance solid-state electrolyte for lithium ion batteries, *Chemical Communications* 55(47) (2019) 6715-6718.
- [46] J. Zhu, Z. Zhang, S. Zhao, A.S. Westover, I. Belharouak, P.F. Cao, Single-Ion Conducting Polymer Electrolytes for Solid-State Lithium–Metal Batteries: Design, Performance, and Challenges, *Advanced Energy Materials* 11(14) (2021) 2003836.
- [47] S. Zhang, Z. Deng, G. Wan, Cationic Conductivity of Blend Complexes Composed of Poly [oligo (oxyethylene) methacrylate] and the Alkali Metal Salts of Poly (sulfoalkyl methacrylate), *Polymer journal* 23(2) (1991) 73-78.
- [48] Q. Pan, W. Zhang, M. Pan, B. Zhang, D. Zeng, Y. Sun, H. Cheng, Construction of a lithium ion transport network in cathode with lithiated bis (benzene sulfonyl) imide based single ion polymer ionomers, *Journal of Power Sources* 283 (2015) 279-288.
- [49] R. Meziane, J.-P. Bonnet, M. Courty, K. Djellab, M. Armand, Single-ion polymer electrolytes based on a delocalized polyanion for lithium batteries, *Electrochimica Acta* 57 (2011) 14-19.
- [50] R. Rohan, K. Pareek, Z. Chen, W. Cai, Y. Zhang, G. Xu, Z. Gao, H. Cheng, A high performance polysiloxane-based single ion conducting polymeric electrolyte membrane for application in lithium ion batteries, *Journal of Materials Chemistry A* 3(40) (2015) 20267-20276.
- [51] M.B. Armand, Polymer electrolytes, *Annual Review of Materials Science* 16(1) (1986) 245-261.

- [52] R.J. Klein, S. Zhang, S. Dou, B.H. Jones, R.H. Colby, J. Runt, Modeling electrode polarization in dielectric spectroscopy: Ion mobility and mobile ion concentration of single-ion polymer electrolytes, *The Journal of chemical physics* 124(14) (2006) 144903.
- [53] D. Fragiadakis, S. Dou, R.H. Colby, J. Runt, Molecular mobility, ion mobility, and mobile ion concentration in poly (ethylene oxide)-based polyurethane ionomers, *Macromolecules* 41(15) (2008) 5723-5728.
- [54] S. Inceoglu, A.A. Rojas, D. Devaux, X.C. Chen, G.M. Stone, N.P. Balsara, Morphology–conductivity relationship of single-ion-conducting block copolymer electrolytes for lithium batteries, *ACS Macro Letters* 3(6) (2014) 510-514.
- [55] S. Feng, D. Shi, F. Liu, L. Zheng, J. Nie, W. Feng, X. Huang, M. Armand, Z. Zhou, Single lithium-ion conducting polymer electrolytes based on poly [(4-styrenesulfonyl)(trifluoromethanesulfonyl) imide] anions, *Electrochimica Acta* 93 (2013) 254-263.
- [56] Q. Ma, H. Zhang, C. Zhou, L. Zheng, P. Cheng, J. Nie, W. Feng, Y.S. Hu, H. Li, X. Huang, Single lithium-ion conducting polymer electrolytes based on a super-delocalized polyanion, *Angewandte Chemie International Edition* 55(7) (2016) 2521-2525.
- [57] W.H. Meyer, Polymer electrolytes for lithium-ion batteries, *Advanced materials* 10(6) (1998) 439-448.
- [58] R. Tan, R. Gao, Y. Zhao, M. Zhang, J. Xu, J. Yang, F. Pan, Novel organic–inorganic hybrid electrolyte to enable LiFePO₄ quasi-solid-state Li-ion batteries performed highly around room temperature, *ACS applied materials & interfaces* 8(45) (2016) 31273-31280.
- [59] J. Lopez, D.G. Mackanic, Y. Cui, Z. Bao, Designing polymers for advanced battery chemistries, *Nature Reviews Materials* 4(5) (2019) 312-330.

- [60] G. Luo, B. Yuan, T. Guan, F. Cheng, W. Zhang, J. Chen, Synthesis of single lithium-ion conducting polymer electrolyte membrane for solid-state lithium metal batteries, *ACS Applied Energy Materials* 2(5) (2019) 3028-3034.
- [61] T. Guan, Z. Rong, F. Cheng, W. Zhang, J. Chen, UV-cured interpenetrating networks of single-ion conducting polymer electrolytes for rechargeable lithium metal batteries, *ACS Applied Energy Materials* 3(12) (2020) 12532-12539.
- [62] K. Deng, S. Wang, S. Ren, D. Han, M. Xiao, Y. Meng, Network type sp³ boron-based single-ion conducting polymer electrolytes for lithium ion batteries, *Journal of Power Sources* 360 (2017) 98-105.
- [63] K. Deng, D. Han, S. Ren, S. Wang, M. Xiao, Y. Meng, Single-ion conducting artificial solid electrolyte interphase layers for dendrite-free and highly stable lithium metal anodes, *Journal of Materials Chemistry A* 7(21) (2019) 13113-13119.
- [64] J. Zhang, S. Wang, D. Han, M. Xiao, L. Sun, Y. Meng, Lithium (4-styrenesulfonyl)(trifluoromethanesulfonyl) imide based single-ion polymer electrolyte with superior battery performance, *Energy Storage Materials* 24 (2020) 579-587.
- [65] W. Ren, C. Ding, X. Fu, Y. Huang, Advanced gel polymer electrolytes for safe and durable lithium metal batteries: Challenges, strategies, and perspectives, *Energy Storage Materials* (2020).
- [66] H.O. Ford, B. Park, J. Jiang, M.E. Seidler, J.L. Schaefer, Enhanced Li⁺ conduction within single-ion conducting polymer gel electrolytes via reduced cation–polymer interaction, *ACS Materials Letters* 2(3) (2020) 272-279.

- [67] L. Porcarelli, A.S. Shaplov, F. Bella, J.R. Nair, D. Mecerreyes, C. Gerbaldi, Single-ion conducting polymer electrolytes for lithium metal polymer batteries that operate at ambient temperature, *ACS Energy Letters* 1(4) (2016) 678-682.
- [68] Y. Zhong, L. Zhong, S. Wang, J. Qin, D. Han, S. Ren, M. Xiao, L. Sun, Y. Meng, Ultrahigh Li-ion conductive single-ion polymer electrolyte containing fluorinated polysulfonamide for quasi-solid-state Li-ion batteries, *Journal of Materials Chemistry A* 7(42) (2019) 24251-24261.
- [69] H. Yang, B. Liu, J. Bright, S. Kasani, J. Yang, X. Zhang, N. Wu, A single-ion conducting UIO-66 metal–organic framework electrolyte for all-solid-state lithium batteries, *ACS Applied Energy Materials* 3(4) (2020) 4007-4013.
- [70] P. Yao, H. Yu, Z. Ding, Y. Liu, J. Lu, M. Lavorgna, J. Wu, X. Liu, Review on polymer-based composite electrolytes for lithium batteries, *Frontiers in chemistry* 7 (2019) 522.
- [71] C.-W. Nan, L. Fan, Y. Lin, Q. Cai, Enhanced Ionic Conductivity of Polymer Electrolytes Containing Nanocomposite SiO₂ Particles, *Physical review letters* 91(26) (2003) 266104.
- [72] S.N. Banitaba, D. Semnani, E. Heydari-Soureshjani, B. Rezaei, A.A. Ensafi, Electrospun polyethylene oxide-based membranes incorporated with silicon dioxide, aluminum oxide and clay nanoparticles as flexible solvent-free electrolytes for lithium-ion batteries, *Jom* 71(12) (2019) 4537-4546.
- [73] S. Chung, Y. Wang, L. Persi, F. Croce, S. Greenbaum, B. Scrosati, E. Plichta, Enhancement of ion transport in polymer electrolytes by addition of nanoscale inorganic oxides, *Journal of power sources* 97 (2001) 644-648.
- [74] J. Weston, B. Steele, Effects of inert fillers on the mechanical and electrochemical properties of lithium salt-poly (ethylene oxide) polymer electrolytes, *Solid State Ionics* 7(1) (1982) 75-79.

- [75] D. Lin, W. Liu, Y. Liu, H.R. Lee, P.-C. Hsu, K. Liu, Y. Cui, High ionic conductivity of composite solid polymer electrolyte via in situ synthesis of monodispersed SiO₂ nanospheres in poly (ethylene oxide), *Nano letters* 16(1) (2016) 459-465.
- [76] C. Ma, J. Zhang, M. Xu, Q. Xia, J. Liu, S. Zhao, L. Chen, A. Pan, D.G. Ivey, W. Wei, Cross-linked branching nanohybrid polymer electrolyte with monodispersed TiO₂ nanoparticles for high performance lithium-ion batteries, *Journal of Power Sources* 317 (2016) 103-111.
- [77] M. Faraday, V. Experimental researches in electricity, *Philosophical transactions of the Royal Society of London* (122) (1832) 125-162.
- [78] K. Funke, *Solid State Ionics: from Michael Faraday to green energy—the European dimension*, *Science and Technology of Advanced Materials* (2013).
- [79] E. Warburg, F. Tegetmeier, Ueber die electrolytische Leitung des Bergkrystalls, *Annalen der Physik* 271(11) (1888) 455-467.
- [80] C. Tubandt, E. Lorenz, Molekularzustand und elektrisches Leitvermögen kristallisierter Salze, *Zeitschrift für Physikalische Chemie* 87(1) (1914) 513-542.
- [81] C. Wagner, Theorie der geordneten Mischphasen. III, *Zeitschrift für Physikalische Chemie* 22(1) (1933) 181-194.
- [82] K. Takada, Progress and prospective of solid-state lithium batteries, *Acta Materialia* 61(3) (2013) 759-770.
- [83] K. Zhang, G.H. Lee, M. Park, W. Li, Y.M. Kang, Recent developments of the lithium metal anode for rechargeable non-aqueous batteries, *Advanced Energy Materials* 6(20) (2016) 1600811.

- [84] Q. Liu, Z. Geng, C. Han, Y. Fu, S. Li, Y.-b. He, F. Kang, B. Li, Challenges and perspectives of garnet solid electrolytes for all solid-state lithium batteries, *Journal of Power Sources* 389 (2018) 120-134.
- [85] C. Wang, K. Fu, S.P. Kammampata, D.W. McOwen, A.J. Samson, L. Zhang, G.T. Hitz, A.M. Nolan, E.D. Wachsman, Y. Mo, Garnet-type solid-state electrolytes: materials, interfaces, and batteries, *Chemical reviews* 120(10) (2020) 4257-4300.
- [86] Y. He, C. Lu, S. Liu, W. Zheng, J. Luo, Interfacial incompatibility and internal stresses in all-solid-state lithium ion batteries, *Advanced Energy Materials* 9(36) (2019) 1901810.
- [87] T.-B. Song, Q. Chen, H. Zhou, C. Jiang, H.-H. Wang, Y.M. Yang, Y. Liu, J. You, Y. Yang, Perovskite solar cells: film formation and properties, *Journal of Materials Chemistry A* 3(17) (2015) 9032-9050.
- [88] J. Brous, I. Fankuchen, E. Banks, Rare earth titanates with a perovskite structure, *Acta crystallographica* 6(1) (1953) 67-70.
- [89] V. Thangadurai, W. Weppner, Recent progress in solid oxide and lithium ion conducting electrolytes research, *Ionics* 12(1) (2006) 81-92.
- [90] T. Takahashi, H. Iwahara, Ionic conduction in perovskite-type oxide solid solution and its application to the solid electrolyte fuel cell, *Energy Conversion* 11(3) (1971) 105-111.
- [91] A. Belous, G. Novitskaya, S. Polyanetskaya, Y.I. Gornikov, Investigation into complex oxides of $\text{La}_{2/3-x}\text{Li}_{3x}\text{TiO}_3$ composition, *Izv. Akad. Nauk SSSR, Neorg. Mater* 23(3) (1987) 470-472.
- [92] Y. Inaguma, C. Liqun, M. Itoh, T. Nakamura, T. Uchida, H. Ikuta, M. Wakihara, High ionic conductivity in lithium lanthanum titanate, *Solid State Communications* 86(10) (1993) 689-693.

- [93] H. Xu, H. Zhang, J. Ma, G. Xu, T. Dong, J. Chen, G. Cui, Overcoming the challenges of 5 V spinel $\text{LiNi}_0.5\text{Mn}_1.5\text{O}_4$ cathodes with solid polymer electrolytes, *ACS Energy Letters* 4(12) (2019) 2871-2886.
- [94] H.T. Le, R.S. Kalubarme, D.T. Ngo, H.S. Jadhav, C.-J. Park, Bi-layer lithium phosphorous oxynitride/aluminium substituted lithium lanthanum titanate as a promising solid electrolyte for long-life rechargeable lithium–oxygen batteries, *Journal of Materials Chemistry A* 3(44) (2015) 22421-22431.
- [95] L.O. Hagman, P. Kierkegaard, P. Karvonen, A. Virtanen, J. Paasivirta, The crystal structure of $\text{NaMe}_2\text{IV}(\text{PO}_4)_3$; $\text{MeIV} = \text{Ge, Ti, Zr}$, *Acta Chem. Scand* 22(6) (1968) 1822-32.
- [96] J.B. Goodenough, H.-P. Hong, J. Kafalas, Fast Na^+ -ion transport in skeleton structures, *Materials Research Bulletin* 11(2) (1976) 203-220.
- [97] C.R. Mariappan, C. Yada, F. Rosciano, B. Roling, Correlation between micro-structural properties and ionic conductivity of $\text{Li}_{1.5}\text{Al}_{1.0}\text{Ge}_{1.5}(\text{PO}_4)_3$ ceramics, *Journal of Power Sources* 196(15) (2011) 6456-6464.
- [98] Z. Gao, H. Sun, L. Fu, F. Ye, Y. Zhang, W. Luo, Y. Huang, Promises, challenges, and recent progress of inorganic solid-state electrolytes for all-solid-state lithium batteries, *Advanced materials* 30(17) (2018) 1705702.
- [99] H.-P. Hong, Crystal structure and ionic conductivity of $\text{Li}_{14}\text{Zn}(\text{GeO}_4)_4$ and other new Li^+ superionic conductors, *Materials Research Bulletin* 13(2) (1978) 117-124.
- [100] Z. Wen, X. Xu, J. Li, Preparation, microstructure and electrical properties of $\text{Li}_{1.4}\text{Al}_{1.0}\text{Ti}_{1.6}(\text{PO}_4)_3$ nanoceramics, *Journal of electroceramics* 22(1) (2009) 342-345.

- [101] K. Arbi, W. Bucheli, R. Jiménez, J. Sanz, High lithium ion conducting solid electrolytes based on NASICON $\text{Li}_{1+x}\text{Al}_x\text{M}_{2-x}(\text{PO}_4)_3$ materials (M= Ti, Ge and $0 \leq x \leq 0.5$), *Journal of the European Ceramic Society* 35(5) (2015) 1477-1484.
- [102] A.M. Cruz, E.B. Ferreira, A.C.M. Rodrigues, Controlled crystallization and ionic conductivity of a nanostructured LiAlGePO_4 glass–ceramic, *Journal of Non-Crystalline Solids* 355(45-47) (2009) 2295-2301.
- [103] J. Fu, Fast Li^+ ion conducting glass-ceramics in the system $\text{Li}_2\text{O}-\text{Al}_2\text{O}_3-\text{GeO}_2-\text{P}_2\text{O}_5$, *Solid State Ionics* 104(3-4) (1997) 191-194.
- [104] J.S. Thokchom, N. Gupta, B. Kumar, Superionic conductivity in a lithium aluminum germanium phosphate glass–ceramic, *Journal of the Electrochemical Society* 155(12) (2008) A915.
- [105] H. Kitaura, H. Zhou, Electrochemical performance of solid-state lithium–air batteries using carbon nanotube catalyst in the air electrode, *Advanced Energy Materials* 2(7) (2012) 889-894.
- [106] V. Thangadurai, S. Narayanan, D. Pinzarú, Garnet-type solid-state fast Li ion conductors for Li batteries: critical review, *Chemical Society Reviews* 43(13) (2014) 4714-4727.
- [107] S. Ramakumar, C. Deviannapoorani, L. Dhivya, L.S. Shankar, R. Murugan, Lithium garnets: Synthesis, structure, Li^+ conductivity, Li^+ dynamics and applications, *Progress in Materials Science* 88 (2017) 325-411.
- [108] W. AF, *Structural Inorganic Chemistry*, Clarendon Press, Oxford, 1975.
- [109] E.J. Cussen, The structure of lithium garnets: cation disorder and clustering in a new family of fast Li^+ conductors, *Chemical Communications* (4) (2006) 412-413.

- [110] V. Thangadurai, H. Kaack, W.J. Weppner, Novel fast lithium ion conduction in garnet-type $\text{Li}_5\text{La}_3\text{M}_2\text{O}_{12}$ ($\text{M} = \text{Nb}, \text{Ta}$), *Journal of the American Ceramic Society* 86(3) (2003) 437-440.
- [111] C.A. Geiger, E. Alekseev, B. Lazic, M. Fisch, T. Armbruster, R. Langner, M. Fechtelkord, N. Kim, T. Pettke, W. Weppner, Crystal chemistry and stability of “ $\text{Li}_7\text{La}_3\text{Zr}_2\text{O}_{12}$ ” garnet: a fast lithium-ion conductor, *Inorganic chemistry* 50(3) (2011) 1089-1097.
- [112] R. Murugan, S. Ramakumar, N. Janani, High conductive yttrium doped $\text{Li}_7\text{La}_3\text{Zr}_2\text{O}_{12}$ cubic lithium garnet, *Electrochemistry Communications* 13(12) (2011) 1373-1375.
- [113] J.L. Allen, J. Wolfenstine, E. Rangasamy, J. Sakamoto, Effect of substitution ($\text{Ta}, \text{Al}, \text{Ga}$) on the conductivity of $\text{Li}_7\text{La}_3\text{Zr}_2\text{O}_{12}$, *Journal of Power Sources* 206 (2012) 315-319.
- [114] S. Ohta, T. Kobayashi, T. Asaoka, High lithium ionic conductivity in the garnet-type oxide $\text{Li}_{7-X}\text{La}_3(\text{Zr}_{2-X}\text{Nb}_X)\text{O}_{12}$ ($X = 0-2$), *Journal of Power Sources* 196(6) (2011) 3342-3345.
- [115] V. Thangadurai, W. Weppner, $\text{Li}_6\text{A}\text{La}_2\text{Nb}_2\text{O}_{12}$ ($\text{A} = \text{Ca}, \text{Sr}, \text{Ba}$): A New Class of Fast Lithium Ion Conductors with Garnet-Like Structure, *Journal of the American Ceramic Society* 88(2) (2005) 411-418.
- [116] V. Thangadurai, W. Weppner, $\text{Li}_6\text{A}\text{La}_2\text{Ta}_2\text{O}_{12}$ ($\text{A} = \text{Sr}, \text{Ba}$): novel garnet-like oxides for fast lithium ion conduction, *Advanced Functional Materials* 15(1) (2005) 107-112.
- [117] R. Murugan, V. Thangadurai, W. Weppner, Fast lithium ion conduction in garnet-type $\text{Li}_7\text{La}_3\text{Zr}_2\text{O}_{12}$, *Angewandte Chemie International Edition* 46(41) (2007) 7778-7781.
- [118] J. Percival, E. Kendrick, R. Smith, P. Slater, Cation ordering in Li containing garnets: synthesis and structural characterisation of the tetragonal system, $\text{Li}_7\text{La}_3\text{Sn}_2\text{O}_{12}$, *Dalton Transactions* (26) (2009) 5177-5181.

- [119] J. Awaka, N. Kijima, K. Kataoka, H. Hayakawa, K.-i. Ohshima, J. Akimoto, Neutron powder diffraction study of tetragonal $\text{Li}_7\text{La}_3\text{Hf}_2\text{O}_{12}$ with the garnet-related type structure, *Journal of Solid State Chemistry* 183(1) (2010) 180-185.
- [120] J.-F. Wu, W.K. Pang, V.K. Peterson, L. Wei, X. Guo, Garnet-type fast Li-ion conductors with high ionic conductivities for all-solid-state batteries, *ACS Applied Materials & Interfaces* 9(14) (2017) 12461-12468.
- [121] V. Thangadurai, D. Pinzaru, S. Narayanan, A.K. Baral, Fast solid-state Li ion conducting garnet-type structure metal oxides for energy storage, *The journal of physical chemistry letters* 6(2) (2015) 292-299.
- [122] L. Dhivya, R. Murugan, Effect of simultaneous substitution of Y and Ta on the stabilization of cubic phase, microstructure, and Li^+ conductivity of $\text{Li}_7\text{La}_3\text{Zr}_2\text{O}_{12}$ lithium garnet, *ACS Applied Materials & Interfaces* 6(20) (2014) 17606-17615.
- [123] L. Buannic, B. Orayech, J.-M. Lopez Del Amo, J. Carrasco, N.A. Katcho, F.d.r. Aguesse, W. Manalastas, W. Zhang, J. Kilner, A. Llordés, Dual substitution strategy to enhance Li^+ ionic conductivity in $\text{Li}_7\text{La}_3\text{Zr}_2\text{O}_{12}$ solid electrolyte, *Chemistry of materials* 29(4) (2017) 1769-1778.
- [124] Y. Jiang, X. Zhu, S. Qin, J. Zhu, Investigation of Mg^{2+} , Sc^{3+} and Zn^{2+} doping effects on densification and ionic conductivity of low-temperature sintered $\text{Li}_7\text{La}_3\text{Zr}_2\text{O}_{12}$ garnets, *Solid State Ionics* 300 (2017) 73-77.
- [125] Y. Lu, X. Meng, J.A. Alonso, M.T. Fernández-Díaz, C. Sun, Effects of fluorine doping on structural and electrochemical properties of $\text{Li}_6.25\text{Ga}_0.25\text{La}_3\text{Zr}_2\text{O}_{12}$ as electrolytes for solid-state lithium batteries, *ACS Applied Materials & Interfaces* 11(2) (2018) 2042-2049.
- [126] L.H. Abrha, T.T. Hagos, Y. Nikodimos, H.K. Bezabh, G.B. Berhe, T.M. Hagos, C.-J. Huang, W.A. Tegegne, S.-K. Jiang, H.H. Weldeyohannes, Dual-doped cubic garnet solid

electrolytes with superior air stability, *Acs Applied Materials & Interfaces* 12(23) (2020) 25709-25717.

[127] J.C. Bachman, S. Muy, A. Grimaud, H.-H. Chang, N. Pour, S.F. Lux, O. Paschos, F. Maglia, S. Lupart, P. Lamp, Inorganic solid-state electrolytes for lithium batteries: mechanisms and properties governing ion conduction, *Chemical reviews* 116(1) (2016) 140-162.

[128] Y. Li, B. Xu, H. Xu, H. Duan, X. Lü, S. Xin, W. Zhou, L. Xue, G. Fu, A. Manthiram, Hybrid polymer/garnet electrolyte with a small interfacial resistance for lithium-ion batteries, *Angewandte Chemie International Edition* 56(3) (2017) 753-756.

[129] S. Yu, R.D. Schmidt, R. Garcia-Mendez, E. Herbert, N.J. Dudney, J.B. Wolfenstine, J. Sakamoto, D.J. Siegel, Elastic properties of the solid electrolyte $\text{Li}_7\text{La}_3\text{Zr}_2\text{O}_{12}$ (LLZO), *Chemistry of Materials* 28(1) (2016) 197-206.

[130] Y.A. Du, N. Holzwarth, Mechanisms of Li^+ diffusion in crystalline γ - and β - Li_3PO_4 electrolytes from first principles, *Physical Review B* 76(17) (2007) 174302.

[131] P.G. Bruce, A. West, The A-C conductivity of polycrystalline LISICON, $\text{Li}_{2+2x}\text{Zn}_{1-x}\text{GeO}_4$, and a model for intergranular constriction resistances, *Journal of The Electrochemical Society* 130(3) (1983) 662.

[132] P. Bruce, A. West, Ionic conductivity of LISICON solid solutions, $\text{Li}_{2+2x}\text{Zn}_{1-x}\text{GeO}_4$, *Journal of Solid State Chemistry* 44(3) (1982) 354-365.

[133] Y. Meesala, A. Jena, H. Chang, R.-S. Liu, Recent advancements in Li-ion conductors for all-solid-state Li-ion batteries, *ACS Energy Letters* 2(12) (2017) 2734-2751.

[134] P. Knauth, Inorganic solid Li ion conductors: An overview, *Solid State Ionics* 180(14-16) (2009) 911-916.

- [135] A. Robertson, A. West, A. Ritchie, Review of crystalline lithium-ion conductors suitable for high temperature battery applications, *Solid State Ionics* 104(1-2) (1997) 1-11.
- [136] J. Kuwano, A. West, New Li⁺ ion conductors in the system, Li₄GeO₄-Li₃VO₄, *Materials Research Bulletin* 15(11) (1980) 1661-1667.
- [137] Y. Deng, C. Eames, B. Fleutot, R. David, J.-N. Chotard, E. Suard, C. Masquelier, M.S. Islam, Enhancing the lithium ion conductivity in lithium superionic conductor (LISICON) solid electrolytes through a mixed polyanion effect, *ACS applied materials & interfaces* 9(8) (2017) 7050-7058.
- [138] M. Tachez, J.-P. Malugani, R. Mercier, G. Robert, Ionic conductivity of and phase transition in lithium thiophosphate Li₃PS₄, *Solid State Ionics* 14(3) (1984) 181-185.
- [139] J.H. Kennedy, S. Sahami, S.W. Shea, Z. Zhang, Preparation and conductivity measurements of SiS₂□ Li₂S glasses doped with LiBr and LiCl, *Solid State Ionics* 18 (1986) 368-371.
- [140] J.H. Kennedy, Y. Yang, A highly conductive Li⁺-glass system:(1-x)(0.4 SiS₂-0.6 Li₂S)-xLiI, *J. Electrochem. Soc* 133 (1986) 2437-2438.
- [141] B.T. Ahn, R.A. Huggins, Phase behavior and conductivity of Li₂SiS₃ composition, *Solid state ionics* 46(3-4) (1991) 237-242.
- [142] H. Morimoto, H. Yamashita, M. Tatsumisago, T. Minami, Mechanochemical synthesis of new amorphous materials of 60Li₂S· 40SiS₂ with high lithium ion conductivity, *Journal of the American Ceramic Society* 82(5) (1999) 1352-1354.
- [143] R. Kanno, T. Hata, Y. Kawamoto, M. Irie, Synthesis of a new lithium ionic conductor, thio-LISICON–lithium germanium sulfide system, *Solid state ionics* 130(1-2) (2000) 97-104.

- [144] C. Cao, Z.-B. Li, X.-L. Wang, X.-B. Zhao, W.-Q. Han, Recent advances in inorganic solid electrolytes for lithium batteries, *Frontiers in energy research* 2 (2014) 25.
- [145] Y.S. Jung, D.Y. Oh, Y.J. Nam, K.H. Park, Issues and challenges for bulk-type all-solid-state rechargeable lithium batteries using sulfide solid electrolytes, *Israel Journal of Chemistry* 55(5) (2015) 472-485.
- [146] A. Hayashi, H. Muramatsu, T. Ohtomo, S. Hama, M. Tatsumisago, Improved chemical stability and cyclability in $\text{Li}_2\text{S}-\text{P}_2\text{S}_5-\text{P}_2\text{O}_5-\text{ZnO}$ composite electrolytes for all-solid-state rechargeable lithium batteries, *Journal of alloys and compounds* 591 (2014) 247-250.
- [147] X. Shen, Q. Zhang, T. Ning, T. Liu, Y. Luo, X. He, Z. Luo, A. Lu, Critical challenges and progress of solid garnet electrolytes for all-solid-state batteries, *Materials Today Chemistry* 18 (2020) 100368.
- [148] Y. Liu, P. He, H. Zhou, Rechargeable solid-state Li-Air and Li-S batteries: materials, construction, and challenges, *Advanced Energy Materials* 8(4) (2018) 1701602.
- [149] A.A. Almetwally, M. El-Sakhawy, M. Elshakankery, M. Kasem, Technology of nano-fibers: Production techniques and properties-Critical review, *J. Text. Assoc* 78(1) (2017) 5-14.
- [150] O. Fesenko, L. Yatsenko, *Nanochemistry, Biotechnology, Nanomaterials, and Their Applications*, Springer 2018.
- [151] H. Zhao, Y. Lei, 3D Nanostructures for the Next Generation of High-Performance Nanodevices for Electrochemical Energy Conversion and Storage, *Advanced Energy Materials* 10(28) (2020) 2001460.
- [152] Y. Li, Y. Sun, Y. Qin, W. Zhang, L. Wang, M. Luo, H. Yang, S. Guo, Recent advances on water-splitting electrocatalysis mediated by noble-metal-based nanostructured materials, *Advanced Energy Materials* 10(11) (2020) 1903120.

- [153] Y. Li, J. Zhu, H. Cheng, G. Li, H. Cho, M. Jiang, Q. Gao, X. Zhang, Developments of advanced electrospinning techniques: A critical review, *Advanced Materials Technologies* (2021) 2100410.
- [154] Y. Li, J. Zhu, P. Zhu, C. Yan, H. Jia, Y. Kiyak, J. Zang, J. He, M. Dirican, X. Zhang, Glass fiber separator coated by porous carbon nanofiber derived from immiscible PAN/PMMA for high-performance lithium-sulfur batteries, *Journal of Membrane Science* 552 (2018) 31-42.
- [155] P. Zhu, C. Yan, J. Zhu, J. Zang, Y. Li, H. Jia, X. Dong, Z. Du, C. Zhang, N. Wu, Flexible electrolyte-cathode bilayer framework with stabilized interface for room-temperature all-solid-state lithium-sulfur batteries, *Energy Storage Materials* 17 (2019) 220-225.
- [156] W.E. Teo, S. Ramakrishna, A review on electrospinning design and nanofibre assemblies, *Nanotechnology* 17(14) (2006) R89.
- [157] P. Zhu, J. Zhu, C. Yan, M. Dirican, J. Zang, H. Jia, Y. Li, Y. Kiyak, H. Tan, X. Zhang, In Situ Polymerization of Nanostructured Conductive Polymer on 3D Sulfur/Carbon Nanofiber Composite Network as Cathode for High-Performance Lithium–Sulfur Batteries, *Advanced Materials Interfaces* 5(10) (2018) 1701598.
- [158] H. Jia, M. Dirican, C. Chen, J. Zhu, P. Zhu, C. Yan, Y. Li, X. Dong, J. Guo, X. Zhang, Reduced graphene oxide-incorporated SnSb@ CNF composites as anodes for high-performance sodium-ion batteries, *ACS applied materials & interfaces* 10(11) (2018) 9696-9703.
- [159] C. Chen, G. Li, J. Zhu, Y. Lu, M. Jiang, Y. Hu, Z. Shen, X. Zhang, In-situ formation of tin-antimony sulfide in nitrogen-sulfur Co-doped carbon nanofibers as high performance anode materials for sodium-ion batteries, *Carbon* 120 (2017) 380-391.

- [160] J. Zhu, Y. Lu, C. Chen, Y. Ge, S. Jasper, J.D. Leary, D. Li, M. Jiang, X. Zhang, Porous one-dimensional carbon/iron oxide composite for rechargeable lithium-ion batteries with high and stable capacity, *Journal of Alloys and Compounds* 672 (2016) 79-85.
- [161] D. Lee, Functional material developments of fuel cells and the key factors for real commercialization of next-generation energy devices, *Sustainable Materials for Next Generation Energy Devices*, Elsevier 2021, pp. 85-100.
- [162] M. Yanilmaz, Y. Lu, J. Zhu, X. Zhang, Silica/polyacrylonitrile hybrid nanofiber membrane separators via sol-gel and electrospinning techniques for lithium-ion batteries, *Journal of Power Sources* 313 (2016) 205-212.
- [163] Y. Ge, J. Zhu, Y. Lu, C. Chen, Y. Qiu, X. Zhang, The study on structure and electrochemical sodiation of one-dimensional nanocrystalline TiO₂@ C nanofiber composites, *Electrochimica Acta* 176 (2015) 989-996.
- [164] Y. Ge, H. Jiang, K. Fu, C. Zhang, J. Zhu, C. Chen, Y. Lu, Y. Qiu, X. Zhang, Copper-doped Li₄Ti₅O₁₂/carbon nanofiber composites as anode for high-performance sodium-ion batteries, *Journal of Power Sources* 272 (2014) 860-865.
- [165] X. Wang, G.M. Girard, H. Zhu, R. Yunis, D.R. MacFarlane, D. Mecerreyes, A.J. Bhattacharyya, P.C. Howlett, M. Forsyth, Poly (ionic liquid) s/electrospun nanofiber composite polymer electrolytes for high energy density and safe Li metal batteries, *ACS Applied Energy Materials* 2(9) (2019) 6237-6245.
- [166] S. Nakazawa, Y. Matsuda, M. Ochiai, Y. Inafune, M. Yamato, M. Tanaka, H. Kawakami, Enhancing Lithium ion conductivity and all-solid-state secondary battery performance in polymer composite electrolyte membranes with β -Crystalline-rich Poly (vinylidene fluoride) Nanofibers, *Electrochimica Acta* 394 (2021) 139114.

- [167] L. Tian, Y. Liu, Z. Su, Y. Cao, W. Zhang, S. Yi, Y. Zhang, B. Niu, P. Dong, D. Long, A lithiated organic nanofiber-reinforced composite polymer electrolyte enabling Li-ion conduction highways for solid-state lithium metal batteries, *Journal of Materials Chemistry A* 9(42) (2021) 23882-23890.
- [168] L. Gao, J. Li, J. Ju, B. Cheng, W. Kang, N. Deng, High-performance all-solid-state polymer electrolyte with fast conductivity pathway formed by hierarchical structure polyamide 6 nanofiber for lithium metal battery, *Journal of Energy Chemistry* 54 (2021) 644-654.
- [169] W. Yu, N. Deng, Z. Yan, L. Gao, K. Cheng, X. Tian, L. Tang, B. Cheng, W. Kang, Mg-based inorganic nanofibers constructing fast and multi-dimensional ion conductive pathways for all-solid-state lithium metal batteries, *Journal of Energy Chemistry* 67 (2022) 684-696.
- [170] K.-Q. He, J.-W. Zha, P. Du, S.H.-S. Cheng, C. Liu, Z.-M. Dang, R.K. Li, Tailored high cycling performance in a solid polymer electrolyte with perovskite-type $\text{Li}_{0.33}\text{La}_{0.557}\text{TiO}_3$ nanofibers for all-solid-state lithium ion batteries, *Dalton Transactions* 48(10) (2019) 3263-3269.
- [171] B. Li, Q. Su, L. Yu, D. Wang, S. Ding, M. Zhang, G. Du, B. Xu, $\text{Li}_{0.35}\text{La}_{0.55}\text{TiO}_3$ nanofibers enhanced poly (vinylidene fluoride)-based composite polymer electrolytes for all-solid-state batteries, *ACS Applied Materials & Interfaces* 11(45) (2019) 42206-42213.
- [172] K. Liu, R. Zhang, J. Sun, M. Wu, T. Zhao, Polyoxyethylene (PEO)|PEO-perovskite|PEO composite electrolyte for all-solid-state lithium metal batteries, *ACS Applied Materials & Interfaces* 11(50) (2019) 46930-46937.
- [173] E. Zhao, Y. Guo, A. Zhang, H. Wang, G. Xu, Polydopamine coated TiO_2 nanofiber fillers for polyethylene oxide hybrid electrolytes for efficient and durable all solid state lithium ion batteries, *Nanoscale* (2022).

- [174] A. La Monaca, A. Paolella, A. Guerfi, F. Rosei, K. Zaghib, Electrospun ceramic nanofibers as 1D solid electrolytes for lithium batteries, *Electrochemistry Communications* 104 (2019) 106483.
- [175] A. La Monaca, G. Girard, S. Savoie, G. Bertoni, S. Krachkovskiy, A. Vijh, F. Pierini, F. Rosei, A. Paolella, Synthesis of Electrospun NASICON $\text{Li}_{1.5}\text{Al}_{1.5}\text{Ge}_{1.5}(\text{PO}_4)_3$ Solid Electrolyte Nanofibers by Control of Germanium Hydrolysis, *Journal of The Electrochemical Society* 168(11) (2021) 110512.
- [176] P. Zhu, C. Yan, M. Dirican, J. Zhu, J. Zang, R.K. Selvan, C.-C. Chung, H. Jia, Y. Li, Y. Kiyak, $\text{Li}_{0.33}\text{La}_{0.557}\text{TiO}_3$ ceramic nanofiber-enhanced polyethylene oxide-based composite polymer electrolytes for all-solid-state lithium batteries, *Journal of Materials Chemistry A* 6(10) (2018) 4279-4285.
- [177] X. Wang, Y. Zhang, X. Zhang, T. Liu, Y.-H. Lin, L. Li, Y. Shen, C.-W. Nan, Lithium-salt-rich PEO/ $\text{Li}_{0.3}\text{La}_{0.557}\text{TiO}_3$ interpenetrating composite electrolyte with three-dimensional ceramic nano-backbone for all-solid-state lithium-ion batteries, *ACS applied materials & interfaces* 10(29) (2018) 24791-24798.
- [178] H. Yang, M. Abdullah, J. Bright, W. Hu, K. Kittilstved, Y. Xu, C. Wang, X. Zhang, N. Wu, Polymer-ceramic composite electrolytes for all-solid-state lithium batteries: Ionic conductivity and chemical interaction enhanced by oxygen vacancy in ceramic nanofibers, *Journal of Power Sources* 495 (2021) 229796.
- [179] Y. Zhang, W. Feng, Y. Zhen, P. Zhao, X. Wang, L. Li, Enhancement of cycling stability of all-solid-state lithium-ion batteries with composite polymer electrolytes incorporating $\text{Li}_6\text{La}_3\text{Zr}_2\text{AlO}_{12}$ nanofibers, *Ionics* 26(9) (2020) 4239-4246.

- [180] X. Zheng, T. Yang, J. Wei, C. Wang, M. Chen, Co-contribution of quenching and nanocrystallization on ionic-conductivity improvement of a composite electrolyte of polyethylene Oxide/Li₇La₃Zr₂O₁₂ nanofibers at 45° C for all-solid-state Li metal batteries, *Journal of Power Sources* 496 (2021) 229843.
- [181] Y. Zhao, J. Yan, W. Cai, Y. Lai, J. Song, J. Yu, B. Ding, Elastic and well-aligned ceramic LLZO nanofiber based electrolytes for solid-state lithium batteries, *Energy Storage Materials* 23 (2019) 306-313.
- [182] C. Yan, P. Zhu, H. Jia, Z. Du, J. Zhu, R. Orenstein, H. Cheng, N. Wu, M. Dirican, X. Zhang, Garnet-rich composite solid electrolytes for dendrite-free, high-rate, solid-state lithium-metal batteries, *Energy Storage Materials* 26 (2020) 448-456.
- [183] X. Zheng, J. Wei, W. Lin, K. Ji, C. Wang, M. Chen, Bridging Li₇La₃Zr₂O₁₂ Nanofibers with Poly (ethylene oxide) by Coordination Bonds to Enhance the Cycling Stability of All-Solid-State Lithium Metal Batteries, *ACS Applied Materials & Interfaces* (2022).
- [184] H. Xu, X. Zhang, J. Jiang, M. Li, Y. Shen, Ultrathin Li₇La₃Zr₂O₁₂@ PAN composite polymer electrolyte with high conductivity for all-solid-state lithium-ion battery, *Solid State Ionics* 347 (2020) 115227.
- [185] L. Gao, J. Li, J. Ju, B. Cheng, W. Kang, N. Deng, Polyvinylidene fluoride nanofibers with embedded Li₆.₄La₃Zr₁.₄Ta₀.₆O₁₂ fillers modified polymer electrolytes for high-capacity and long-life all-solid-state lithium metal batteries, *Composites Science and Technology* 200 (2020) 108408.
- [186] T.-Q. Yang, C. Wang, W.-K. Zhang, Y. Xia, Y.-P. Gan, H. Huang, X.-P. He, J. Zhang, Composite polymer electrolytes reinforced by a three-dimensional polyacrylonitrile/Li₀.₃₃La₀.

557TiO₃ nanofiber framework for room-temperature dendrite-free all-solid-state lithium metal battery, *Rare Metals* (2022) 1-10.

[187] S. Li, N. Li, C. Sun, A flexible three-dimensional composite nanofiber enhanced quasi-solid electrolyte for high-performance lithium metal batteries, *Inorganic Chemistry Frontiers* 8(2) (2021) 361-367.

[188] C.A. Vincent, Ion transport in polymer electrolytes, *Electrochimica Acta* 40(13-14) (1995) 2035-2040.

[189] A.M. Stephan, Review on gel polymer electrolytes for lithium batteries, *European polymer journal* 42(1) (2006) 21-42.

[190] G. Mao, R.F. Perea, W.S. Howells, D.L. Price, M.-L. Saboungi, Relaxation in polymer electrolytes on the nanosecond timescale, *Nature* 405(6783) (2000) 163-165.

[191] P.G. Bruce, *Solid state electrochemistry*, Cambridge university press 1997.

[192] G. Appetecchi, Y. Aihara, B. Scrosati, Investigation of swelling phenomena in PEO-based polymer electrolytes: II. Chemical and electrochemical characterization, *Solid State Ionics* 170(1-2) (2004) 63-72.

[193] Z. Chen, L. Zhang, R. West, K. Amine, Gel electrolyte for lithium-ion batteries, *Electrochimica acta* 53(8) (2008) 3262-3266.

[194] M. Patel, K.G. Chandrappa, A.J. Bhattacharyya, Increasing ionic conductivity of polymer-sodium salt complex by addition of a non-ionic plastic crystal, *Solid State Ionics* 181(17-18) (2010) 844-848.

[195] W. Wang, P. Alexandridis, Composite polymer electrolytes: Nanoparticles affect structure and properties, *Polymers* 8(11) (2016) 387.

- [196] M.H. Cohen, D. Turnbull, Molecular transport in liquids and glasses, *The Journal of Chemical Physics* 31(5) (1959) 1164-1169.
- [197] E. Quartarone, P. Mustarelli, Electrolytes for solid-state lithium rechargeable batteries: recent advances and perspectives, *Chemical Society Reviews* 40(5) (2011) 2525-2540.
- [198] J.H. Gibbs, E.A. DiMarzio, Nature of the glass transition and the glassy state, *The Journal of Chemical Physics* 28(3) (1958) 373-383.
- [199] H. Yang, J. Bright, B. Chen, P. Zheng, X. Gao, B. Liu, S. Kasani, X. Zhang, N. Wu, Chemical interaction and enhanced interfacial ion transport in a ceramic nanofiber–polymer composite electrolyte for all-solid-state lithium metal batteries, *Journal of Materials Chemistry A* 8(15) (2020) 7261-7272.
- [200] J. Zhu, C. Chen, Y. Lu, J. Zang, M. Jiang, D. Kim, X. Zhang, Highly porous polyacrylonitrile/graphene oxide membrane separator exhibiting excellent anti-self-discharge feature for high-performance lithium–sulfur batteries, *Carbon* 101 (2016) 272-280.
- [201] J. Zhu, E. Yildirim, K. Aly, J. Shen, C. Chen, Y. Lu, M. Jiang, D. Kim, A.E. Tonelli, M.A. Pasquinelli, Hierarchical multi-component nanofiber separators for lithium polysulfide capture in lithium–sulfur batteries: an experimental and molecular modeling study, *Journal of Materials Chemistry A* 4(35) (2016) 13572-13581.
- [202] Z. Tong, L. Huang, W. Lei, H. Zhang, S. Zhang, Carbon-containing electrospun nanofibers for lithium–sulfur battery: Current status and future directions, *Journal of Energy Chemistry* 54 (2021) 254-273.
- [203] Z. Osman, M.M. Ghazali, L. Othman, K.M. Isa, AC ionic conductivity and DC polarization method of lithium ion transport in PMMA–LiBF₄ gel polymer electrolytes, *Results in physics* 2 (2012) 1-4.

- [204] M. Morita, F. Araki, N. Yoshimoto, M. Ishikawa, H. Tsutsumi, Ionic conductance of polymeric electrolytes containing lithium salts mixed with rare earth salts, *Solid State Ionics* 136 (2000) 1167-1173.
- [205] S.B. Aziz, T.J. Woo, M. Kadir, H.M. Ahmed, A conceptual review on polymer electrolytes and ion transport models, *Journal of Science: Advanced Materials and Devices* 3(1) (2018) 1-17.
- [206] P.G. Bruce, C.A. Vincent, Steady state current flow in solid binary electrolyte cells, *Journal of electroanalytical chemistry and interfacial electrochemistry* 225(1-2) (1987) 1-17.
- [207] Z. Chen, D. Steinle, H.-D. Nguyen, J.-K. Kim, A. Mayer, J. Shi, E. Paillard, C. Iojoiu, S. Passerini, D. Bresser, High-energy lithium batteries based on single-ion conducting polymer electrolytes and Li [Ni_{0.8}Co_{0.1}Mn_{0.1}] O₂ cathodes, *Nano Energy* 77 (2020) 105129.
- [208] K. Borzutzki, J. Thienenkamp, M. Diehl, M. Winter, G. Brunklaus, Fluorinated polysulfonamide based single ion conducting room temperature applicable gel-type polymer electrolytes for lithium ion batteries, *Journal of Materials Chemistry A* 7(1) (2019) 188-201.
- [209] Y. Liu, D. Lin, Y. Jin, K. Liu, X. Tao, Q. Zhang, X. Zhang, Y. Cui, Transforming from planar to three-dimensional lithium with flowable interphase for solid lithium metal batteries, *Science advances* 3(10) (2017) eaao0713.
- [210] M. Tatsumisago, M. Nagao, A. Hayashi, Recent development of sulfide solid electrolytes and interfacial modification for all-solid-state rechargeable lithium batteries, *Journal of Asian Ceramic Societies* 1(1) (2013) 17-25.
- [211] Y. Gong, K. Fu, S. Xu, J. Dai, T.R. Hamann, L. Zhang, G.T. Hitz, Z. Fu, Z. Ma, D.W. McOwen, Lithium-ion conductive ceramic textile: a new architecture for flexible solid-state lithium metal batteries, *Materials today* 21(6) (2018) 594-601.

- [212] J. Zhang, N. Zhao, M. Zhang, Y. Li, P.K. Chu, X. Guo, Z. Di, X. Wang, H. Li, Flexible and ion-conducting membrane electrolytes for solid-state lithium batteries: dispersion of garnet nanoparticles in insulating polyethylene oxide, *Nano Energy* 28 (2016) 447-454.
- [213] K.K. Fu, Y. Gong, B. Liu, Y. Zhu, S. Xu, Y. Yao, W. Luo, C. Wang, S.D. Lacey, J. Dai, Toward garnet electrolyte-based Li metal batteries: An ultrathin, highly effective, artificial solid-state electrolyte/metallic Li interface, *Science Advances* 3(4) (2017) e1601659.
- [214] F. Ahmed, I. Choi, M.M. Rahman, H. Jang, T. Ryu, S. Yoon, L. Jin, Y. Jin, W. Kim, Remarkable conductivity of a self-healing single-ion conducting polymer electrolyte, poly(ethylene-Co-acrylic lithium (fluoro sulfonyl) imide), for all-solid-state Li-ion batteries, *ACS applied materials & interfaces* 11(38) (2019) 34930-34938.
- [215] L. Meabe, N. Goujon, C. Li, M. Armand, M. Forsyth, D. Mecerreyes, Single-Ion Conducting Poly (Ethylene Oxide Carbonate) as Solid Polymer Electrolyte for Lithium Batteries, *Batteries & Supercaps* 3(1) (2020) 68-75.
- [216] D.M. Shin, J.E. Bachman, M.K. Taylor, J. Kamcev, J.G. Park, M.E. Ziebel, E. Velasquez, N.N. Jarenwattananon, G.K. Sethi, Y. Cui, A Single-Ion Conducting Borate Network Polymer as a Viable Quasi-Solid Electrolyte for Lithium Metal Batteries, *Advanced Materials* 32(10) (2020) 1905771.
- [217] Y. He, J. Wang, Y. Zhang, S. Huo, D. Zeng, Y. Lu, Z. Liu, D. Wang, H. Cheng, Effectively suppressing lithium dendrite growth via an es-LiSPCE single-ion conducting nano fiber membrane, *Journal of Materials Chemistry A* 8(5) (2020) 2518-2528.
- [218] C. Cao, Y. Li, Y. Feng, C. Peng, Z. Li, W. Feng, A solid-state single-ion polymer electrolyte with ultrahigh ionic conductivity for dendrite-free lithium metal batteries, *Energy Storage Materials* 19 (2019) 401-407.

- [219] H. Yuan, J. Luan, Z. Yang, J. Zhang, Y. Wu, Z. Lu, H. Liu, Single lithium-ion conducting solid polymer electrolyte with superior electrochemical stability and interfacial compatibility for solid-state lithium metal batteries, *ACS applied materials & interfaces* 12(6) (2020) 7249-7256.
- [220] K.-L. Liu, C.-H. Chao, H.-C. Lee, C.-S. Tsao, J. Fang, N.-L. Wu, C.-Y. Chao, A novel non-porous separator based on single-ion conducting triblock copolymer for stable lithium electrodeposition, *Journal of Power Sources* 419 (2019) 58-64.
- [221] X. Guan, Q. Wu, X. Zhang, X. Guo, C. Li, J. Xu, In-situ crosslinked single ion gel polymer electrolyte with superior performances for lithium metal batteries, *Chemical Engineering Journal* 382 (2020) 122935.
- [222] D.S. Ginley, *Materials for electrochemical energy storage and conversion II--batteries, capacitors, and fuel cells : symposium held December 1-5, 1997, Boston, Massachusetts, U.S.A.*
- [223] G. Li, Z. Chen, J. Lu, Lithium-sulfur batteries for commercial applications, *Chem* 4(1) (2018) 3-7.
- [224] X.-B. Cheng, R. Zhang, C.-Z. Zhao, Q. Zhang, Toward safe lithium metal anode in rechargeable batteries: a review, *Chemical reviews* 117(15) (2017) 10403-10473.
- [225] H. Ye, Y. Zhang, Y.-X. Yin, F.-F. Cao, Y.-G. Guo, An outlook on low-volume-change lithium metal anodes for long-life batteries, *ACS Central Science* 6(5) (2020) 661-671.
- [226] K. Yan, H.-W. Lee, T. Gao, G. Zheng, H. Yao, H. Wang, Z. Lu, Y. Zhou, Z. Liang, Z. Liu, Ultrathin two-dimensional atomic crystals as stable interfacial layer for improvement of lithium metal anode, *Nano letters* 14(10) (2014) 6016-6022.
- [227] J. Wang, Q. Kang, J. Yuan, Q. Fu, C. Chen, Z. Zhai, Y. Liu, W. Yan, A. Li, J. Zhang, Dendrite-free lithium and sodium metal anodes with deep plating/stripping properties for lithium and sodium batteries, *Carbon Energy* 3(1) (2021) 153-166.

- [228] Y. Jiang, B. Wang, P. Liu, B. Wang, Y. Zhou, D. Wang, H. Liu, S. Dou, Modified solid-electrolyte interphase toward stable Li metal anode, *Nano Energy* 77 (2020) 105308.
- [229] S. Gao, F. Sun, N. Liu, H. Yang, P.-F. Cao, Ionic conductive polymers as artificial solid electrolyte interphase films in Li metal batteries—A review, *Materials Today* 40 (2020) 140-159.
- [230] H. Zhao, D. Lei, Y.B. He, Y. Yuan, Q. Yun, B. Ni, W. Lv, B. Li, Q.H. Yang, F. Kang, Compact 3D copper with uniform porous structure derived by electrochemical dealloying as dendrite-free lithium metal anode current collector, *Advanced Energy Materials* 8(19) (2018) 1800266.
- [231] D. Zhou, R. Liu, Y.B. He, F. Li, M. Liu, B. Li, Q.H. Yang, Q. Cai, F. Kang, SiO₂ hollow nanosphere-based composite solid electrolyte for lithium metal batteries to suppress lithium dendrite growth and enhance cycle life, *Advanced Energy Materials* 6(7) (2016) 1502214.
- [232] Y. Yang, G. Zheng, Y. Cui, Nanostructured sulfur cathodes, *Chemical Society Reviews* 42(7) (2013) 3018-3032.
- [233] H. Wang, X. Cao, W. Liu, X. Sun, Research progress of the solid state lithium-sulfur batteries, *Frontiers in Energy Research* 7 (2019) 112.
- [234] A. Manthiram, Y. Fu, Y.-S. Su, Challenges and prospects of lithium-sulfur batteries, *Accounts of chemical research* 46(5) (2013) 1125-1134.
- [235] H. Pan, Z. Cheng, P. He, H. Zhou, A review of solid-state lithium-sulfur battery: ion transport and polysulfide chemistry, *Energy & Fuels* 34(10) (2020) 11942-11961.
- [236] D. Lin, Y. Liu, Y. Cui, Reviving the lithium metal anode for high-energy batteries, *Nature nanotechnology* 12(3) (2017) 194-206.

- [237] T. Thompson, S. Yu, L. Williams, R.D. Schmidt, R. Garcia-Mendez, J. Wolfenstine, J.L. Allen, E. Kioupakis, D.J. Siegel, J. Sakamoto, Electrochemical window of the Li-ion solid electrolyte $\text{Li}_7\text{La}_3\text{Zr}_2\text{O}_{12}$, *ACS Energy Letters* 2(2) (2017) 462-468.
- [238] Y. Zhu, X. He, Y. Mo, First principles study on electrochemical and chemical stability of solid electrolyte–electrode interfaces in all-solid-state Li-ion batteries, *Journal of Materials Chemistry A* 4(9) (2016) 3253-3266.
- [239] R. Murugan, V. Thangadurai, W. Weppner, Schnelle lithiumionenleitung in granatartigem $\text{Li}_7\text{La}_3\text{Zr}_2\text{O}_{12}$, *Angewandte Chemie* 119(41) (2007) 7925-7928.
- [240] K.K. Fu, Y. Gong, J. Dai, A. Gong, X. Han, Y. Yao, C. Wang, Y. Wang, Y. Chen, C. Yan, Flexible, solid-state, ion-conducting membrane with 3D garnet nanofiber networks for lithium batteries, *Proceedings of the National Academy of Sciences* 113(26) (2016) 7094-7099.
- [241] J. Van Den Broek, S. Afyon, J.L. Rupp, Interface-engineered all-solid-state Li-ion batteries based on garnet-type fast Li^+ conductors, *Advanced Energy Materials* 6(19) (2016) 1600736.
- [242] T. Thompson, A. Sharafi, M.D. Johannes, A. Huq, J.L. Allen, J. Wolfenstine, J. Sakamoto, A tale of two sites: on defining the carrier concentration in garnet-based ionic conductors for advanced Li batteries, *Advanced Energy Materials* 5(11) (2015) 1500096.
- [243] Y. Zhu, X. He, Y. Mo, Origin of outstanding stability in the lithium solid electrolyte materials: insights from thermodynamic analyses based on first-principles calculations, *ACS applied materials & interfaces* 7(42) (2015) 23685-23693.
- [244] J. Hu, W. Wang, H. Peng, M. Guo, Y. Feng, Z. Xue, Y. Ye, X. Xie, Flexible organic–inorganic hybrid solid electrolytes formed via thiol–acrylate photopolymerization, *Macromolecules* 50(5) (2017) 1970-1980.

- [245] H.T. Le, D.T. Ngo, R.S. Kalubarme, G. Cao, C.-N. Park, C.-J. Park, Composite gel polymer electrolyte based on poly (vinylidene fluoride-hexafluoropropylene)(PVDF-HFP) with modified aluminum-doped lithium lanthanum titanate (A-LLTO) for high-performance lithium rechargeable batteries, *ACS applied materials & interfaces* 8(32) (2016) 20710-20719.
- [246] J. Bae, Y. Li, J. Zhang, X. Zhou, F. Zhao, Y. Shi, J.B. Goodenough, G. Yu, A 3D nanostructured hydrogel-framework-derived high-performance composite polymer lithium-ion electrolyte, *Angewandte Chemie International Edition* 57(8) (2018) 2096-2100.
- [247] W. Wang, E. Yi, A.J. Fici, R.M. Laine, J. Kieffer, Lithium ion conducting poly (ethylene oxide)-based solid electrolytes containing active or passive ceramic nanoparticles, *The Journal of Physical Chemistry C* 121(5) (2017) 2563-2573.
- [248] W. Liu, N. Liu, J. Sun, P.-C. Hsu, Y. Li, H.-W. Lee, Y. Cui, Ionic conductivity enhancement of polymer electrolytes with ceramic nanowire fillers, *Nano letters* 15(4) (2015) 2740-2745.
- [249] J.-H. Choi, C.-H. Lee, J.-H. Yu, C.-H. Doh, S.-M. Lee, Enhancement of ionic conductivity of composite membranes for all-solid-state lithium rechargeable batteries incorporating tetragonal $\text{Li}_7\text{La}_3\text{Zr}_2\text{O}_{12}$ into a polyethylene oxide matrix, *Journal of Power Sources* 274 (2015) 458-463.
- [250] M. Keller, G.B. Appetecchi, G.-T. Kim, V. Sharova, M. Schneider, J. Schuhmacher, A. Roters, S. Passerini, Electrochemical performance of a solvent-free hybrid ceramic-polymer electrolyte based on $\text{Li}_7\text{La}_3\text{Zr}_2\text{O}_{12}$ in P (EO) 15LiTFSI, *Journal of Power Sources* 353 (2017) 287-297.

- [251] J. Zhou, T. Qian, N. Xu, M. Wang, X. Ni, X. Liu, X. Shen, C. Yan, Selenium-Doped Cathodes for Lithium–Organosulfur Batteries with Greatly Improved Volumetric Capacity and Coulombic Efficiency, *Advanced Materials* 29(33) (2017) 1701294.
- [252] D.R. Paul, L.M. Robeson, Polymer nanotechnology: nanocomposites, *Polymer* 49(15) (2008) 3187-3204.
- [253] M. Winter, R.J. Brodd, What are batteries, fuel cells, and supercapacitors?, *Chemical reviews* 104(10) (2004) 4245-4270.
- [254] P.G. Bruce, Energy storage beyond the horizon: Rechargeable lithium batteries, *Solid State Ionics* 179(21-26) (2008) 752-760.
- [255] J. Zhu, P. Zhu, C. Yan, X. Dong, X. Zhang, Recent progress in polymer materials for advanced lithium-sulfur batteries, *Progress in Polymer Science* 90 (2019) 118-163.
- [256] J. Yue, M. Yan, Y.X. Yin, Y.G. Guo, Progress of the interface design in all-solid-state Li–S batteries, *Advanced Functional Materials* 28(38) (2018) 1707533.
- [257] H. Wang, Y. Cui, Nanodiamonds for energy, *Carbon Energy* 1(1) (2019) 13-18.
- [258] Y. Shi, G. Liu, R. Jin, H. Xu, Q. Wang, S. Gao, Carbon materials from melamine sponges for supercapacitors and lithium battery electrode materials: a review, *Carbon Energy* 1(2) (2019) 253-275.
- [259] S. Li, W. Zhang, J. Zheng, M. Lv, H. Song, L. Du, Inhibition of polysulfide shuttles in Li–S batteries: modified separators and solid-state electrolytes, *Advanced Energy Materials* 11(2) (2021) 2000779.
- [260] C. Yan, Y. Zhou, H. Cheng, R. Orenstein, P. Zhu, O. Yildiz, P. Bradford, J. Jur, N. Wu, M. Dirican, Interconnected cathode-electrolyte double-layer enabling continuous Li-ion conduction throughout solid-state Li-S battery, *Energy Storage Materials* 44 (2022) 136-144.

- [261] S. Evers, L.F. Nazar, New approaches for high energy density lithium–sulfur battery cathodes, *Accounts of chemical research* 46(5) (2013) 1135-1143.
- [262] H. Kim, J.T. Lee, A. Magasinski, K. Zhao, Y. Liu, G. Yushin, In situ TEM observation of electrochemical lithiation of sulfur confined within inner cylindrical pores of carbon nanotubes, *Advanced Energy Materials* 5(24) (2015) 1501306.
- [263] R.K. Selvan, P. Zhu, C. Yan, J. Zhu, M. Dirican, A. Shanmugavani, Y.S. Lee, X. Zhang, Biomass-derived porous carbon modified glass fiber separator as polysulfide reservoir for Li-S batteries, *Journal of colloid and interface science* 513 (2018) 231-239.
- [264] A. Manthiram, Y. Fu, S.-H. Chung, C. Zu, Y.-S. Su, Rechargeable lithium–sulfur batteries, *Chemical reviews* 114(23) (2014) 11751-11787.
- [265] X. Ji, K.T. Lee, L.F. Nazar, A highly ordered nanostructured carbon–sulphur cathode for lithium–sulphur batteries, *Nature materials* 8(6) (2009) 500-506.
- [266] X. Judez, M. Martinez-Ibanez, A. Santiago, M. Armand, H. Zhang, C. Li, Quasi-solid-state electrolytes for lithium sulfur batteries: Advances and perspectives, *Journal of Power Sources* 438 (2019) 226985.
- [267] J.G. Speight, *Lange's handbook of chemistry*, McGraw-hill New York 2005.
- [268] W. Chen, T. Lei, C. Wu, M. Deng, C. Gong, K. Hu, Y. Ma, L. Dai, W. Lv, W. He, Designing safe electrolyte systems for a high-stability lithium–sulfur battery, *Advanced Energy Materials* 8(10) (2018) 1702348.
- [269] R. Xu, J. Lu, K. Amine, Progress in mechanistic understanding and characterization techniques of Li-S batteries, *Advanced Energy Materials* 5(16) (2015) 1500408.
- [270] S. Zhang, K. Ueno, K. Dokko, M. Watanabe, Recent advances in electrolytes for lithium–sulfur batteries, *Advanced Energy Materials* 5(16) (2015) 1500117.

- [271] Y. Guo, H. Li, T. Zhai, Reviving lithium-metal anodes for next-generation high-energy batteries, *Advanced Materials* 29(29) (2017) 1700007.
- [272] S.S. Zhang, Liquid electrolyte lithium/sulfur battery: Fundamental chemistry, problems, and solutions, *Journal of Power Sources* 231 (2013) 153-162.
- [273] S. Zanotto, A. Blancato, A. Buchheit, M. Muñoz-Castro, H.D. Wiemhöfer, F. Morichetti, A. Melloni, Metasurface Reconfiguration through Lithium-Ion Intercalation in a Transition Metal Oxide, *Advanced Optical Materials* 5(2) (2017) 1600732.
- [274] Y. Diao, K. Xie, S. Xiong, X. Hong, Shuttle phenomenon—The irreversible oxidation mechanism of sulfur active material in Li–S battery, *Journal of Power Sources* 235 (2013) 181-186.
- [275] T. Lei, Y. Xie, X. Wang, S. Miao, J. Xiong, C. Yan, TiO₂ feather duster as effective polysulfides restrictor for enhanced electrochemical kinetics in lithium–sulfur batteries, *Small* 13(37) (2017) 1701013.
- [276] R. Demir-Cakan, M. Morcrette, Gangulibabu; Gueguen, A.; Dedryvere, R.; Tarascon, JM, *Energy Environ. Sci* 6 (2013) 176-182.
- [277] R. Rauh, F. Shuker, J. Marston, S. Brummer, Formation of lithium polysulfides in aprotic media, *Journal of Inorganic and Nuclear Chemistry* 39(10) (1977) 1761-1766.
- [278] R. Giannuzzi, M. Balandeh, A. Mezzetti, L. Meda, P. Pattathil, G. Gigli, F. Di Fonzo, M. Manca, On the Li Intercalation Kinetics in Tree-like WO₃ Electrodes and Their Implementation in Fast Switchable Electrochromic Devices, *Advanced Optical Materials* 3(11) (2015) 1614-1622.

- [279] M. Jia, X. Xu, J. Peng, J. Zhang, C. Yao, L. Li, Solution-Processed Double-Layer Electron-Transport Layer for Conventional Blue Phosphorescent Organic Light-Emitting Diodes, *Advanced Optical Materials* 4(10) (2016) 1635-1641.
- [280] Y.C. Jeong, J.H. Kim, S. Nam, C.R. Park, S.J. Yang, Rational design of nanostructured functional interlayer/separator for advanced Li-S batteries, *Advanced Functional Materials* 28(38) (2018) 1707411.
- [281] W. Ren, W. Ma, S. Zhang, B. Tang, Recent advances in shuttle effect inhibition for lithium sulfur batteries, *Energy Storage Materials* 23 (2019) 707-732.
- [282] H.J. Peng, J.Q. Huang, X.B. Cheng, Q. Zhang, Review on high-loading and high-energy lithium-sulfur batteries, *Advanced Energy Materials* 7(24) (2017) 1700260.
- [283] Z. Cui, C. Zu, W. Zhou, A. Manthiram, J.B. Goodenough, Mesoporous titanium nitride-enabled highly stable lithium-sulfur batteries, *Advanced materials* 28(32) (2016) 6926-6931.
- [284] B.-C. Yu, J.-W. Jung, K. Park, J.B. Goodenough, A new approach for recycling waste rubber products in Li-S batteries, *Energy & Environmental Science* 10(1) (2017) 86-90.
- [285] Z. Wei, Y. Ren, J. Sokolowski, X. Zhu, G. Wu, Mechanistic understanding of the role separators playing in advanced lithium-sulfur batteries, *InfoMat* 2(3) (2020) 483-508.
- [286] G. Liu, M. Reinhout, B. Mainguy, G.L. Baker, Synthesis, structure, and ionic conductivity of self-assembled amphiphilic poly (methacrylate) comb polymers, *Macromolecules* 39(14) (2006) 4726-4734.
- [287] H. Lin, T. Kai, B.D. Freeman, S. Kalakkunnath, D.S. Kalika, The effect of cross-linking on gas permeability in cross-linked poly (ethylene glycol diacrylate), *Macromolecules* 38(20) (2005) 8381-8393.

- [288] X.-X. Zeng, Y.-X. Yin, N.-W. Li, W.-C. Du, Y.-G. Guo, L.-J. Wan, Reshaping lithium plating/stripping behavior via bifunctional polymer electrolyte for room-temperature solid Li metal batteries, *Journal of the American Chemical Society* 138(49) (2016) 15825-15828.
- [289] C. Decker, K. Moussa, Photopolymerization of multifunctional monomers in condensed phase, *Journal of Applied Polymer Science* 34(4) (1987) 1603-1618.
- [290] S. Kalakkunnath, D.S. Kalika, H. Lin, B.D. Freeman, Viscoelastic characteristics of UV polymerized poly (ethylene glycol) diacrylate networks with varying extents of crosslinking, *Journal of Polymer Science Part B: Polymer Physics* 44(15) (2006) 2058-2070.
- [291] B. Ding, J. Wang, Z. Fan, S. Chen, Q. Lin, X. Lu, H. Dou, A.K. Nanjundan, G. Yushin, X. Zhang, Solid-state lithium–sulfur batteries: Advances, challenges and perspectives, *Materials Today* 40 (2020) 114-131.